

CHARACTERIZATION OF ULTRAFINE PARTICULATE MATTER
FROM TRADITIONAL AND IMPROVED BIOMASS COOKSTOVES

by

BRIAN GARY JUST

B.M.E., University of Minnesota (Twin Cities), 1999

A THESIS SUBMITTED IN PARTIAL FULFILLMENT OF
THE REQUIREMENTS FOR THE DEGREE OF
MASTER OF APPLIED SCIENCE

in

THE FACULTY OF GRADUATE STUDIES
(Mechanical Engineering)

THE UNIVERSITY OF BRITISH COLUMBIA
(Vancouver)

August 2012

© Brian Gary Just 2012

Abstract

Billions of people worldwide use biomass fires or cookstoves on a daily basis, with significant resultant contributions to emissions of global carbonaceous aerosols. The use of biomass as a fuel has an impact on local ecosystems, contributes to CO₂ levels in the atmosphere, and black carbon (BC) and organic carbon (OC) affect the earth's radiative balance. Widespread initiatives, including carbon funding programs, propose to replace traditional "three-stone" open fires with "improved" cookstoves designed to reduce fuel usage. While numerous studies investigate cookstove efficiency and publish emissions factors for gaseous pollutants and overall particulate matter (PM), there is a lack of focus on the size and nature of ultrafine particulate (UFP) emissions. This paper compares ultrafine emissions during steady combustion from a traditional three-stone fire and two improved stoves: a Rocket stove ("Chulika") and a Gasifier stove ("Oorja").

An AVL emissions bench measured gaseous products. PM instrumentation included a TSI SMPS, TSI APS, TSI DustTrak DRX, Magee Scientific Aethalometer, and 47mm PTFE and quartz filters; a thermophoretic sampling device was employed to gather material for PM imaging using transmission electron microscopy (TEM).

The improved cookstoves demonstrated high combustion efficiency compared to the three-stone fire and are likely to reduce biomass consumption. Additionally, emitted PM mass was reduced by a significant amount. PM emissions from improved stoves had a higher proportion of BC compared with total PM, though there was relatively little variation in overall BC levels. The reduction in highly scattering OC that would accompany a large-scale shift towards usage of improved stoves could affect the earth's radiative balance, but this merits investigation with consideration to other particle characteristics. Primary particles emitted from the improved stoves were smaller than those from the three-stone fire and appeared slightly less likely to coagulate into chain agglomerates. The observed shift towards greater quantities of smaller nanometer-sized particles could pose health concerns and is a point for further consideration by health scientists and reinforces the need for adequate ventilation for all cookstoves, independent of type.

Preface

The author conceived of the work leading to this research under the guidance of Profs. Steven Rogak and Milind Kandlikar. All cookstove tests, the literature review, data analyses, and transmission electron microscopy were performed by the author. Discussion in Sections 3.3 and 3.4 and Chapter 4 includes input from Profs. Rogak and Kandlikar.

A summarized version of this research was published as Paper #12-005 for the Combustion Institute – Canadian Section Spring Technical Meeting, held in Toronto, ON in May 2012.

Table of contents

Abstract	ii
Preface	iii
Table of contents	iv
List of tables	vi
List of figures	vii
List of symbols and abbreviations	ix
Acknowledgements	xi
1 Introduction	1
1.1 Biomass combustion	1
1.1.1 Wood composition	1
1.1.2 The combustion process	1
1.1.3 Gaseous emissions	2
1.1.4 Particle emissions	2
1.2 Effects of pollutants from cookstoves	4
1.2.1 Environmental	4
1.2.2 Health	5
1.3 Cookstove interventions	7
1.3.1 Stove types	7
1.3.2 Rocket stoves	8
1.3.3 Gasifier stoves	9
1.3.4 Key organizations and programs	10
1.3.5 Commentary	11
1.4 Review of existing research and methods	11
1.4.1 Previous research	11
1.4.2 Cookstove testing protocols	16
1.4.3 Exhaust collection methods	17
2 Experimental design	19
2.1 Instrumentation	19
2.1.1 Gaseous phase emissions	20
2.1.2 PM emissions	20
2.1.3 Auxiliary measurement devices	21
2.1.4 Data acquisition	22
2.2 Experimental setup	22
2.2.1 Stoves	22
2.2.2 Fuels	23
2.2.3 Protocol	24
2.3 Summary of test outputs	25
3 Analysis, results, and discussion	26
3.1 Testing overview	26
3.2 Analysis	26
3.2.1 Definition of “steady” burn	27
3.2.2 DustTrak correction	28
3.2.3 Carbon balance and emissions factors	28
3.3 Results	30
3.3.1 Cookstove performance at a glance	30
3.3.2 PM correction	34
3.3.3 EC/OC content	34
3.3.4 Carbon balance	37
3.3.5 PM size distributions	38

3.3.6	PM imaging	40
3.4	Additional discussion.....	43
3.4.1	Commentary on particle size	43
3.4.2	Commentary on EC/OC content	43
3.4.3	Relevance of size and composition for scattering-based instruments	44
3.5	Recommended future work.....	44
4	Conclusions	46
	References	47
	Appendices	51
	Appendix A: Exhaust system calibration and estimated dilution ratio	51
	Appendix B: Flow requirements and isokinetic probe sizing	55
	Appendix C: Gaseous phase emissions instrumentation details	56
	Appendix D: Estimate of PM diffusion losses.....	57
	Appendix E: PM emissions instrumentation details	59
	Appendix F: TPS design and notes.....	60
	Appendix G: Supplementary cookstove information.....	83
	Appendix H: Biomass fuel discussion and supplementary details.....	84
	Appendix I: Summary of testing protocol procedures	89
	Appendix J: Sample data sheet from cookstove test.....	91
	Appendix K: Gravimetric (PTFE filter) raw data, critical flow orifice calibration, and DustTrak repeatability	95
	Appendix L: Pollutant comparisons	97
	Appendix M: Sunset Laboratory EC/OC analysis results.....	99
	Appendix N: Emissions factors and GWP.....	101
	Appendix O: Overview of SMPS and APS scans.....	102
	Appendix P: Overview of combined SMPS / APS scans	114
	Appendix Q: Investigation of Oorja operating modes	116
	Appendix R: Overview of TEM imaging	118
	Appendix S: Primary particle sizing	135

List of tables

Table 1. Summarized emissions data from (Roden et al. 2006)	13
Table 2. Selected EF and ratios relative to total emissions, one test only, from (MacCarty et al. 2008).....	14
Table 3. Comparison of studies and motives	15
Table 4. BC concentration averages summarized from Kar et al. study (2012)	16
Table 5. Test outputs	25
Table 6. Summary of data collection	26
Table 7. Summary of combustion products, by percentage of carbon going to formation of a particular product (gaseous products only)	32
Table 8. PM mass comparison.....	34
Table 9. BC/PM (from aethalometer data)	35
Table 10. EC/OC content summary.....	36
Table 11. Summary of combustion products, by percentage of carbon going to formation of a particular product....	37
Table 12. Emissions factors, g/kg-dry fuel	38
Table 13. Average particle size within agglomerates (error based on standard deviation).....	42
Table 14. Plume velocity vs. distance below duct inlet in hood.....	52
Table 15. Summary of exhaust flow calibration data	53
Table 16. Flow rate requirements	55
Table 17. AVL Emissions Bench specifications (UBC SCRE Users Manual, Rev. E, (2009))	56
Table 18. Flows and dimensions for diffusion losses	57
Table 19. Particle size dependence of several dimensionless parameters relating to thermophoretic velocity	63
Table 20. Comparison of precipitation mechanisms.....	68
Table 21. TPS parametric analysis results	71
Table 22. Fuel elemental analysis summary (numbers represent percentage dry mass).....	84
Table 23. Averages of raw DustTrak data for each stove / test (all data in mg/m ³).....	95
Table 24. GWP comparison (without efficiency consideration).....	101
Table 25. Summary of SMPS / APS "good" scans	110
Table 26. TEM grid matrix.....	118
Table 27. TEM imaging coordinates (in um).....	118
Table 28. TEM imaging steps.....	119

List of figures

Figure 1. Kinetically limited chemical reactions and physical processes involved in soot formation (Lighty, Veranth, and Sarofim 2000), used with permission from Taylor and Francis.....	3
Figure 2. Schematic of soot microstructure (Flagan and Seinfeld 1988), used with permission from CaltechBOOK..	4
Figure 3. Predicted fractional deposition of inhaled particles in the nasopharyngeal, tracheobronchial, and alveolar region of the human respiratory tract during nose-breathing (based on data from ICRP (1994)). (Drawing courtesy of J. Harkema.) Springer and Springer Netherlands (Nanotechnology – Toxicological Issues and Environmental Safety and Environmental Safety, 28:15-51, 2007, p25, “Biokinetics and Effects of Nanoparticles,” Oberdörster, Figure 4. © 2007 Springer); with kind permission from Springer Science and Business Media.....	6
Figure 4. Traditional cooking methods: (a) three-stone fire, (b) traditional cookstove (Reprinted with permission from Roden, C. A., Tami C. Bond, Stuart Conway, and Anibal Benjamin Osorto Pinel. 2006. “Emission Factors and Real-Time Optical Properties of Particles Emitted from Traditional Wood Burning Cookstoves.” Environmental Science & Technology 40 (21) (November 1): 6750–6757. © 2006 American Chemical Society.).....	7
Figure 5. Stove examples (J. Jetter 2011), used with permission from J. Jetter.	8
Figure 6. Diagram of Rocket stove (Still and Winiarski 2001), used with permission from HEDON Household Energy Network.....	8
Figure 7. Example gasification stove cross-section.....	9
Figure 8. Schematic of emission sampling setup (Reprinted with permission from Roden, C. A., Tami C. Bond, Stuart Conway, and Anibal Benjamin Osorto Pinel. 2006. “Emission Factors and Real-Time Optical Properties of Particles Emitted from Traditional Wood Burning Cookstoves.” Environmental Science & Technology 40 (21) (November 1): 6750–6757. © 2006 American Chemical Society.).....	12
Figure 9. Recommended hood setup from WBT 4.1.2 (2009).....	18
Figure 10. (a) Photograph of exhaust system and (b) schematic of emissions testing setup.	19
Figure 11. (a) Three-stone fire, (b) Chulika and (c) Oorja cookstoves.....	23
Figure 12. Fuels used, (a) hemlock sticks, (b) commercial pellets	24
Figure 13. Example SMPS scan summary.....	27
Figure 14. Gaseous emissions data, test series #1, 2, 4; (a) CO ₂ , (b) CO, (c) NO, (d) NO _x , (e) CH ₄ , (f) THC	31
Figure 15. Uncorrected DustTrak PM data, test series #1, 2, 4	32
Figure 16. Sample of raw emissions data for Test Series #1.	33
Figure 17. CO vs. CO ₂ . One data point per second (12805 total) during all tests during "steady" period.....	33
Figure 18. BC vs. uncorrected PM (with least-squares fit for each stove)	35
Figure 19. Graphical representation of carbon-containing combustion products	37
Figure 20. (a) Normalized SMPS number distribution; standard deviation of the average value for each size bin is represented by “error bands” of the corresponding color [Oorja: N=36 (scans), Chulika: N=67; Three-stone: N=68]. (b) Cumulative distribution normalized to highest emitter (three-stone). Data for diameters smaller than 350 nm is displayed. All diameters are based on electrical mobility.	38
Figure 21. Normalized SMPS+APS distributions by number on a (a) linear and (b) log y-scale. Standard deviation of the average value for each size bin is represented by “error bands” of the corresponding color [Oorja: N=36 (scans), Chulika: N=67; Three-stone: N=68]. Diameter is based on electrical mobility. 0.35 – 0.52 um (total) counts given by the APS are also normalized and displayed.....	39
Figure 22. Example TEM imaging at 15k magnification; (a) three-stone, (b) Chulika, (c) Oorja.....	40
Figure 23. Example TEM imaging at 150k magnification; (a) three-stone, (b) Chulika, (c) Oorja.....	40
Figure 24. Example TEM imaging and primary particle (of agglomerates) sizing at high magnification; (a) three-stone at 300kx, (b) Chulika at 300kx, (c) Oorja at 500kx; (d) shows a number of individual primary particles for the Oorja at 500kx.	41
Figure 25. UBC cookstove test exhaust system.....	51
Figure 26. Photo of cookstove exhaust system, (a) upper assembly and (b) hood	51

Figure 27. Sketch of exhaust flow rate calibration test setup	53
Figure 28. Penetration vs. particle diameter for cookstoves emissions test setup.....	58
Figure 29. (a) dimensionless and (b) characteristic example of thermophoretic velocity vs. particle size ($k_g/k_p=10$, $\nabla T =5 \times 10^5$ K/m and $T=350K$)	63
Figure 30. Plate-to-plate thermophoretic sampler (Wen and Wexler 2007), used with permission from Taylor and Francis.	64
Figure 31. Deposition across the TPS of Thayer et al. (2011), used with permission from Taylor and Francis.	66
Figure 32. Configuration of ESP by Miller et al. (2010), used with permission from Taylor and Francis.....	67
Figure 33. Sample collection efficiency for an ESP (Miller et al. 2010), used with permission from Taylor and Francis.	67
Figure 34. Previous version of UBC TPS (Images: (Lagally 2011))......	69
Figure 35. New TPS (a) overall body, (b) heated tube, (c) removable base and magnetic cap, (d) close-up view of magnetic cap and TEM grid location.....	70
Figure 36. Wood pellet photograph	84
Figure 37. Moisture content analysis raw data	88
Figure 38. Gravimetric raw data for PTFE filters.....	95
Figure 39. Gravimetric vs. DustTrak PM mass comparison.....	96
Figure 40. Gaseous pollutants vs. PM; (a), (c), and (e) show species as labelled; (b), (d), and (f) correspond to the previous plots with the x-axis adjusted to show greater detail.....	97
Figure 41. Sunset Laboratory summary.....	100
Figure 42. Normalized combined SMPS / APS distributions	114
Figure 43. (a) Example of "bad" SMPS data, 3-stone test #6; (b) example of "good" SMPS data, 3-stone supplementary test #1b	115
Figure 44. Averaged SMPS results (not normalized) from follow-up testing	115
Figure 45. Oorja results from June 2012 follow-up tests.....	116
Figure 46. Raw sizing data, Oorja	137
Figure 47. Raw sizing data, Chulika.....	138
Figure 48. Raw sizing data, 3-Stone	138
Figure 49. Scaled sizing data, all stoves	139

List of symbols and abbreviations

APS (Aerodynamic Particle Sizer)
ARC (Aprovecho Research Center)
BC (Black Carbon)
CAWP (Centre for Advanced Wood Processing)
CCT (Controlled Cooking Test)
CDM (Clean Development Mechanism)
CER (Certified Emission Reduction)
CERC (Clean Energy Research Centre)
CHN (Carbon-Hydrogen-Nitrogen)
CPC (Condensation Particle Counter)
CREATE (Collaborative Research and Training Experience)
DB (Dynamic Blank)
DMA (Differential Mobility Analyzer)
EC (Elemental Carbon)
EF (Emissions Factor)
ELPI (Electrical Low-Pressure Impactor)
ESP (Electrostatic Precipitator)
ETHOS (Engineers in Technical and Humanitarian Opportunities of Service)
FID (Flame Ionization Detector)
FTIR (Fourier-Transform Infrared)
GWP (Global Warming Potential)
GWP₁₀₀ (100-year Global Warming Potential)
IPCC (Intergovernmental Panel on Climate Change)
JSMBT (Janara Samuha Mutual Benefit Trust)
KPT (Kitchen Performance Test)
MCE (Modified Combustion Efficiency)
NIOSH (National Institute for Occupational Safety and Health)
NMHC (Non-Methane Hydrocarbons)
NSERC (Natural Sciences and Engineering Research Council)
NTREE (National Round Table on the Environment and the Economy)
OC (Organic Carbon)
OM (Organic Matter / Material)
PCIA (Partnership for Clean Indoor Air)
PIC (Product of Incomplete Combustion)
PM (Particulate Matter)

PM0.1 (Particulate Matter with diameters smaller than 0.1 um, sometimes referred to as UFP)
PM2.5 (Particulate Matter with diameters smaller than 2.5 um, sometimes referred to as “fine” PM)
PM10 (Particulate Matter with diameters smaller than 10 um)
PSAP (Particle Soot Absorption Photometer)
PTFE (Polytetrafluoroethylene, commonly known as Teflon®)
RF (Radiative Forcing)
RH (Relative Humidity)
SCRE (Single Cylinder Research Engine)
SEM (Scanning Electron Microscope/Microscopy)
SMPS (Scanning Mobility Particle Sizer)
SSA (Single Scatter Albedo)
TC (Total Carbon)
TEM (Transmission Electron Microscope / Microscopy)
TEOM (Tapered Element Oscillating Microbalance)
THC (Total Hydrocarbons)
TLUD (Top-Lit Up Draft)
TNMHC (Total Non-Methane Hydrocarbons)
TPS (Thermophoretic Particle Sampler)
TSP (Total Suspended Particulate)
UBC (University of British Columbia)
UFP (Ultrafine Particulates, generally considered those with diameters smaller than 0.1 um, PM0.1)
USEPA (United States Environmental Protection Agency)
WBT (Water Boiling Test)
WHO (World Health Organization)

Acknowledgements

I acknowledge my supervisory team of Professor Steven Rogak from the Department of Mechanical Engineering and Professor Milind Kandlikar from the Institute for Resources, Environment and Sustainability and the Liu Institute for Global Issues. This interdisciplinary research would not have occurred without their encouragement and support.

I thank the Natural Sciences and Engineering Research Council (NSERC) Collaborative Research and Training Experience (CREATE) Atmospheric Aerosol Program for the fellowship that supported me during my graduate studies. I'd also like to express my appreciation for guidance from Prof. Andrew Grieshop and Dr. Conor Reynolds and for assistance from fellow researchers Bronson Patychuk, Hugo Arri, and Arka Soewono. Special thanks to others at The University of British Columbia (UBC) go to Vincent Leung at the Centre for Advanced Wood Processing, Derrick Horne and Brad Ross at the Bioimaging Lab, Bob Perry at the Clean Energy Research Centre, Winnie Chu at the Occupational and Environmental Health Laboratory, Markus Fengler and Roland Genshorek at the Mechanical Engineering machine shop, and Glenn Jolly and Sean Buxton at the Mechanical Engineering instrumentation shop.

1 Introduction

Billions of people worldwide use biomass fires or cookstoves on a daily basis, with significant resultant contributions to emissions of global carbonaceous aerosols. The potential to reduce health and environmental impacts by using “improved” cookstoves is well documented (Grieshop, Marshall, and Kandlikar 2011; K. R. Smith and Haigler 2008), as improved cookstoves can reduce fuel consumption and particulate matter (PM) emissions by reducing waste heat and/or enabling more complete combustion. Numerous initiatives target the replacement of traditional “three-stone” open fires with cookstoves designed to reduce fuel usage and emissions; e.g., the Global Alliance for Clean Cookstoves targets the distribution of 100 million cookstoves by the year 2020 (United Nations Foundation 2012).

Many cookstove studies investigate cookstove efficiency and report emissions factors for gaseous pollutants and PM, the latter reported as either total mass or PM_{2.5}, total mass of PM with diameters smaller than 2.5 μm (e.g., (J. Zhang et al. 2000; MacCarty et al. 2008; J. J. Jetter and Kariher 2009)). However, few studies focus on the size and nature of ultrafine particulate emissions which may penetrate the body more efficiently and be more harmful to humans (Auger et al. 2006). Roden et al. (2006) measured the black carbon (BC) and organic carbon (OC) content of cookstove PM; this detail helps to fill a gap in knowledge of the emissions characteristics of cookstoves, but there is still a need to determine whether PM from improved cookstoves may be smaller, more numerous, and/or morphologically or chemically different in a way that could adversely affect the expected environmental and health benefits of emissions reductions.

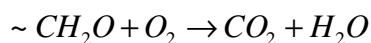
1.1 Biomass combustion

1.1.1 Wood composition

The dry composition of wood is dominated by cellulose (40-50% by dry mass), followed by hemicelluloses, lignin, and extractives. Cellulose is a linear, high molecular weight polymer that serves as the main structural element. Hemicellulose is amorphous and has a lower degree of polymerization than cellulose. Lignin acts as the cement that holds the cellulose together. Extractives, typically comprising less than 5% of dry mass, include alcohols, waxes, phenolics, and proteins. For reference, the elemental composition of an average of eleven hardwoods has been reported as 50.2% carbon, 6.2% hydrogen, 43.5% oxygen, and 0.1% nitrogen (Tillman, Rossi, and Kitto 1981). The chemical formula CH_2O can be used as an approximate proxy for the elemental content of wood.

1.1.2 The combustion process

Cellulose decomposes (pyrolyzes) with heat addition. This occurs first at the surface and in cracks, and volatile gases are emitted. These gases oxidize at temperatures above $\sim 200^\circ\text{C}$ according to the exothermic reaction



Heat from this reaction causes further cellulose decomposition once a fire has “started.” Meanwhile, in a separate and parallel reaction, charred wood (C) is oxidized by O₂, with CO₂ the lone product (of complete combustion).

Smouldering, which occurs when a fire is nearly extinguished, is a flameless low-temperature surface reaction involving endothermic pyrolysis and exothermic oxidation. Further notes on combustion phases and their characteristics appear in subsequent discussion.

Complete combustion results in two products: CO₂ and H₂O. Various other gases and solids represent various products of incomplete combustion (PICs), the emissions of which are of relevance to both climate and health concerns.

1.1.3 Gaseous emissions

Carbon dioxide (CO₂) is the most well-known greenhouse gas and, along with water, a product of complete combustion. Carbon monoxide (CO) is the primary PIC in wood combustion. Other carbonaceous by-products include CH₄ (also a powerful greenhouse gas), and non-methane hydrocarbons (NMHC).^{*} All of the above are needed in order to complete a carbon balance calculation, a useful tool for calculating emissions factors. Traces of other gases (e.g. NO_x) may also be present; see later discussion.

1.1.4 Particle emissions

Several commonly used terms relating to PM can cause confusion. *Atmospheric aerosol* represents a suspension of fine solids and liquids in a gas (air). *Smoke* “occurs” when small particles are present in sufficient quantities to be visible. *Soot* refers to agglomerations of light-absorbing carbon particles. *Ultrafine PM* (or *UFP*) is a subset of PM, typically referring to particles smaller than 0.1 μm; these are also sometimes referred to as nanoparticles.

PM composed of primary particles and agglomerates represents the solid PICs and is considered to comprise continuous units larger than molecular dimensions (size range 0.001 μm – 50 μm). It is categorized and measured in various ways. Total suspended particulate (TSP) and subcategories PM₁₀, PM_{2.5}, and PM_{0.1} (total PM smaller than 10 μm, 2.5 μm, and 0.1 μm, respectively) are common measures that report PM in terms of mass per volume of air. However, it is important to remember that PM does not consist of uniform, chemically-defined particles, but rather solids, liquids, and combinations thereof suspended in the air. It may be primary (emitted at the emission source) or secondary (the product of chemical or physical reactions that can involve other primary or secondary emissions), with size varying from nanoparticles to comparatively large particles with diameters measured in hundreds of microns. Chemically, PM contains a spectrum of substances, from innocuous materials like simple

^{*} Some instruments report total hydrocarbons (THC), which combines CH₄ and NMHC/TNMHC (total NMHC).

water to carcinogenic compounds such as polycyclic aromatic hydrocarbons (PAHs).^{*} In addition to size and composition differences, PM also varies by particle morphology, which is important because shape can affect its physical and chemical interactions with humans and the environment.

As an example of the complexity of PM, Figure 1 shows the processes involved in soot formation and effectively summarizes several processes and associated particle sizes and morphologies; timescale is dependent on the application.

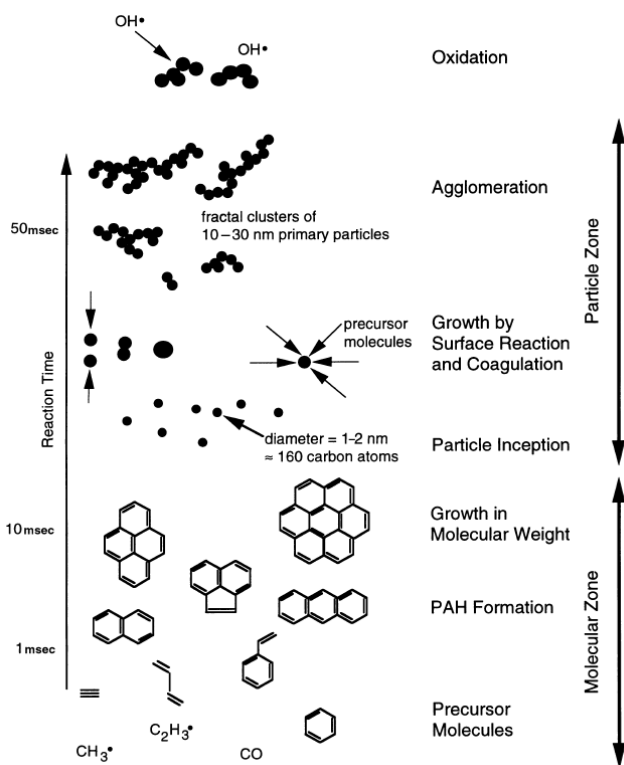


Figure 1. Kinetically limited chemical reactions and physical processes involved in soot formation (Lighty, Veranth, and Sarofim 2000), used with permission from Taylor and Francis.

The spherical “primary particles” indicated in Figure 1 are composed of “large numbers of lamellar crystallites that typically contain 5 to 10 sheets containing on the order of 100 carbon atoms each” (Flagan and Seinfeld 1988); see Figure 2 for an illustration. The spheres coagulate to form chain agglomerates and can also grow by the adsorption of vapour species on their surfaces.

^{*} In some contexts chemical composition can actually be used to determine the source of PM; e.g., (Goudie and Middleton 2001).

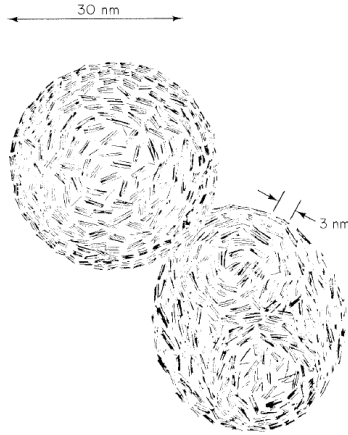


Figure 2. Schematic of soot microstructure (Flagan and Seinfeld 1988), used with permission from CaltechBOOK.

As carbon, hydrogen, and oxygen dominate the dry chemical composition of wood, other elements are present in only small amounts. As such, PM emissions are predominantly carbon-containing species that can be subdivided into OC and BC.*

1.2 Effects of pollutants from cookstoves

1.2.1 Environmental

730 million tons of biomass are burned in developing countries each year, with over a billion tons of resulting CO₂ emitted (World Bank 2011). The aim to minimize global climate change effects by controlling greenhouse gases has spurred programs that target reductions in biomass fuel usage. In addition to global effects, local ecosystems and social systems are affected by fuel collection which can cause depletion of resources, deforestation, and other land-use changes.

In addition to these local-to-regional effects, the OC and BC content of aerosols (PM) has the ability to affect the earth's radiative balance. From a simplistic point of view, OC scatters light, with a net cooling effect on both ground and atmosphere. Meanwhile, BC absorbs radiation, with the net effect of atmospheric warming and ground cooling (less radiation reaches the earth's surface). Factors such as land use change and settled BC that changes surface albedo (e.g., decreasing the reflective properties of ice and snow) complicate the quantification of aerosol effects. The total direct aerosol radiative forcing (RF) effect is estimated at $-0.5 (\pm 0.4) \text{ W/m}^2$, with biomass burning contributing $+0.03 (\pm 0.12) \text{ W/m}^2$; for reference, RF from fossil fuel OC is estimated to be $-0.05 (\pm 0.05) \text{ W/m}^2$, fossil fuel BC $+0.2 (\pm 0.15) \text{ W/m}^2$ (Forster et al. 2007).

* Elemental carbon (EC) is the operational equivalent to BC. The two terms are used interchangeably in this text.

Emissions from biomass-fuelled cookstoves represent ~20% of pyrogenic BC and OC; compare to fossil fuel burning, which contributes to 38% of pyrogenic BC and 7% of OC (Bond et al. 2004). Venkatamaran et al. (2005) calculate that biofuel combustion is the largest source of BC emissions in India and suggest its control as means to combat regional climate change. Menon et al. (2002) conclude that, in addition to radiative effects, BC significantly affects regional climate by altering the hydrologic cycle.

Other research has combined the varied effects of cookstove emissions with IPCC factors for 100-year CO₂ equivalent global warming potential (GWP) in order to compare the global warming impact of stove design alternatives (MacCarty et al. 2008).

In summary, biomass collection practices and the various constituents of cookstove emissions have the potential to affect the environment on many levels. Reductions in biomass usage and/or cookstove improvements that reduce emissions are likely to have positive environmental effects.

1.2.2 Health

Products of biomass fuel combustion include a wide range of gases ranging from the asphyxiant CO to carcinogenic hydrocarbons (e.g., benzene) and mutagenic organics. PM size and chemical content can vary immensely. Woodsmoke contains at least 26 hazardous air pollutants (Naeher et al. 2007).

According to the World Health Organization, nearly two million human deaths per year are attributed to the effects of cookstoves; indoor smoke is estimated to cause 21% of lower respiratory infection deaths, 35% of chronic obstructive pulmonary deaths, and 3% of lung cancer deaths worldwide (2009). Low birth weight and stillbirth have also been linked to indoor air pollution from stoves (Pope et al. 2010). According to Environment Canada, “Numerous studies have linked [particulate matter] to aggravated cardiac and respiratory diseases such as asthma, bronchitis and emphysema and to various forms of heart disease” (2012).

Not to be understated is the potential harm caused by UFP, or nanoparticles. It is important to understand the significance of PM size in proper context. In the human body, particle diameter (d) matters since it indicates if/where particles are likely to deposit. And though PM is typically reported in mass (d³), surface area (d²) is a better indicator of reactivity. Regarding the effects of nanoparticles on human beings, the literature is limited but provides evidence of size-dependent health effects.

Brown et al. (2001) investigated proinflammatory responses to polystyrene in rats and found a “significantly greater neutrophil influx into the rat lung after instillation of 64-nm polystyrene particles compared with 202- and 535-nm particles and this was mirrored in other parameters of lung inflammation, such as increased protein and lactate dehydrogenase in bronchoalveolar lavage.” Renwick et al. (2004) instilled fine and ultrafine carbon black (mean diameters 260.2 and 14.3 nm, respectively) and titanium dioxide (250.0 and 29.0 nm) into rats; the ultrafine particles

of both materials induced more inflammation and epithelial damage than the (larger) fine particles. Auger et al. (2006) exposed human nasal epithelial cells to both diesel exhaust and Paris urban air particles and reported that “internalization of particles, which is believed to initiate oxidative stress and proinflammatory cytokine expression, was restricted to small nanoparticles (≤ 40 nm).” In a report of the effects of nanoparticles, Oberdörster (2007) notes that the main deposition mechanism for inhaled particles <100 nm is due to diffusion from collisions with air molecules and states that alveolar macrophages (the prevalent mechanism for clearing larger particles from the alveolar region) do not efficiently clear particles <100 nm; deposited nanoparticles “appear to translocate readily to extrapulmonary sites and reach other target organs by different transfer routes and mechanisms.” It is not clear to what extent inhaled nanoparticles enter the blood stream of humans, though evidence supports the occurrence in rodents (e.g. 30 nm gold particles were found in pulmonary capillary platelets within 30 minutes of exposure to intratracheal regions (Berry et al. 1977)).

As indicated by Figure 3, deposition region is highly dependent on particle size; e.g. a high percentage of inhaled PM larger than 2.5 μm can be removed by moist surfaces and nasal hairs while many smaller particles will enter the lungs and may be deposited on the alveolar surfaces.

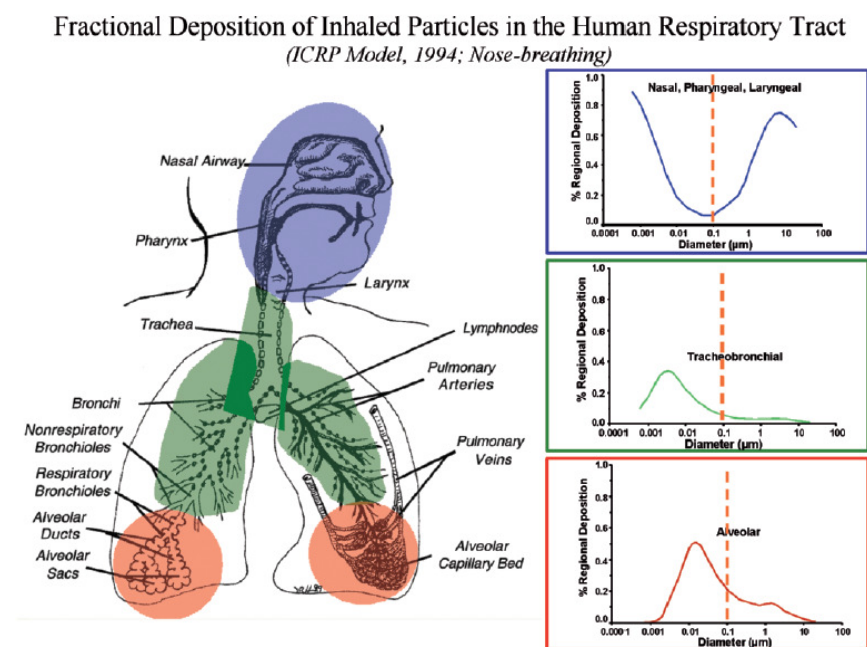


Figure 3. Predicted fractional deposition of inhaled particles in the nasopharyngeal, tracheobronchial, and alveolar region of the human respiratory tract during nose-breathing (based on data from ICRP (1994)). (Drawing courtesy of J. Harkema.) Springer and Springer Netherlands (*Nanotechnology – Toxicological Issues and Environmental Safety and Environmental Safety*, 28:15-51, 2007, p25, “Biokinetics and Effects of Nanoparticles,” Oberdörster, Figure 4. © 2007 Springer); with kind permission from Springer Science and Business Media.

Clearly, the health effects of cookstove emissions are not yet fully understood, especially with respect to nanoparticles. While this research cannot help to that end, it can help fill a gap in knowledge about the size and nature of nanoparticles emitted as a by-product of biomass combustion in cookstoves.

1.3 Cookstove interventions

A number of initiatives aim to replace traditional cooking methods with “improved” or “clean” cookstoves and are further detailed after an introduction to stove types.

1.3.1 Stove types

Billions of people worldwide use traditional methods for cooking. These may include the three-stone fire (Figure 4(a)), in which an open fire is lit directly underneath a cooking apparatus supported by stones, bricks, or other solid materials, and other simple traditional stoves (e.g., Figure 4(b)).



*Figure 4. Traditional cooking methods: (a) three-stone fire, (b) traditional cookstove (Reprinted with permission from Roden, C. A., Tami C. Bond, Stuart Conway, and Anibal Benjamin Osorto Pinel. 2006. “Emission Factors and Real-Time Optical Properties of Particles Emitted from Traditional Wood Burning Cookstoves.” *Environmental Science & Technology* 40 (21) (November 1): 6750–6757. © 2006 American Chemical Society.).*

Numerous improved or clean cookstoves aim to reduce the environmental and/or health effects of traditional cookstoves. There is no accepted distinction between “improved” and “clean;” they are often used interchangeably and without quantification of advantages offered versus traditional methods. Excellent overviews to stove types are given by MacCarty et al. (2008) and Jetter and Kariher (2009); Figure 5 shows a sampling of the large number of stove design alternatives available. In particular, two classes of improved cookstove designed for biomass combustion warrant further introduction.

- A. Ceramic Jiko, charcoal
- B. Metal Jiko, charcoal
- C. Belonio, rice hull
- D. Onil, wood
- E. Protos, plant oil
- F. Mayon Turbo, rice hull
- G. Oorja, pellet
- H. KCJ, charcoal
- I. GERES, charcoal
- J. StoveTec, charcoal
- K. Jinqilin CKQ-801, cobs
- L. 3-Stone Fire, wood
- M. Upesi, wood
- N. Uhai, charcoal
- O. Gyapa, charcoal
- P. Envirofit G-3300, wood
- Q. Sampada, wood
- R. Berkeley Darfur, wood
- S. StoveTec TLUD, pellet
- T. Philips HD4012, wood
- U. Philips HD4008, wood
- V. StoveTec, wood



Figure 5. Stove examples (J. Jetter 2011), used with permission from J. Jetter.

1.3.2 Rocket stoves

“Rocket” stoves (see Figure 6) are based on a few key features that include an insulated combustion chamber to keep the fire above 650° C, insulating, lightweight stove materials, an L- or J-shaped design with an elbow for fuel feeding, and a skirt that minimizes the distance between the stove and cooking pot (Still and Winiarski 2001).

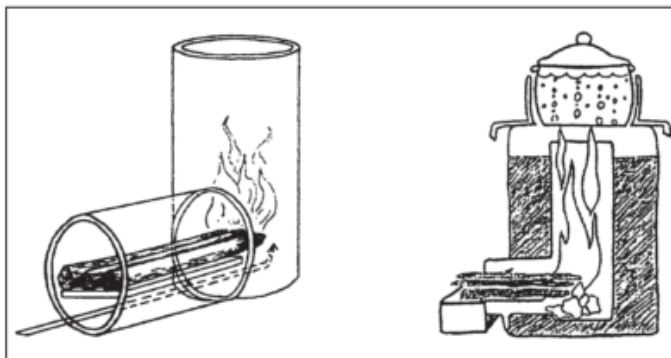


Figure 6. Diagram of Rocket stove (Still and Winiarski 2001), used with permission from HEDON Household Energy Network.

Hot, insulated combustion allows for more complete burning of fuel. An insulating, lightweight design with a skirt minimizes heat losses. The fuel-feed opening near the bottom allows sufficient quantities of air to enter the combustion chamber; the temperature gradient between this cool air and the hot combustion gases above the flame establishes a one-way air flow. A myriad of rocket stove designs and configurations exist beyond some of those depicted in Figure 5. Many target local economics and cater to available materials and fuels.

1.3.3 Gasifier stoves

Gasifier stoves create a combustible gas in a pyrolysis zone that is slightly separated from a combustion zone (see Figure 7). Within the stove base, biomass is pyrolyzed (charred, or decomposed without oxygen) in a high temperature region within a zone between unburned fuel and already-pyrolyzed char. Volatile gases, water vapour, and solid char are by-products of the reaction.

Primary and secondary air flows are employed. Primary air flow (at ambient temperature) is drawn through the fuel mixture and the pyrolysis zone; limited oxidation provides the heat required to sustain burning and pyrolysis. Some of the charred biomass (carbon) combusts in the primary air flow oxygen. Other char is subject to gasification; it reacts with water vapour and carbon dioxide to form hydrogen and carbon monoxide (partial oxidation). The resulting “syngas” and volatiles rise to the “top” of the stove, where they encounter a secondary air flow (which may be preheated via its pathway adjacent to a conductive combustion chamber wall) that mixes with the gases to allow for sustained burning.

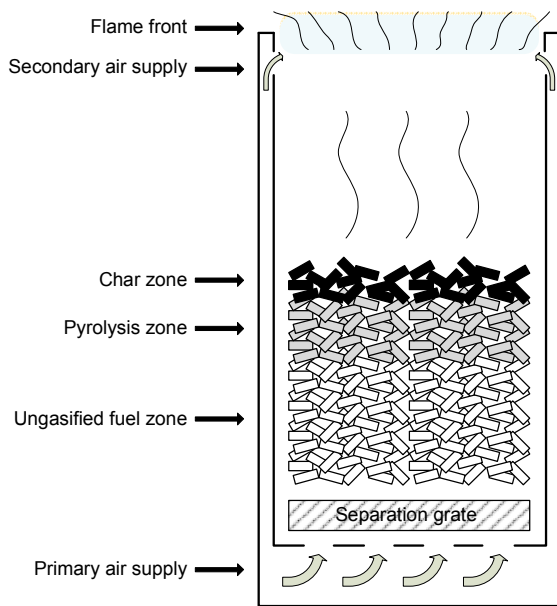


Figure 7. Example gasification stove cross-section

Gasifier stove designs can include forced air (typically via fan and battery) or natural draft for the air supply.

Operation near stoichiometric air to fuel ratio maximizes combustion temperature while maintaining combustion efficiency (rate of air flow offers a means to control combustion rate), but adjusting the air flow rate can present a challenge, especially with natural draft designs. Some gasifier stove configurations create char / charcoal that can be subsequently reused in other applications. Most require batch loading, since fresh material added to the top of the fuel supply interferes with effective stove operation.

1.3.4 Key organizations and programs

A number of organizations and initiatives target the wider distribution of improved cookstoves. Among the biggest is the Partnership for Clean Indoor Air (PCIA), a group of several hundred public and private organizations that aims to “improve health, livelihood, and quality of life by reducing exposure to indoor air pollution” (The Partnership For Clean Indoor Air 2012). The collective hosts forums and other events attended by leading players in the field; e.g., in February 2012 it hosted an International Standards Organization (ISO) workshop on cookstoves.* Engineers in Technical and Humanitarian Opportunities of Service (ETHOS) is a non-profit organization that focuses on “improving vernacular wood burning cooking stoves, including increasing efficiency and effectiveness while reducing emissions, addressing problems brought forward by the in-field partners”(Engineers in Technical and Humanitarian Opportunities of Service 2012); it holds annual conferences and its published proceedings are a rich source of information on stoves, testing and programs. The Aprovecho Research Center (ARC)[†] focuses on the design and testing of improved biomass cooking and heating. It conducts cookstove testing, training, and research and development. A number of researchers and higher learning institutions focus on cookstoves and effects; Kirk Smith’s Household Energy, Climate, and Health Project at the University of California – Berkeley[‡] and Tami Bond’s Aerosols in the Global Environment research group at the University of Illinois – Urbana-Champaign[§] are two examples.

Recent years have yielded new programs with enormous scope for implementing change. The Global Alliance for Clean Cookstoves targets large-scale adoption of clean cookstoves, the formulation of operational strategies, and research to facilitate progress towards its goal of bringing clean and efficient stoves and fuels to 100 million homes by 2020; the United States government alone has already committed over \$105m to the effort (US Department of State 2012). Another relatively recent and significant financial driver of change is the use of carbon credit funding for cookstove upgrades. The Clean Development Mechanism (CDM) “allows emission-reduction projects in developing countries to earn certified emission reduction (CER) credits, each equivalent to one tonne of CO₂. These CERs can be traded and sold, and used by industrialized countries to meet a part of their emission reduction targets under the Kyoto Protocol” (United Nations Framework Convention on Climate Change 2012). The Gold Standard is an example of a certification scheme that deals with carbon credits for CDM and voluntary markets.** A report published in May 2011 identified 43 cookstove projects that had applied for carbon credits, most on the voluntary exchange market; the majority aimed for biomass fuelled replacement cookstoves rather than stoves that required fuel switching (Cox 2011). A recent report acknowledged clean cookstoves’ ascent from “marginal volumes to prominent project type,” noting that in 2011, clean cookstove technologies transacted 3.2 MtCO₂e (primarily from Africa-based projects utilizing The Gold Standard) (Peters-Stanley and Hamilton 2012).

* In 2012, PCIA integrated with the Global Alliance for Clean Cookstoves.

[†] Website: <http://www.aprovecho.org/lab/home>.

[‡] Website: <http://ehs.sph.berkeley.edu/krsmith/>.

[§] Website: <http://www.hiwater.org/>.

** Website: <http://www.cdmgoldstandard.org/about-us/who-we-are>.

One example of a cookstove intervention with relevance to this research is a project administered by Janara Samuha Mutual Benefit Trust (JSMBT) in India. The organization used CDM funding to replace traditional cookstoves with an improved cookstove (named “Chulika”) in 21,500 households in Karnataka State. The stoves were distributed in 2011. Expected CO₂ emissions reduction is 43,215 tons per year (Janara Samuha Mutual Benefit Trust 2010). Monitoring of the program’s success is ongoing.

1.3.5 Commentary

The actual dissemination of improved cookstoves, whether by governments or non-government organizations is complicated by factors that include design, target customers, financing, and marketing; numerous programs have not been successful or sustainable (e.g., see (Shrimali et al. 2011)). Regardless, “clean” or “improved” cookstoves have become the subject of much attention and money, with significant programs and changes coming online at present and likely in the near future. This makes a better understanding of emissions – and soon – all the more important.

1.4 Review of existing research and methods

1.4.1 Previous research

Many studies evaluate cookstoves in laboratory and/or real-world environments. A selection of demonstrative examples is presented to explore the methodologies and motives that assisted the design and focus of the present experiment.

J. Zhang et al. (2000) compared 28 fuel / stove combinations in China. Most tests were conducted in a simulated village kitchen house. The study focused mainly on fuel types, although various stove types were tested and included brick and improved brick, with and without an exhaust flue. A modified water boiling test (WBT, discussed below) was utilized. Emissions samples were collected into a Tedlar bag via a probe inserted into the flue or inside a hood exhaust duct (for stoves with no flue). CO, CO₂, CH₄, and TNMHC emissions were measured from the Tedlar bag samples while TSP was measured gravimetrically and evaluated for carbon content with a thermal-optical technique. A carbon balance method was used to compute emissions factors which were reported on a fuel mass basis and on a delivered energy basis. Mean emissions factors for all tests involving wood combustion were 987, 58.7, 2.70, and 3.05 g/kg of dry fuel for CO₂, CO, CH₄, and TSP, respectively (J. Zhang et al. 2000). The authors note that for no biomass stove were PICs less than 4% of the original fuel carbon. The biomass stoves showed much lower efficiencies than liquid and gaseous-fuel stoves; solid fuels’ emissions varied widely at different times of the burn. Particulate size distributions were not measured.

Fan and Zhang (2001) measured emissions (PM, CO, CO₂, CH₄, THC) from five portable combustion devices (including lamps, candles, and a heater, but no cookstoves). A well-mixed chamber / room was used, enabling emission rates and factors to be calculated using a single-compartment mass balance model. Emissions were collected into Tedlar bags for offline analysis of CO₂, CH₄, and THC. CO was measured with a real-time

electrochemical instrument. Particle mass concentrations were measured with a nephelometer that monitored a size range of 0.1-10 μm with a detection limit of 0.02 mg/m^3 . Particle number concentrations and size distributions were determined with an optical particle counter sampling at 57 mL/min with eight size bins (in μm : 0.1-0.2, 0.2-0.3, 0.3-0.4, 0.5-0.7, 0.7-1.0, 1.0-2.0, >2). “Normal” and “high” burning conditions were tested. Most particles emitted were in the 0.1-0.3 μm range, with acknowledgement that smaller particles were not measurable by the devices used. In the presentation of results, the authors gave an overview of emission factors for other combustion devices. This is the earliest study encountered that attempted to characterize particle size, though the lower limit at 100 nm was too large to be useful and biomass combustion sources were not tested.

Roden et al. (2006) conducted a field study with wood-burning cookstoves in Honduras. An eight-armed probe was used to collect exhaust from the plume. CO and CO_2 were measured in real-time. PM was analyzed in real-time by two optical instruments, a particle soot absorption photometer (PSAP) which measured light absorption at three wavelengths and a nephelometer which measured light scattering at a single wavelength. PTFE and quartz filters were collected for offline determination of PM mass and EC/OC ratio. Figure 8 shows a schematic of the testing setup.

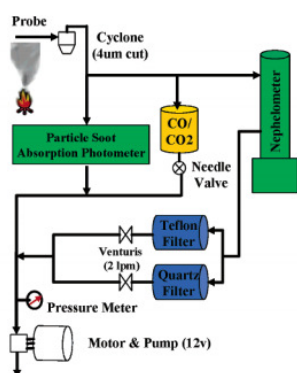


Figure 8. Schematic of emission sampling setup (Reprinted with permission from Roden, C. A., Tami C. Bond, Stuart Conway, and Anibal Benjamin Osorto Pinel. 2006. “Emission Factors and Real-Time Optical Properties of Particles Emitted from Traditional Wood Burning Cookstoves.” *Environmental Science & Technology* 40 (21) (November 1): 6750–6757. © 2006 American Chemical Society.).

Three combustion phases were noted (vigorous flaming, gentle flaming, and smouldering) and single scatter albedo (SSA) and absorption Angstrom exponent (\hat{A}_{ap}) were investigated at each. Mass emissions factors were reported in addition to the ratio of EC to TC (total carbon); this varied from 0.07-0.64 with an average of 0.30. EC/PM averaged 0.21 (in comparison, Venkataraman et al. (2005) measured BC:PM_{2.5} at 0.05-0.52 for small cooking fires. No correlation was distinguishable between wood moisture and EC/TC or PM emission factor. PM size distributions were not measured. Table 1 provides an overview of relevant data. The authors noted that for the wood used (oak and pine), average carbon content was 0.50 kg-carbon/kg-fuel. Since most carbon is accounted for

by CO₂ and CO, the sum of these species was considered a proxy for fuel combusted. PM size distributions were not measured.

Table 1. Summarized emissions data from (Rodén et al. 2006)

	Average	Improved stove
Mass emission factor (g-PM/kg-fuel)	8.5 ± 1.6	5.6 ± 0.7
OC emission factor (g-OC/kg-fuel)	4.0 ± 0.9	1.7 ± 0.3
EC emission factor (g-EC/kg-fuel)	1.5 ± 0.3	3.1 ± 0.5
EC/TC	0.30 ± 0.03	0.64 ± 0.04
CO emission factor (g-CO/kg-fuel)	116 ± 55	46 ± 19

Andreatta (2007) focused on a top-lot up draft (TLUD) gasifier stove developed by Paul Anderson and attempted to quantify efficiency and pollutants by boiling five litres of water with various combinations and forms of biomass fuels. Wood usage and pollutants were given in mass per litre of water boiled. Results were compared with a forced-air and a rocket stove design, though the author noted the difficulty in accommodating the “standard test” used by other designs (the TLUD stove is built for batch rather than continuous fuel feeding). Emissions were observed to be unsteady, even with an apparently steady flame. Disadvantages of the gasifier stove were fuel (and fuel packing) sensitivity, higher pollutants at shutdown, and user-dependent operation that could be inefficient and polluting. PM size distributions were not measured. Overall, a (gasifier) performance increase over a rocket stove was noted. Total CO emissions per liter of boiled / simmered water (per test protocol) were 3-4 times lower for the TLUD vs. the rocket stove. Similarly, PM emissions were about 4 times lower for the TLUD. The study provided a useful reference point for testing and emissions of a gasifier stove.

The purpose of MacCarty et al. (2008) was to quantify the relative emissions from five biomass-fuelled stoves. The testing protocol was a modified WBT and the stove setups and burning method are well-described. A Fourier-transform infrared (FTIR) system was used to measure 23 gaseous species. Particles were collected via a hood with a nephelometer measuring particle scattering and a PSAP for particle absorption in real time; a filter system collected samples for later mass and EC/OC measurement. For particulates, results were broken into EC and organic matter (OM). Though the fuel and the manner in which fires were attended affected the types of particles produced, the authors noted that stoves seemed to play a substantial role. In particular, the rocket design had a much higher proportion of particles with global warming potential (see Table 2). PM size distributions were not measured.

Table 2. Selected EF and ratios relative to total emissions, one test only, from (MacCarty et al. 2008)

	Cooling particles from smouldering fire		Warming particles from flaming fire	
	OM (g/kg-fuel)	OM/PM	EC (g/kg-fuel)	EC/PM
Three-stone	1.45	.62	0.88	0.38
Rocket	0.55	.32	1.16	0.68
Karve (gasifier)	0.82	.74	0.28	0.26

Roden et al. (2009) conducted field research in Honduras using traditional, “new” improved, and “broken-in” improved cookstoves. Research questions included: Are in-use emissions similar to those measured in a laboratory, can improved stoves improve environmental impacts, and do reductions continue as stoves age? They specified sampling locations with and without the use of chimneys and dilution ratios and resident times sufficient to establish phase equilibrium. Results were compared with a number of other field and laboratory studies. High PM emissions correlated to ignition and fuel addition events. Fuel variability and fire tending accounted for significant differences between actual in-use and laboratory results which differed by a factor of about three (laboratory results were always lower). EC fraction of PM was fairly consistent across all tests at about 0.25. PM size distributions were not measured.

J.J. Jetter and Kariher (2009) tested ten cookstoves with four fuels in order to measure and report cookstove performance and emissions data using a WBT protocol. Rocket, fan, and charcoal stoves representative of the many improved cookstove designs available were tested alongside a traditional three-stone fire. The testing system was well-described; WBT protocol (v1.5) was employed. Gaseous pollutant emissions were analyzed, PM_{2.5} emissions were measured using a filter method, and an electrical low-pressure impactor (ELPI) measured particle size distributions and concentrations in the 30 nm – 10 um range. Results were normalized to a starting temperature of 25°C. CO/CO₂ was used as an indicator of quality of combustion. Aside from a table comparing United States Environmental Protection Agency (USEPA) and ARC results, reported data was largely qualitative. PM size distributions and concentrations were not reported, though the ELPI is in theory capable of providing useful size data.

Q. Zhang et al. (2010) aimed to characterize UFP emissions using different cooking styles (Indian, Chinese and Italian) in a single-story family house (noting that UFP are more toxic than larger particles); the study used modern appliances and did not compare stove styles. A scanning mobility particle sizer (SMPS) was used to measure size distribution in the 7.6-289 nm range. A DustTrak photometer calibrated against a tapered element oscillating microbalance (TEOM) was used to gather particle mass concentrations. An aethalometer measured EC concentration. Air exchange rates were calculated via CO₂ concentration. Particle size distributions were plotted vs. time showing a primary mode at ~60-70 nm. A factor analysis compares particle number concentrations with changing power source (electric vs. gas), temperature (medium vs. high), and exhaust fan status (off vs. on). The stoves used did not burn biomass.

In the research presented above, study motives varied widely. Climate-focused studies focused on the EC/OC composition of PM. No literature was discovered that reported size distribution of cookstove emissions in the nanoparticle range.* Table 3 summarizes.

Table 3. Comparison of studies and motives

	(J. Zhang et al. 2000)	(Fan and Zhang 2001)	(Roden et al. 2006)	(Andreatta 2007)	(MacCarty et al. 2008)	(Roden et al. 2009)	(J. J. Jetter and Kariher 2009)	(Q. Zhang et al. 2010)
Control variable(s)	Fuel, stove type	Non-stove combustion devices	Fuel, stove	Fuel, stove type	Stove type	Setting, stove state	Stove type	Power source, fan status, temperature
WBT used?	Yes	No	No	No	Yes	Yes, for comparison	Yes	No
Health / climate focus?	Both	Health	Both	Both	Climate	Climate	Both	Health
PM size measured?	No, TSP only	Yes	No	No	No	No	Yes (not reported)	Yes
UFP measured?	No	No	No	No	No	No	?	Yes

A literature review conducted after the conclusion of the research presented in this thesis yielded further progress in cookstove emissions characterization.

Rehman et al. (2011) used indoor and outdoor field measurements in/around a village in rural India to correlate BC emissions to anthropogenic events. Indoor BC was measured in 35 households using a real-time microaethalometer, and a miniaturized aerosol filter sampler that collected 24 hour samples for later analysis. Outdoor BC was measured with an aethalometer at two locations in the village and at a nearby highway traffic junction. Twice-daily BC peak concentrations (up to 60 ug/m³) occurred at times coinciding with morning and evening cooking periods; the authors linked this to cooking events, not traffic. OC was approximately five times BC.

Kar et al. (2012) tested five commercially available (in India) gasifier stoves, three natural draft and two forced draft. A standardized Controlled Cooking Test (CCT) was used to simulate actual cooking conditions using hardwood and mixed (biomass) fuels. Microaethalometers measured BC concentrations in real-time at the expected inhalation height of a stove operator (“breathing zone”) and at a point 2 m directly above the burner (“plume zone”). Summarized results appear in Table 4. PM and gaseous pollutants were not measured.

* The Zhang et al. (2000) laboratory study used an SMPS to obtain UFP data, but did not compare cookstoves.

Table 4. BC concentration averages summarized from Kar et al. study (2012)

	BC concentration in breathing zone, ug/m ³	BC concentration in plume zone, ug/m ³
Mud stove	128 ± 65	335 ± 29
Average of forced draft stoves	38 ± 28 ^a (-70%)	78 ± 40 (-77%)
Average of natural draft stoves	78 ± 30 ^a (-39%)	224 ± 66 (-33%)

^a Not statistically significant due to high variance of results in each stove class

Guofeng et al. (2012) tested a number of wood fuels were in a single residential brick cooking stove in rural China. Emissions factors for PM, EC, and OC were measured, with the addition of PM size distributions. Modified combustion efficiency (MCE), defined as $CO_2/(CO_2+CO)$, was also reported. Sampling periods covered all stages of the burn cycle. PM was measured gravimetrically and EC/OC was analyzed. For PM size distributions, a nine-stage cascade impactor was used. MCE varied from 93.5-96.2%. PM ranged from 0.71-4.7 g/kg-fuel and showed high fuel dependency. OC/PM and EC/PM ratios were 0.32 ± 0.27 and 0.39 ± 0.26 , respectively. Correlations between emissions factors were investigated. The cascade impactor did not allow sufficient resolution (smallest bin size < 0.4 μ m) to capture the mode diameter of emissions from tree biomass combustion.

While these recent studies provide more data on BC concentrations from cookstoves, PM size distributions and morphological information are still lacking. Thus the research presented here is well justified and has potential to help fill a noteworthy and important gap in cookstove emissions literature.

1.4.2 Cookstove testing protocols

Several protocols are used in cookstove testing. Up-to-date protocols and training presentations are available from ARC.* The most common standard protocol for cookstove testing is the Water Boiling Test (WBT). Draft version 4.1.2 was last updated on October 1, 2009. Prepared by several key contributors in the stove testing field, the WBT is a simulation of the cooking process “intended to help stove designers measure how efficiently a stove uses fuel to heat water in a cooking pot and the quantity of harmful emissions produced while cooking” (Anon. 2009). It is meant to be a replicable way to assess stove performance. Three phases of cookstove operation are tested: cold-start high-power, hot-start high-power, and controlled simmering of a measured amount of water for 45 minutes (immediately following the second phase). Outputs are time to boil, burning rate, specific fuel consumption, firepower, turn-down ratio (ratio of high power to low power output) and thermal efficiency. The document gives specific instructions for each phase of the testing, along with advice for documentation and data collection; a companion spreadsheet assists with calculations for non-experts.

* See: <http://www.aprovecho.org/lab/pubs/testing>.

Weaknesses include the fact that controlled conditions are not necessarily representative of actual cooking circumstances and usage. Furthermore, efficiency is linked to heat transfer, meaning that stove / cooking vessel geometry and the use of auxiliary devices such as pot skirts can greatly affect results. It still provides valuable information, but can mask fundamental differences in the combustion characteristics of stoves. Also, emissions measurement is not an inherent feature of the WBT; rather, the protocol is perhaps best suited to field studies that focus on efficiency measurement. Many studies refer to a “modified” WBT in which the standard WBT is customized to suit a specific stove, fuel, and setting.

The Controlled Cooking Test (CCT) is meant to compare “improved” stoves to traditional designs in a manner that more closely replicates actual usage in cooking. Homogenous fuel supply, cooking pots, and water / food are used to minimize errors. The cooking is done by a local person, not by a researcher, and a single standardized test is repeated for each stove. Like the CCT, the Kitchen Performance Test (KPT) is meant to compare improved stoves to traditional ones; this is accomplished by measuring fuel consumption and by surveying local inhabitants.

Though the specific testing protocol is not critical, it is prudent to choose a recent, defined protocol to serve as a template. The WBT provides useful, well thought-out, developed guidelines for testing. However, since the focus of the present study is emissions measurement rather than efficiency, considerable modifications will be made.

1.4.3 Exhaust collection methods

Many studies collect emissions in Tedlar bags for later analysis. Existing gaseous emissions testing instruments available at UBC make this unnecessary. Two techniques for real-time exhaust collection and emissions testing are discussed below.

In the “chamber” method of exhaust collection, emissions factors are determined indirectly based on a mass rate balance within a specified volume. The method is detailed by Jawurek & Ballard-Tremeer (1999) in a study that compared emissions from two cooking devices. The chamber uses dilution, and stratification is avoided by the use of fans that mix the air. This method presupposes constant emission rate and fuel burn rate and the stove is operated in a way to keep both as constant as possible. For this reason, the authors determined that it is the better choice for continuously fuelled (as opposed to batch fuelled) stoves and it is an appropriate method for open fires. Once the emission source is removed, the air exchange rate in the closed volume must be measured (by decay of emissions species). Differing air exchange rates can make comparisons between tests problematic.

In the “hood” method, emissions are measured directly at/near their source. Gases are captured by a canopy, usually just above the combustion location. Ballard-Tremeer & Jawurek (1999) detailed this method in a study of three stoves tested with three hood extraction rates. SO₂ and TSP were shown to be independent of extraction rate and the effect on measured CO was small. The extraction rate range was quite narrow – 0.049 -0.065 m³/s, resulting in

velocities of 0.10-0.12 m/s (Ballard-Tremere and Jawurek 1999) – and the authors note that higher rates clearly affect combustion while lower rates will not capture all emissions. So while a drawback to the method is that the presence of an extraction hood is potentially capable of changing combustion characteristics, the influence of extraction is independent of stove type if the extraction level does not change between tests and air velocity lies within an acceptable range.

Based on a requirement to test different stoves (including batch and continuously fuelled designs), the hood method was selected and implemented in an engine test cell at the Clean Energy Research Centre (CERC) at UBC.

Recommendations from WBT version 4.1.2 (see Figure 9) were used as a guideline for design and construction of the cookstove testing exhaust system; details appear in the following chapter.

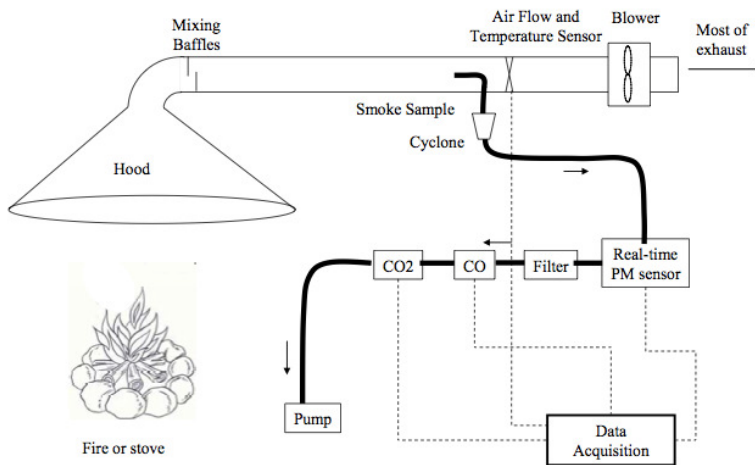


Figure 9. Recommended hood setup from WBT 4.1.2 (2009)

2 Experimental design

2.1 Instrumentation

The exhaust system pictured in Figure 10(a) was designed and constructed by the author at UBC. It extracts air from the combustion region and diverts it to the CERC building exhaust.

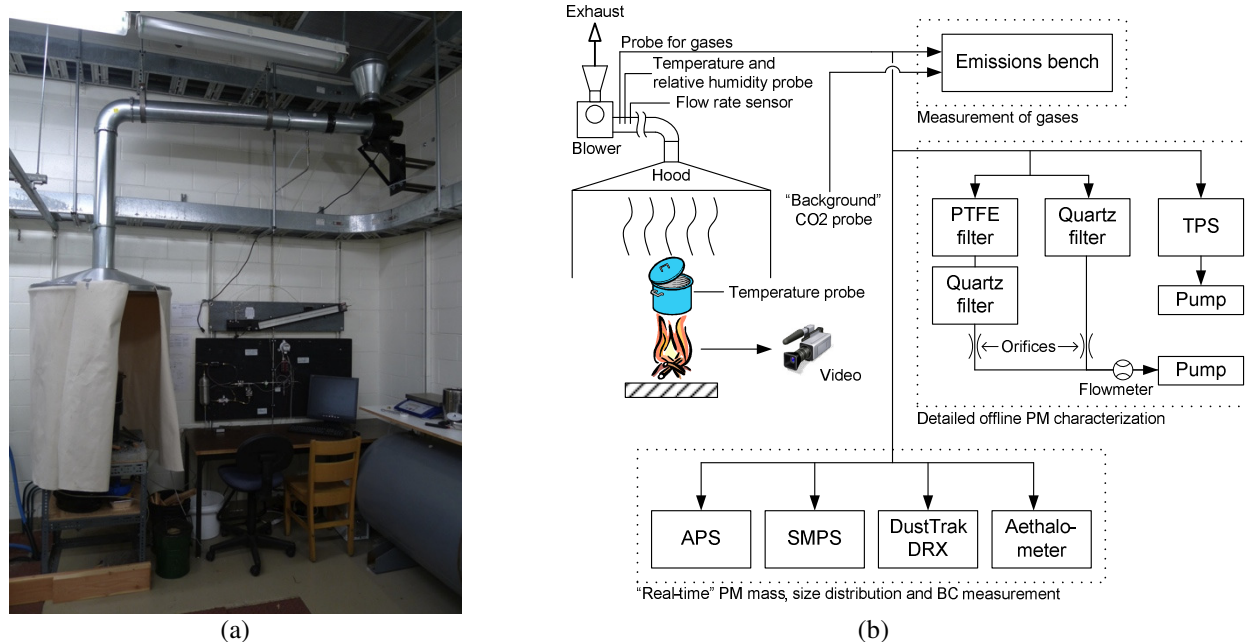


Figure 10. (a) Photograph of exhaust system and (b) schematic of emissions testing setup.

Natural dilution occurs as combustion products mix with ambient air before entering the exhaust hood; a dilution ratio of 100-150: 1 was targeted.* A single-speed blower provided an exhaust flow rate of ~190 scfm, and mixing baffles at the exhaust duct inlet ensured adequate mixing of combustion products with dilution (room) air in accordance with WBT guidelines. A smoke tube was used to verify that exhaust flow rate and hood geometry (including vertical length and access opening size) allowed for capture of all combustion products; hood height was adjusted so that plume velocity at the average stove height was near the recommended range.† A quasi-isokinetic

* In a study of laboratory diesel emissions (from engines), Kittelson et al. (2006) recommended a primary dilution ratio of 5-30:1 with 1-2 seconds residence time and secondary dilution with dry or humidity-controlled air used to raise overall dilution to > 200 in order to freeze coagulation. Lipsky and Robinson report that though EC measurements do not vary with dilution, dilution ratios < 100 are likely to “substantially overestimate” the emitted fine particle mass, and even at 350:1 mass emission rate may still be decreasing with increasing dilution ratio (2006). Appendix A details a dilution ratio definition and estimate for this research.

† WBT recommendations include (a) hood > 1m above the top of the stove, (b) sampling > 8 diameters downstream of mixing baffles and > 2 diameters upstream of the blow, (c) isokinetic sampling probe facing into the flow, and (d) all tubing made of stainless steel or conductive tubing, with lengths minimized (Anon. 2009). Exhaust flow rate measurement instrumentation was calibrated by introducing and measuring a metered quantity of 4.5% CO₂ into the

sampling probe, sized and constructed based on the expected flow requirement, is located approximately 15 diameters downstream of the exhaust inlet.* From the probe, exhaust is routed to instruments that measure gaseous phase and PM emissions. Figure 10(b) provides a schematic display of the exhaust system and instrumentation.

2.1.1 Gaseous phase emissions

Gaseous emissions are routed to an AVL CEB II Emissions Bench (calibrated each day of testing) that measures CO₂, CO, NO, NO_x, CH₄, THC, and O₂ at 1 Hz. The line is heated to prevent condensation. A second CO₂ line from a location outside of and adjacent to the exhaust hood goes to a second CO₂ sensor within the AVL emissions bench and serves as a continuous background CO₂ measurement. See Appendix C for further details on gaseous phase emissions instrumentation.

2.1.2 PM emissions

PM instruments are connected to the sampling probe via electrically conductive lines in order to minimize diffusion losses.† One branch of the circuit is connected to real-time instruments. A TSI DustTrak DRX Aerosol Monitor 8533 measures light scattering of an aerosol sample and provides an indirect measurement of PM mass in the 0.1 – 15 µm size range. It is calibrated with Arizona Road Dust and assumes a constant refractive index, so errors are present when composition and size are not constant. Relative humidity (RH) may affect this scattering signal,‡ though according to the manufacturer significant bias exists only at RH > 80%.

A TSI Scanning Mobility Particle Sizer (SMPS) Model 3080 with a custom differential mobility analyzer (DMA) column measures particles in the 14.6 – 661.2 nm diameter (midpoint) range. Within the SMPS, an impactor removes large particles before remaining particles are charged and sent the DMA, which size-classifies them according to electrical mobility. Monodisperse aerosol exits the DMA and the condensation particle counter (CPC) grows the particles to micrometer size and counts them optically. Scan time for the entire range of diameters is set to 135 seconds.

The TSI Aerodynamic Particle Sizer (APS) Model 3321 measures particles in the 500 nm – 20 µm aerodynamic diameter range by a time-of-flight technique that uses two laser beams. Scan time is set to 135 seconds to coincide with SMPS scans.

A Magee Scientific Aethalometer Model AE 21 measures BC via light transmission across quartz fibre filter material with 60-second sampling periods. The amount of absorption corresponds (is roughly proportional) to the amount of BC present. A spool of quartz fibre tape advances periodically when a particular filter spot reaches a

system. See Appendix A for further detail on the exhaust system, including a breakdown of components, flow rate calibration, and plume velocities.

* See Appendix B for further details on flow requirements and probe sizing.

† See Appendix D for an estimate of diffusion losses.

‡ This is a potential reason to not strictly follow the WBT, which advises boiling water in an open-topped vessel.

threshold loading density; data gaps exist when spool advances occur. A more direct but offline measure of BC is to collect aerosol onto PTFE and quartz filters for subsequent analysis in a laboratory (see below).

The preceding equipment is used to characterize PM size, composition and (roughly) BC. The instruments have on-board pumps that draw aerosol independently. See Appendix E for further details on PM emissions instrumentation.

In another branch of the test circuit, a pump draws air through a series of parallel devices in order to allow more detailed PM characterization. Aerosol is collected onto 47 mm diameter filters using stainless steel Gelman filter holders modified to accommodate backup filters. A PTFE membrane (Teflon®) filter is used for gravimetric PM mass measurement. Filters are weighed before and after sampling.

Quartz fibre filters are collected for EC/OC analysis. These employ a quartz backup filter behind the PTFE filter to correct for positive adsorption of organic gases; the OC content of the quartz backup filter is subtracted from the single quartz filter to correct for the artifact.* Procedure blanks are also collected. Critical orifices control flow rates for both 47 mm filters, and a Honeywell AWM 5104 Venturi mass flowmeter provides flow rate verification and accurate timing of PM collection periods.

A thermophoretic particle sampler (TPS) developed at UBC by the author is used to collect material onto 3.05 mm transmission electron microscopy (TEM) grids (Ted Pella model 0813-F, Carbon Type B support film[†] on 300 mesh copper) for microscopy work that provides PM morphology and supporting PM size data in the form of images. See Appendix F for further details on the TPS.

2.1.3 Auxiliary measurement devices

Exhaust flow rate is monitored continuously by a Nailor Ampliflow 36FMS-06 airflow sensor connected to a Dwyer MS-121-LCD differential pressure sensor; this was calibrated using a tracer gas as mentioned previously. Exhaust temperature and RH are measured before and after each testing period by a LabJack EI-1034 digital capacitive sensor. An auxiliary silicon temperature sensor (LabJack EI-1050) measures the temperature of water in the recipient vessel (in case of future interest). Video of stove flames is captured for later synchronization with data (in case of future interest).

* Some studies show that a better correction is obtained by having a quartz backup for both the quartz and PTFE filters; the OC content of the quartz filter behind the PTFE filter is used for the correction (it is subtracted from the “primary” quartz filter -- which itself has a quartz backup) (see (Turpin, Huntzicker, and Hering 1994)). However, the quartz-quartz configuration is avoided due to expense and to better align with the protocol of Chulika India tests.

[†] This consists of a Formvar® film coated with a heavier layer of carbon that is stable under a high array of operating conditions.

2.1.4 Data acquisition

Auxiliary devices are connected to a LabJack U3-HV data acquisition unit. A program designed with National Instruments LabVIEW software serves as the user interface with the inclusion of DustTrak data (which is also accessible via removable media). The SMPS and APS are connected to independent PCs; data is recorded via TSI's Aerosol Instrument Manager software. Aethalometer data is recorded onto a data card. AVL gaseous emissions data is recorded to the CERC Cummins ISX PC. Clocks for all real-time PM instruments and data logging PCs are synchronized before each day of testing.

2.2 Experimental setup

2.2.1 Stoves

As indicated by the selection shown earlier (see Figure 5), a large number of improved cookstoves exist, making it necessary to justify the selection of specific models. Focus in the present study is on low-cost, portable, single-burner stoves with wide distribution (or potential for it) in developing regions of the world. In this study, a traditional three-stone fire (see Figure 5.L) is tested against two improved designs (one Rocket, one Gasifier).

The traditional or “unimproved” baseline for the test is a three-stone fire comprised of three bricks (57 mm x 92 mm x 194 mm); the bricks are placed in symmetrical orientation with the cooking pot resting 92 mm from the base surface. This is similar in manner to the method employed by Yuntewi et al. (2008) in which three cement bricks measuring 19 cm x 6 cm x 6 cm were used.

Two “improved” cookstoves were selected. The Chulika was chosen for the Rocket stove based on its usage in a CO₂ reduction campaign funded by the Clean Development Mechanism (Janara Samuha Mutual Benefit Trust 2010). A development organization known as SAMUHA is administering the Chulika cookstove changeout in 21,500 households in Karnataka state, India. The selected Gasifier is the Oorja, formerly a British Petroleum-funded stove project and now in private hands and with active distribution in India. It is designed for pellets and batch loading, with forced draft powered by a fan and a single AA battery.

The Chulika and Oorja cookstoves were purchased in India in August 2012 for INR 1633 (C\$36) and INR 1050 (C\$21), respectively. Supplementary information on the cookstoves is available in Appendix G. The three tested cookstoves (hereafter, the three-stone fire is considered a cookstove) are pictured in Figure 11.

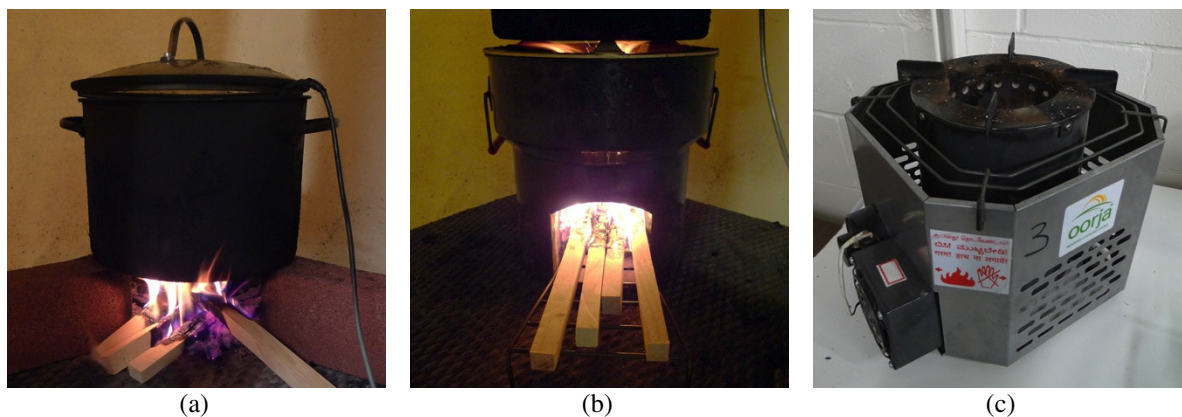


Figure 11. (a) Three-stone fire, (b) Chulika and (c) Oorja cookstoves

2.2.2 Fuels

Because the focus of the study is the change in PM size and composition across cookstove types, it is important to aim for consistency between tests rather than replicate an exact fuel used in a real-world situation. To minimize fuel variation as a source of error or differences in emissions, fuel for the three-stone and Chulika is from a single kiln-dried hemlock timber cut into sticks of rectangular 15-20 mm rectangular cross section (visible in Figure 11(a,b) and Figure 12(a)). All pieces were cut on the same day and stored in identical manner, and testing occurred over a minimal period of time. Moisture content was measured at 9.54% (dry basis)^{*} just prior to testing.[†] A carbon-hydrogen-nitrogen (CHN) elemental analysis done at the UBC Mass Spectrometry Centre yielded a carbon content of 47.53% of dry mass.[‡]

Since the Oorja cookstove is not designed to burn sticks,[§] commercial pellets produced in British Columbia are used. Pellets are ~6.5 mm diameter with an average length of ~10 mm; see Figure 12(b). Moisture content was 6.94% (dry basis) and carbon content was 47.70% of dry mass.^{**}

^{*} On a dry basis, moisture content is reported as moisture content divided by dry mass; in wet basis reporting, the divisor is the wet mass (before drying). Moisture meters (e.g., Delmhorst BD-2100) typically report on a wet basis. The two terms are not interchangeable but can be easily converted.

[†] Wood moisture content was measured by drying a fuel sample at 105°C until mass no longer decreased; Appendix 1 of the WBT protocol was used as a guideline; a short section is reproduced in Appendix H. The oven drying and mass measurement were done at UBC's Centre for Advanced Wood Processing (CAWP).

[‡] The source of material for the CHN analysis was 5 mg of mixed fine shavings from several sticks.

[§] Appendix H contains a brief discussion of the attempt to utilize the same fuel and shape across all stoves.

^{**} The source of material was 5 mg of pulverized powder from a random sampling of several pellets.



Figure 12. Fuels used, (a) hemlock sticks, (b) commercial pellets

Although testing with a second fuel and/or moisture content is perhaps justifiable based on the possibility of different combustion characteristics among the wide range of available fuel variants, it is not realistic to exactly duplicate fuel supplies from around the world. In any case, most end-users of cookstoves likely have little control over biomass fuel choice. The fuels used in this study have similar chemical makeup and should suffice for a comparative study between cookstoves. Appendix H contains additional information about the fuels, data used for moisture content calculation, and CHN analysis data sheets.

2.2.3 Protocol

Because distinct combustion phases with unique emissions properties exist between burn phases (Roden et al. 2006), a “steady-state” combustion condition was targeted instead of using the efficiency-based WBT.* Preliminary tests were conducted with each cookstove to learn about optimal ignition and fuel loading techniques. Early testing of the Chulika indicated an initial burn period characterized by high, unstable PM mass emissions. Starting with fresh fuel it takes about 20 minutes to reach a stable condition in which the fire is maintained by a relatively uniform mix of charred and fresh fuel. “Stable” is relative, as considerable spikes still occur, but with proper fuel tending anomalous events can be avoided.† The batch-loaded Oorja reaches a “steady” well-lit condition after approximately 10 minutes. Further discussion appears in Results.

Following the “warm-up” period, for the Chulika cookstove a continuous four-stick burn (Figure 11.b) was tended for 60 minutes. After each Chulika test, all char and fuel was transferred immediately to a three-stone fire. This reduced the start-up phase, after which the three-stone fire was tended in similar manner for 60 minutes. Oorja testing began with 700 g of pellets, sufficient for 30-35 minutes of “steady” data following the warm-up and before

* During WBT Phases 1 and 2, the aim is to bring to boil a predetermined quantity of water. In Phase 3, the flame is controlled to maintain water temperature at 3°C below the boiling point within a range of $\pm 3^\circ\text{C}$ for a prolonged period (45 minutes).

† Care is taken to avoid biasing the data collection, e.g., by removing data corresponding to smoke plumes (which are a natural and unavoidable part of biomass combustion).

fuel depletion. Oorja performance was influenced by the starting temperature of its insulated combustion chamber. For this reason, tests for all stoves occurred after a sufficient cool-down period (3-4 hours minimum).

Six tests were conducted for each of the three cookstoves. Background data was collected for ten minutes prior to test start-ups and subtracted from eventual results. Because three-stone testing was an extension of the Chulika tests, Chulika background data was used for the respective three-stone data set. A stainless steel pot containing 5 L of water was used as a heat sink / flame deflector to roughly simulate cooking conditions.* To avoid contamination from particles that may have settled on sampling system walls (e.g., during high-polluting stove start-ups and extinguishing events), dwell times of several minutes were allowed for between tests and PM measurements.

During testing, the AVL emissions bench, DustTrak, aethalometer, and auxiliary instruments recorded continuously. SMPS and APS scans were initiated at three minute (approximate) intervals. Filters and TEM grids were collected as required. Appendix I contains a checklist of procedures followed for each test.

2.3 Summary of test outputs

The outcome of this study is a quantitative comparison of (number) size distribution and EC/OC information for the three-stone fire and the two improved cookstoves. Supporting data includes measures of gases, combustion efficiency, overall PM mass, and PM images. Table 5 gives an overview of measurements taken for the eighteen tests. Shaded regions represent outputs that make this research unique.

Table 5. Test outputs

Measurement	Direct output	Data source	Result	Notes
Gaseous emissions	CO, CO ₂ , NO _x , THC, CH ₄ (in ppm)	AVL emissions bench	Carbon balance, emissions factors	Data taken for all tests, used in carbon balance
Particulate mass	PM (Dustrak: mg/m ³ , PTFE filters: mg)	DustTrak, gravimetric measurement of PTFE filter	Carbon balance, emissions factors	Data taken for all tests, used in carbon balance
EC/OC content	PM masses (mg)	Aethalometer, NIOSH 5040 analysis of quartz filter	Dimensionless EC:OC ratio, EFs	Filters not collected / analyzed for all tests
PM size distribution	Size (nm) and number distribution	SMPS, APS	Size (nm) and number distribution	Data taken for all tests
Video	.avi file	Webcam	.avi file	Post-test qualitative verification of test conditions (if necessary)
PM morphology	Images	TPS with TEM	Images	Grids not collected / analyzed for all tests

* This was changed 1-2 times per test to avoid boiling (and increased RH in the exhaust).

3 Analysis, results, and discussion

3.1 Testing overview

Eighteen tests (six for each of the three cookstoves) were conducted on 3-8 March 2012. Manual checklists / recording sheets were used to document certain information (see Appendix J for an example). Table 6 summarizes the data collection and indicates tests for which complete data does not exist.

Table 6. Summary of data collection

Run ID	Lab-VIEW	AVL	Aethalo-meter	APS	SMPS	Dust Trak	Video	PTFE filter	Backup quartz filter	Quartz filter
Oorja1	√	√	√	√	√	√	√	√	√	√
Chulika1	√	√	√	√	√	√	√	√	√	√
3Stone1	√	√	√	√	√	√	√	√	√	√
Oorja2	√	√	√	√	√	√	√	√	√	√
Chulika2	√	√	√	√	√	√	√	√	√	√
3Stone2	√	√	√	√	√	√	√	√	√	√
Oorja3	√	x	x	√	√	√	√	√	√	√
Chulika3	√	x	x	√	√	√	√	√	√	√
3Stone3	√	x	x	○	√	√	√	√	x	x
Oorja4	√	√	√	√	√	√	√	√	√	√
Chulika4	√	√	√	√	√	√	√	√	√	√
3Stone4	√	√	√	√	√	√	√	√	√	√
Oorja5	√	√	√	√	√	√	√	x	x	x
Chulika5	√	√	√	√	○	√	√	√	√	√
3Stone5	√	√	√	√	○	√	√	√	√	√
Oorja6	√	√	√	√	√	√	√	x	x	x
Chulika6	√	√	√	√	○	√	√	x	x	x
3Stone6	√	√	√	√	○	√	√	√	√	√

√ Successful / complete data

x No data

○ Bad / insufficient data

During test series #3, the AVL emissions bench and aethalometer did not properly record data. For the three-stone fire in this test series, APS data is invalid due to insufficient sheath flow (clogged air filter). The SMPS yielded erroneous data for most of test series #5 and 6 due to a malfunction with the power supply that prevented the DMA from reaching > 4000 V (~10,000 V is required in normal operation); see later discussion.

3.2 Analysis

Focus is on the three tests for each cookstove for which complete and valid data was recorded (test series #1, 2, and 4). Data from all instruments was aligned using timestamps recorded during data collection. Where practical,

comparisons are made to existing studies and data, keeping in mind that the main contribution of this study is quantitative information on ultrafine PM. Determining the “ideal” stove is beyond the scope of the project, as is the interpretation of cookstove policy choices and the health and climate implications of results. Further details on a selection of relevant analyses are included here.

3.2.1 Definition of “steady” burn

The rate of CO₂ emissions is not an effective measure of steadiness since it is a measure of carbon combustion rate and not “maturity” of the fire; for the same reason flame temperature (not measured) would not be a suitable objective measure. Real-time PM (as measured by the DustTrak) could be used to define the steady state, but its correlation and variation with fueling events makes it hard to accept as an objective measure.* Rather, the steady burn period is defined by noting SMPS size distributions. For a given stove / test, PM mean size is time dependent during the initial burn period. At a certain point, it stabilizes and further runs yield similar size distributions *despite* irregularities associated with fueling. As noted in the discussion of testing protocol, the Chulika cookstove reaches a “steady” burn state approximately 20 minutes after ignition; the Oorja reaches this state at about 10 minutes.

This “stabilization” is best indicated by an example. In Figure 13, red lines indicate the first five SMPS scans after cookstove ignition (for Chulika test #3). Black lines show all subsequent scans; they are scattered randomly (no clear time-based trend). In this example, the good / steady data period coincides with the beginning of the sixth SMPS scan. Note that although the term steady is used, this implies only that the time dependent variation is minimized. Considerable variations in emissions still occur, but by averaging a number of scans over a range of tests, repeatable results can be reported.

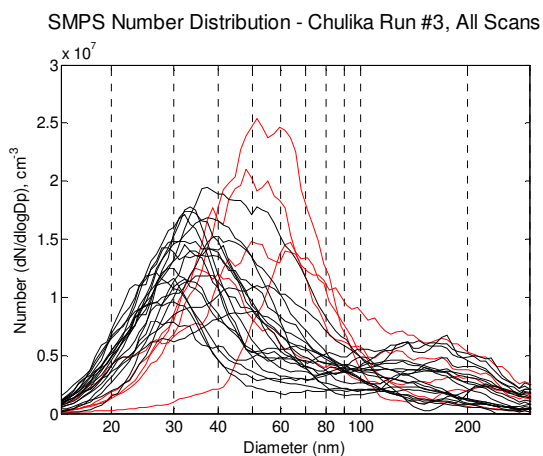


Figure 13. Example SMPS scan summary

* Data-correlated video provided alternate means of determining steadiness but was not used in the analysis that follows.

3.2.2 DustTrak correction

PTFE filter samples were collected for most tests as indicated by Table 6. Prior to weighing, filters were preconditioned for at least 24 hrs in the Balance Room in the Occupational and Environmental Health Laboratory at UBC.* Each filter was charge-neutralized using a Po-210 source and weighed three times before / after aerosol collection using a Sartorius Micro M5P balance. A set of control filters was also weighed three times before each session.

Filter masses are combined with collection time and known rate of flow (via calibrated critical orifice) in order to determine mass of PM per volume of exhaust air. The mass of PM that collects on a filter is determined by

$$m_{PM, \text{filt}} = \bar{m}_{\text{filt}, \text{posttest}} - \bar{m}_{\text{filt}, \text{pretest}} - \left(\bar{m}_{\text{control}, \text{posttest}} - \bar{m}_{\text{control}, \text{pretest}} \right)$$

A dynamic blank was collected and measured with the same protocol and is subtracted from the results with an adjustment for its collection time according to the equation

$$m_{PM, \text{filt}, DB_{\text{corrected}}} = m_{PM, \text{filt}} - \frac{t_{\text{filt}}}{t_{DB}} m_{PM, DB}$$

where t_{filt} is the filter collection time, t_{DB} is the collection time of the dynamic blank (filter), and $m_{PM, DB}$ is the measured mass of PM on the dynamic blank. DustTrak-predicted filter loading is calculated by integrating its 1 Hz readings during the period of filter collection (or using its average value). The following equation is used:

$$m_{PM, DT} = A \left\langle \frac{mg}{m^3} \right\rangle \cdot t_{\text{filt}} \langle s \rangle \cdot Q_{\text{orifice}} \left\langle \frac{l}{\text{min}} \right\rangle \cdot \left[\frac{\text{min}}{60s} \cdot \frac{m^3}{1000l} \right]$$

A is the average DustTrak reading during collection time and Q_{orifice} is the calibrated flow rate through the critical orifice. Masses $m_{PM, \text{filt}}$ and $m_{PM, DT}$ are compared across multiple tests and a correction factor is determined. See Appendix K for supporting data.

3.2.3 Carbon balance and emissions factors

Gaseous emissions are corrected by subtracting averaged background measurement data. Net CO₂ from combustion (exhaust minus ambient measurement) also includes a correction based on the (small) difference in readings between the two CO₂ sensors during the background testing period.

* Room temperature is maintained at $21 \pm 2^\circ \text{C}$. RH is $40 \pm 5\%$.

Emissions factors (EFs) were determined by a carbon balance in which combusted carbon from fuel is accounted for by CO₂ and the measured carbon-containing PICs: CO, CH₄, NMHC,* and PM, according to the equation

$$C_{burn} = C_{CO_2} + C_{CO} + C_{CH_4} + C_{NMHC} + C_{PM}$$

where C_x represents carbon from a specific compound. Carbon emission rate for individual gaseous species is determined by

$$\dot{C}_x \left\langle \frac{g_{C_x}}{s} \right\rangle = [X] \left\langle \frac{mol_x}{1e6 \cdot mol_{exh}} \right\rangle \cdot M_{C_x} \left\langle \frac{g_{C_x}}{mol_x} \right\rangle \cdot Q_{exh} \left\langle \frac{mol_{exh}}{s} \right\rangle$$

where background corrected concentrations of gaseous species [in brackets, X denotes reading] are in parts per million (ppm; equivalently, moles of x per million moles of air / exhaust). M_{C_x} is the mass of carbon in a mole of the substance. Q_{exh} is the total exhaust rate in moles of air per second.

For PM,

$$\dot{C}_{PM} \left\langle \frac{g_{C_{PM}}}{s} \right\rangle = PM \left\langle \frac{g_{PM}}{m_{exh}^3} \right\rangle \cdot \chi \frac{g_C}{g_{PM}} \cdot Q_{exh} \left\langle \frac{m_{exh}^3}{s} \right\rangle$$

PM is DustTrak PM (by mass) with a correction based on gravimetric measurements. χ is the mass ratio of carbon to PM and is adjusted for each cookstove based on gravimetric and EC/OC analysis (see below). Q_{exh} is the exhaust rate converted to volume of air per second based on measured atmospheric conditions in the laboratory.

To estimate instantaneous carbon burn rate, rates from products are summed,

$$\dot{C}_{burn} \left\langle \frac{g_{C_{burned}}}{s} \right\rangle = \sum \dot{C}_x \left\langle \frac{g_{C_x}}{s} \right\rangle$$

\dot{C}_{burn} is used to normalize PM data and is also a factor in determining EFs for combustion products as follows,

$$EF_x \left\langle \frac{g_x}{g_{C_{burned}}} \right\rangle = \frac{\dot{C}_x \left\langle \frac{g_{C_x}}{s} \right\rangle \cdot \frac{M_x}{M_{C_x}} \left\langle \frac{g_x}{g_{C_x}} \right\rangle}{\dot{C}_{burn} \left\langle \frac{g_{C_{burned}}}{s} \right\rangle}$$

* THC measured by the AVL emissions bench is inclusive of CH₄, so NMHC = THC – CH₄ (molar basis). The calibration gas is propane C₃H₈, so three carbon atoms per molecule of NMHC are assumed in subsequent carbon balance equations.

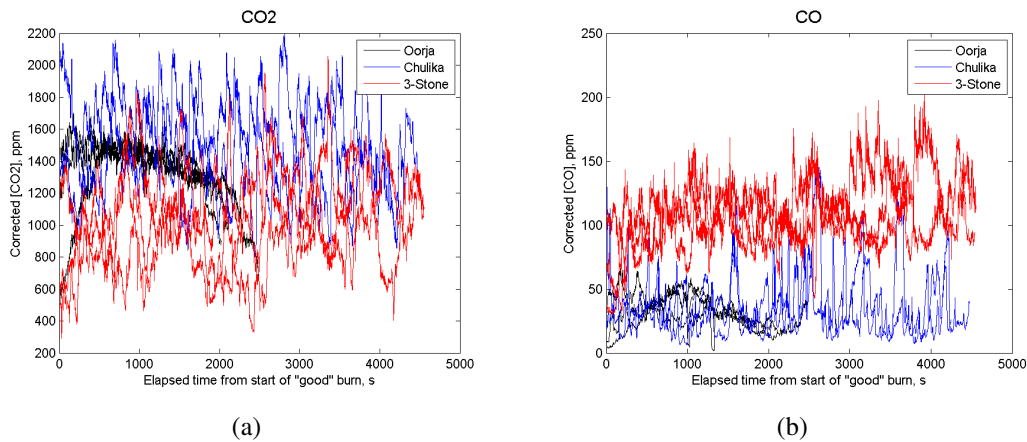
M_x/M_{C_x} is the ratio of molecular weight of a compound to the mass of carbon in that molecule. EFs are reported in terms of pollutant mass per mass of carbon burned.* Additionally, by focusing only on products, it is straightforward to calculate the percentage of total (carbon) for each combustion product:

$$\%_x = \frac{\dot{C}_x}{\dot{C}_{burn}}$$

3.3 Results

3.3.1 Cookstove performance at a glance

Before a detailed investigation of particle size distribution, chemical composition, emissions factors, and morphology, it is useful to explore some raw data from the experiments. Real-time gaseous emissions data (minus background measurements) for all three cookstoves is presented in Figure 14; each stove (color) has three overlaid traces corresponding to test series #1, 2, 4.



* Pollutant mass per unit of energy delivered is a common way to report EFs in the literature, but it includes variables that may confound results (see earlier discussion). Pollutant mass per mass of fuel is a viable alternative since carbon content of fuel is known, but this makes comparison with other studies and fuel types less straightforward.

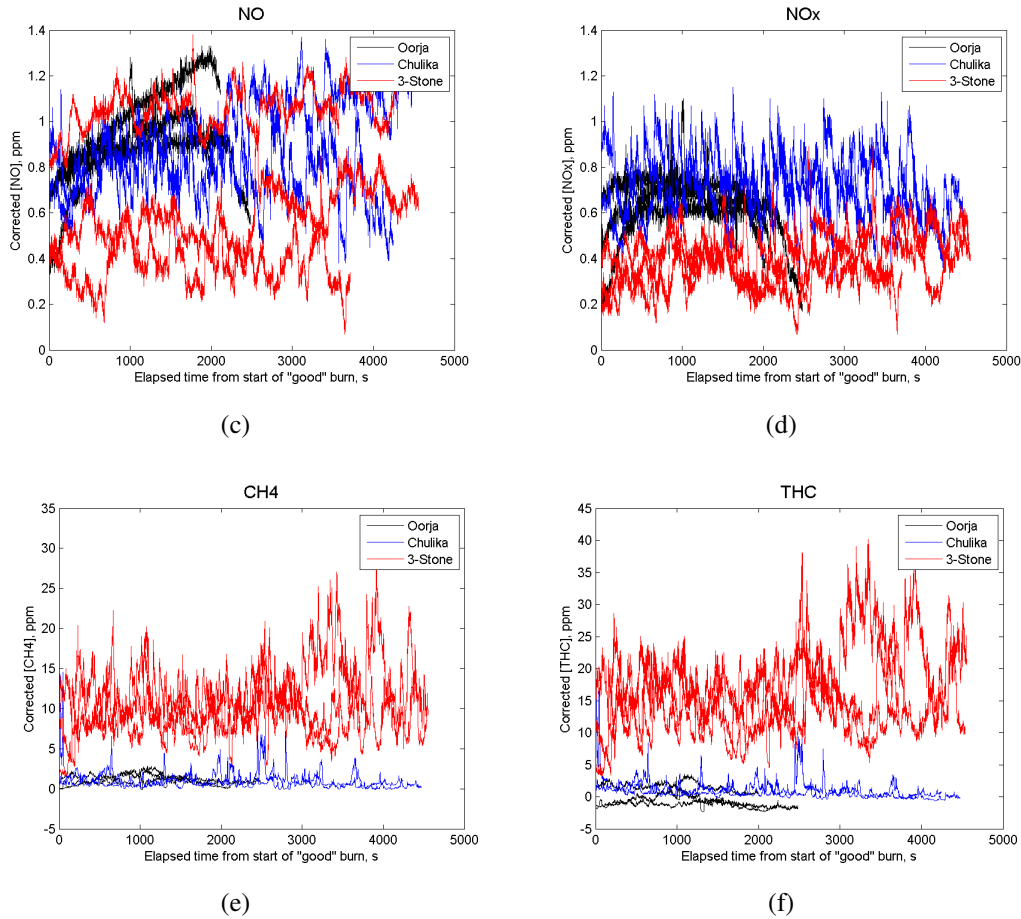


Figure 14. Gaseous emissions data, test series #1, 2, 4; (a) CO_2 , (b) CO , (c) NO , (d) NO_x , (e) CH_4 , (f) THC

A few items are noteworthy. First, emissions levels are most stable for the Oorja; this is particularly evident for CO_2 and CO data. On further investigation, pollutant spikes in Chulika and three-stone data are linked to fire tending events. Second, CO is significantly higher for the three-stone fire than for the improved cookstoves. Third, NO and NO_x levels are insignificant and on the same order as background measurements. This is also generally the case for CH_4 and THC with the exception of the three-stone fire, which emits appreciable levels of hydrocarbons.

Considered on its own, CO_2 is a measure of combustion / fueling rate and is not independently relevant to stove performance. A likely cause of the CO_2 spikes is simply the addition of fuel, or fuel movement that results in relatively large exposed surface areas of uncharred wood that leads to rapid devolatilization and combustion. CO spikes may occur if inadequate O_2 is present to fully combust the devolatilized material. Table 7 details the relative composition of gaseous carbon-containing species by percentage of total available measured carbon that goes to a particular species. More accurate results would include PM in these combustion product percentages and is discussed later.

Table 7. Summary of combustion products, by percentage of carbon going to formation of a particular product (gaseous products only)

Species	Three-stone	Chulika	Oorja
CO ₂	88.4	97.7	97.7
CO	9.3	2.3	2.3
CH ₄	0.9	0 ^a	0 ^a
NMHC	1.4	0 ^a	0 ^a

^a Not clearly distinguishable from background data.

Other comparative non time-series plots with various combinations of PM and gaseous products are shown in Appendix L. There is a tendency for all gaseous PICs to increase roughly linearly relative to PM (also a PIC) for incomplete combustion, with the three-stone fire consistently showing the highest levels of pollutants.

Uncorrected PM (from the DustTrak) is plotted in Figure 15. As noted in the discussion of gaseous pollutants, spikes are associated with fire tending events. Averaged uncorrected DustTrak PM levels across the steady burn periods of test series #1, 2, and 4 yield 28.5, 4.63, and 1.07 mg of PM per gram of carbon burned for the three-stone, Chulika, and Oorja cookstoves, respectively. More accurate results would report PM with a correction based on gravimetric measurements; this is presented and discussed later.

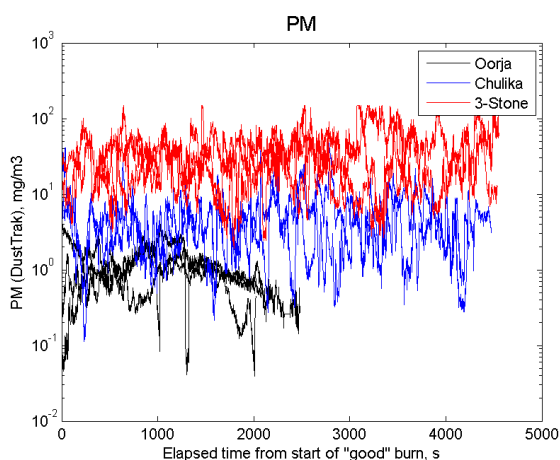


Figure 15. Uncorrected DustTrak PM data, test series #1, 2, 4

The most relevant data to this research are PM and the most significant components of the carbon balance, CO₂ and CO. In Figure 16, these three combustion products are plotted for convenience during a 1500-second steady-burn period for each cookstove.

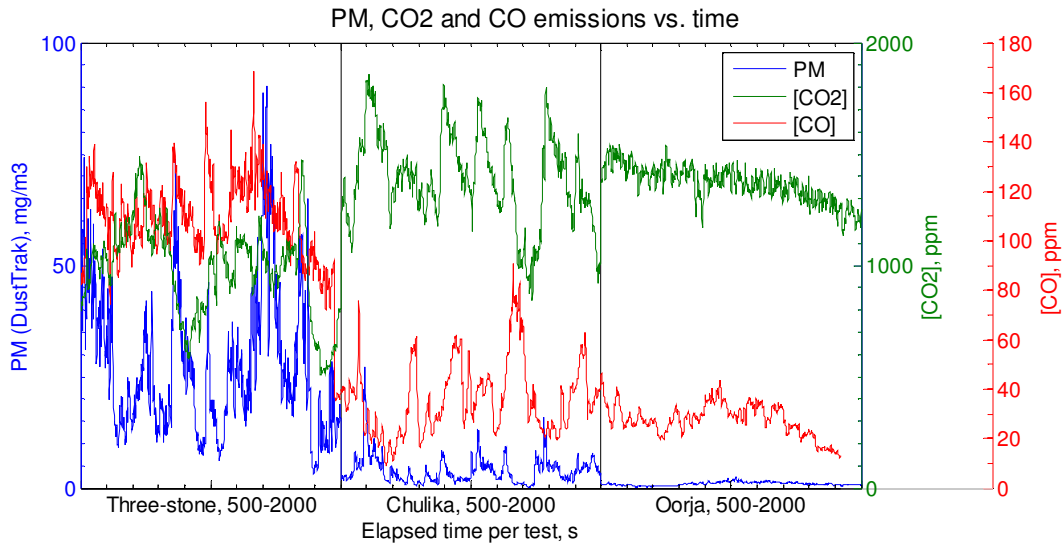


Figure 16. Sample of raw emissions data for Test Series #1.

There is a sizable reduction in PM from the three-stone fire to the Chulika, and again from the Chulika to the Oorja. CO emissions follow a similar trend; CO₂ is displayed as a comparative measure of rate of combustion.

The ratio of CO₂ to CO can be used as a measure of combustion efficiency. As expected based on time-series data (Figure 14 and Figure 16), Figure 17 indicates increasing efficiency corresponding to the transition from three-stone to Chulika to Oorja.* While a quantitative study of efficiency is not the aim of this research, the obvious increase in combustion efficiency with the improved cookstoves is relevant to subsequent results and discussion.

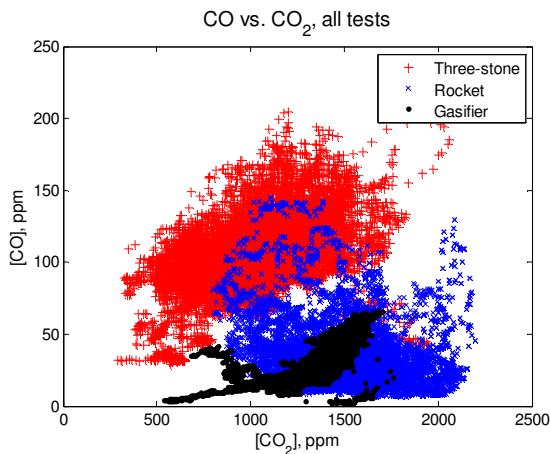


Figure 17. CO vs. CO₂. One data point per second (12805 total) during all tests during "steady" period.

* Complete combustion would yield zero CO regardless of CO₂ output (a horizontal line at y=0 in Figure 17).

3.3.2 PM correction

Post-test weighing of PTFE filters taken during test series #1, 2, and 4 provides a gravimetric measure of PM against averaged data from the DustTrak during the (filter) collection period. Table 8 summarizes; supporting data and a brief analysis of DustTrak repeatability between tests appears in Appendix K. The third column is the corrected average of *all* PM data taken for each stove type during the defined steady test period (i.e., not only during filter collection). Recalling Figure 14(a), which shows the variation of the CO₂ emissions rate (which represents most of the carbon) between the cookstoves tested, a further correction is applied to normalize for carbon burn rate; the fourth column of Table 8 displays normalized corrected PM data based on the average carbon burn rate during Chulika testing.*

Table 8. PM mass comparison

Stove	DustTrak PM (mg/m ³) ^a	DustTrak error ^b	Corrected PM (mg/m ³) ^c	Normalized corr. PM (mg/m ³) ^d
Three-stone	35.0	+172 ± 13%	10.5	8.25
Chulika	3.93	+21 ± 4%	3.81	3.81
Oorja	1.05	-16 ± 10%	1.27	1.18

^a DustTrak PM is based on an average of uncorrected DustTrak readings *during the filter collection period*. DustTrak data from here onwards subtracts the average result taken during the background test period.

^b (DustTrak – gravimetric measurement) / gravimetric measurement; positive value indicates DustTrak overestimation. Error is standard deviation based on the three filter tests for each stove type.[†] Gravimetric measurement includes correction based on dynamic blank measurement (with per-filter adjustment for collection time). The DustTrak error for each stove is used to correct PM in subsequent calculations.

^c Based on *all* DustTrak data during the steady period of all valid tests.

^d Normalized to the carbon burn rate for the Chulika cookstove (highest average burn rate during testing).

Although the difference in average PM levels between stove types is less pronounced with the gravimetric correction, the improved cookstoves still result in significantly lower PM emissions. Further commentary on the discrepancy between DustTrak readings and gravimetric results appears during discussion of EC/OC content.

3.3.3 EC/OC content

Aethalometer data provides a near real-time estimate of BC (considered here as roughly equivalent to EC) content. DustTrak data corresponding to each 60-second aethalometer reading is averaged and plotted against PM in Figure 18.[‡]

* The Chulika is selected simply because it has the highest burn rate in these tests. Differences in exhaust flow rate between tests (typically < 2%) are ignored.

[†] Five filters (per stove) were collected with accompanying DustTrak feedback. Averages and standard deviations are based on tests 1, 2, and 4 because later analysis uses EC/OC content data corresponding with quartz filter collection during those runs only. Differences between overall averages and standard deviations and those of the selected runs are highlighted in Appendix K.

[‡] Negative and near-zero values are filtered out.

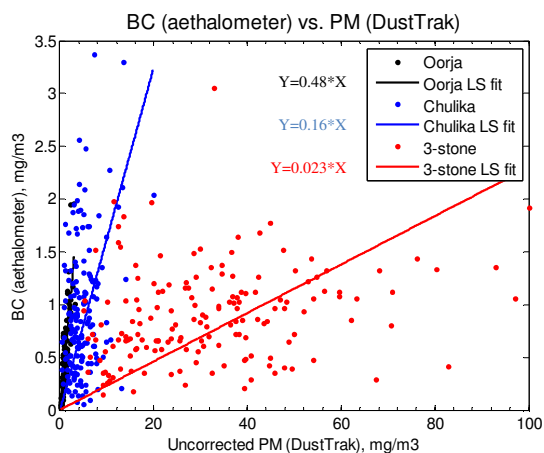


Figure 18. BC vs. uncorrected PM (with least-squares fit for each stove)

The slopes of least-squares-fit lines yield BC/PM ratios as follows: Oorja, 0.48; Chulika, 0.16; three-stone, 0.023. Applying the previously calculated gravimetric correction to the DustTrak PM data gives updated estimates of BC/PM ratios as summarized in Table 9.

Table 9. BC/PM (from aethalometer data)

Stove	BC/PM (uncorrected)	BC/PM (corrected)
Three-stone	0.023	0.063
Chulika	0.16	0.20
Oorja	0.48	0.41

A more accurate measurement of BC is obtained via quartz filters. Sunset Laboratory Inc. (Tigard, OR) performed an analysis of the quartz filters collected during cookstove tests according to the National Institute for Occupational Safety and Health (NIOSH) 5040 protocol. Three filters for each stove type were analyzed* and all were corrected for positive OC artefact by subtracting OC content of a quartz filter behind a PTFE filter taken in parallel. Total carbon (TC) is reported by NIOSH 5040 along with EC (the operational equivalent to BC) and OC. Table 10 summarizes results and includes comparisons with aethalometer and gravimetric measurements. Appendix M contains further details on the protocol along with raw data from the EC/OC analysis and details on repeatability.

* 1.50 cm x 1.00 cm sections of filters were used.

Table 10. EC/OC content summary

Stove	EC/TC (Sunset Lab)	TC/PM ^a (Sunset Lab)	EC/PM ^b (Sunset Lab)	BC/PM ^c (aethalometer)
Three-stone	0.15	0.56	0.083	0.063
Chulika	0.80	0.67	0.53	0.20
Oorja	0.70	0.86	0.60	0.41

^a TC from Sunset Lab analysis of quartz filters; PM from PTFE gravimetric analysis with dynamic blank correction. This mass ratio is used in the carbon balance equations. Denoted previously as χ , it allows for a more accurate carbon burn rate calculation (the effect is small) used to normalize PM size distributions in the next section.

^b EC from Sunset Lab analysis of quartz filters; PM from PTFE filter. The calculation assumes uniform distribution of matter onto quartz and PTFE filters and an effective collection diameter of 35 mm for the PTFE filter.

^c BC from aethalometer; PM from DustTrak with gravimetric correction (column reproduced from Table 9).

While a direct comparison should not be made due to differences in fuels and stoves, these results are in rough agreement with Roden et al. (2006), who reported EC/TC ratios of 0.07 – 0.64 (average 0.27) in a test of 11 traditional Honduran cookstoves; 0.64 ± 0.04 was the EC/TC ratio of a single improved cookstove. In tests conducted with several wood fuels in a residential brick cooking stove, Guofeng et al. determined an EC/PM ratio of 0.39 ± 0.26 (2012).

The Sunset Lab analysis concurs with aethalometer data that indicates that improved stoves produce much more EC as a percentage of TC (or PM) than the three-stone fire. By assuming uniform distribution of PM on the PTFE filter taken in parallel, it is possible to estimate EC/PM ratio. The shaded columns in Table 10 compare results obtained by the laboratory method and the aethalometer data. In both cases, the Oorja cookstove produces the “blackest” PM and the three-stone fire produces the highest organic content.

A few points regarding this data merit attention. First, it is probably not coincidence that during the progression from three-stone to Chulika to Oorja, greater efficiency is accompanied by the production of PM with higher relative EC content. This is likely due to the more complete combustion of OC in the more efficient cookstoves and is discussed later. A second discussion point concerns the DustTrak estimation errors indicated by Table 8: 172% overestimation for the three-stone fire, 21% overestimation for the Chulika, and 16% underestimation for the Oorja. For the three-stone fire, the DustTrak greatly overestimates PM. Since the DustTrak estimates PM based on a light scattering, high OC (low EC) content would tend to increase scattering relative to the calibration material (Arizona Road Dust) and result in overestimation. For the Chulika, the DustTrak also overestimated actual PM, but by a narrow margin. The DustTrak underestimated PM from the Oorja, possibly due to its higher relative EC content and the subsequent reduction in scattering due to the presence of more absorbing material. Difference in particle size may also be a factor and is discussed later.

3.3.4 Carbon balance

By using the estimated TC/PM factor (γ) for each stove type (calculated in the previous section), PM is more accurately accounted for in the carbon balance. Thus Table 7, which reported gaseous combustion products only by percentage of carbon, is updated to yield Table 11, which is graphically represented in Figure 19.*

Table 11. Summary of combustion products, by percentage of carbon going to formation of a particular product

	Three-stone	Chulika	Oorja
CO ₂	87.4	97.3	97.6
CO	9.1	2.4	2.3
CH ₄	0.9	0 ^a	0 ^a
NMHC	1.4	0 ^a	0 ^a
PM	1.2	0.3	0.1

^a Not clearly distinguishable from background data.

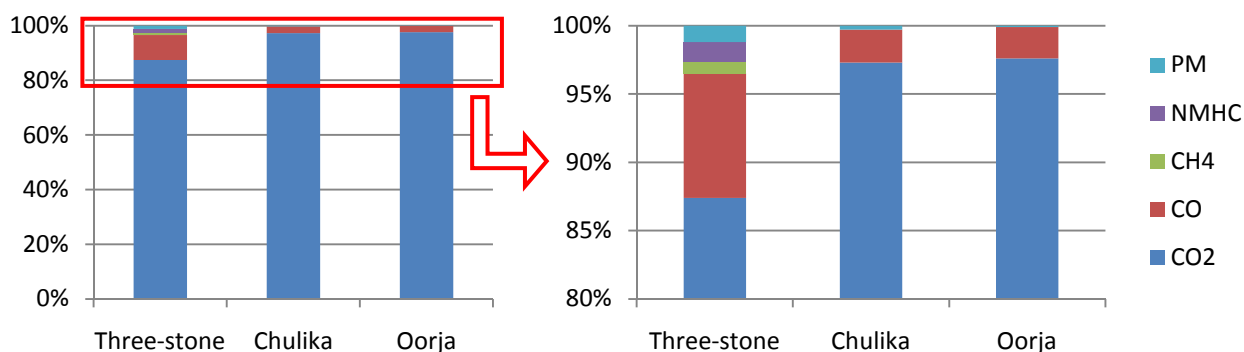


Figure 19. Graphical representation of carbon-containing combustion products

Emissions factors are estimated for CO₂ and all PICs in terms of grams per kg of dry fuel; see Table 12.[†] A brief selection of other published results is shown in the rightmost column; the figures are generally in agreement with the present study. These EFs should only be interpreted with consideration to cookstove efficiency; e.g., the fact that the Oorja outputs more CO₂ per kg-fuel burned is meaningless without accounting for the (potentially high) reduction in fuel usage that Oorja usage may permit.[‡] Refer to Appendix N for further discussion in addition to commentary on global warming potential (GWP) differences between stoves.

* Mass of char at the end of tests was not measured, but was small relative to the mass of fuel consumed. By definition, all carbon mass is assumed to go into (only) the products listed in Table 11.

[†] This is easily converted from terms of dry fuel mass to either carbon mass or wet fuel mass using the fuel carbon and moisture contents reported earlier.

[‡] Detailed efficiency comparison is beyond the scope of this study.

Table 12. Emissions factors, g/kg-dry fuel

Compound	Three-stone	Chulika	Oorja	Reference (g/kg-fuel)
CO ₂	1524	1695	1707	
CO	101	26.9	25.1	166 ^b (trad), 46 ^b (imp)
CH ₄	5.63	negl.	negl.	
NMHC ^a	9.87	negl.	negl.	
PM:	8.44	2.38	0.86	8.5 ^b (trad), 5.6 ^b (imp)
OC	3.98	0.32	0.22	4.0 ^b (trad), 1.7 ^b (imp)
EC	0.70	1.27	0.52	1.5 ^b (trad), 3.1 ^b (imp) 0.88 ^c (3s), 1.16 ^c (rocket), 0.28 ^c (gas)

^a 18 g/mol of NMHC is assumed in accordance with (K. Smith et al. 2000).

^b Average of 11 traditional (trad) stoves and a single improved (imp) stove (Roden et al. 2006).

^c From a three-stone (3s), rocket, and gasifier (gas) stove (MacCarty et al. 2008).

Interestingly, while overall PM emission rates vary significantly, EC emission rates are fairly uniform. Most PM from the highly polluting three-stone fire is attributed to OC.

3.3.5 PM size distributions

Results from real-time instruments are used to normalize data based on the quantity of carbon burned during each SMPS scanning period. The area under each curve in Figure 20(a) is proportional to the total number of particles emitted. * Figure 20(b) displays the data in a different way; cumulative values for the averaged data for each bin are normalized to the highest total emitter (three-stone).

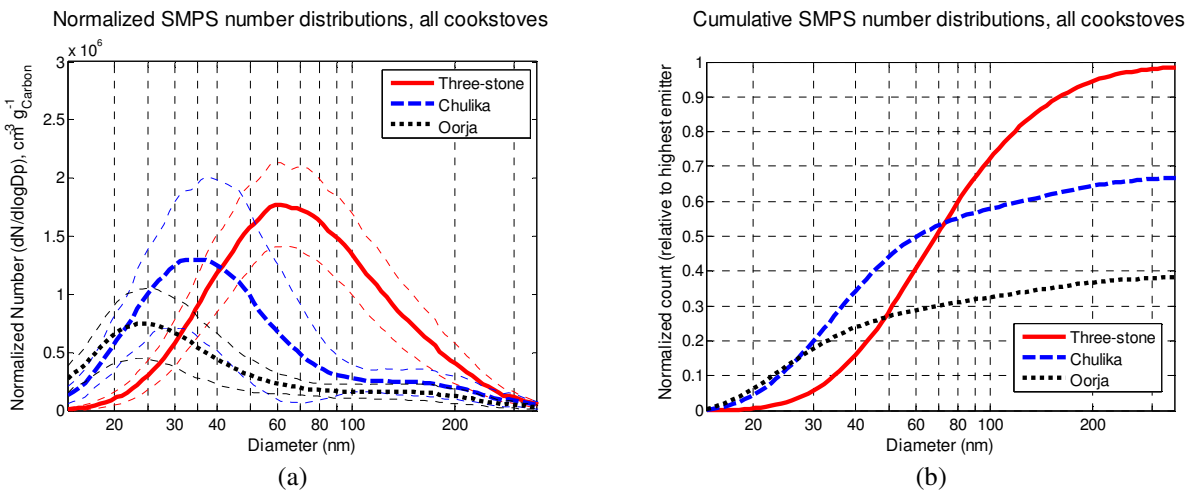


Figure 20. (a) Normalized SMPS number distribution; standard deviation of the average value for each size bin is represented by “error bands” of the corresponding color [Oorja: N=36 (scans), Chulika: N=67; Three-stone: N=68]. (b) Cumulative distribution normalized to highest emitter (three-stone). Data for diameters smaller than 350 nm is displayed. All diameters are based on electrical mobility.

* SMPS scans were also used to define the steady-state portion of tests as discussed previously. See Appendix O for individual scans / distributions, further explanation on methodology, and information on repeatability.

The three-stone fire emits the most particles, but quantities are well within an order of magnitude; the Oorja and Chulika emit approximately 40% and 70%, respectively, of the normalized particle count of the three-stone. There is, however, a clear shift to *smaller* particles during the progression from the relatively inefficient three-stone fire to the improved cookstoves. Figure 20(a) indicates that the mode of three-stone PM emissions is approximately 60 nm, while it is about 35 nm for the Chulika and 25 nm for the Oorja. The normalized cumulative distribution in Figure 20(b) shows that both improved stoves emit approximately *four times* the quantity of sub-30 nm particles emitted by the three-stone fire.

Combining SMPS data (for diameters under 350 nm) with APS results yields the distributions in Figure 21 in which it is evident that there is little contribution from larger (larger than 350 nm) particles.* Even the three-stone fire, which emits considerably more PM by mass compared with the improved stoves, appears to have relatively little overall PM content in this larger size range.

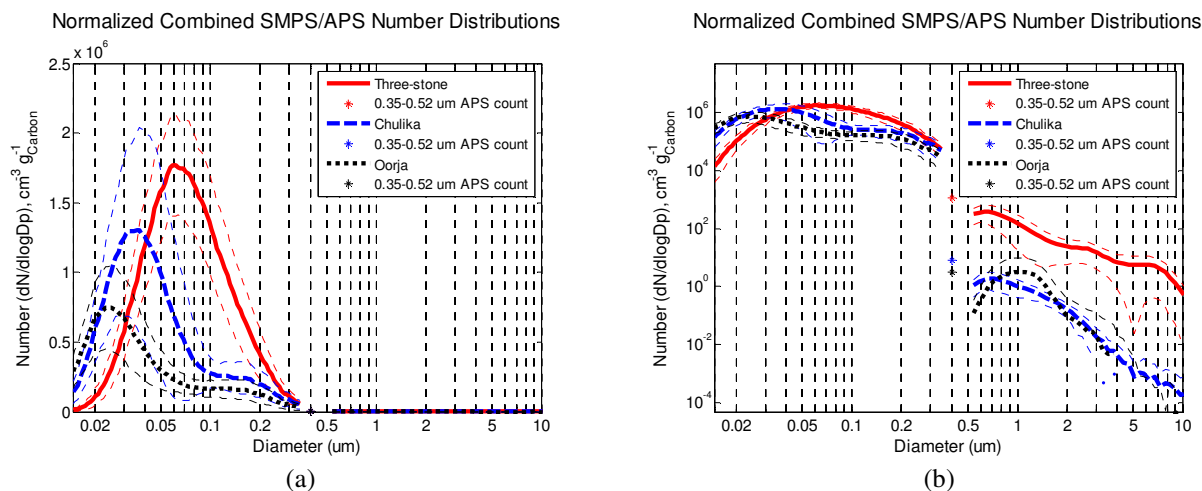


Figure 21. Normalized SMPS+APS distributions by number on a (a) linear and (b) log y-scale. Standard deviation of the average value for each size bin is represented by “error bands” of the corresponding color [Oorja: $N=36$ (scans), Chulika: $N=67$; Three-stone: $N=68$]. Diameter is based on electrical mobility. 0.35 – 0.52 μm (total) counts given by the APS are also normalized and displayed.†

During follow-up testing (see Appendix P), it was discovered that the fan setting on the Oorja can significantly affect the particle size distribution. This is discussed in more detail in Appendix Q.

* The loss of large particles in the sampling system could be significant due to bends and elbows in the lines, but this is not investigated in detail since the focus of the study is ultrafine PM.

† Appendix P reproduces these plots alongside their mass-based equivalents.

3.3.6 PM imaging

Three TEM grids collected during test series #1, 2, and 4 are analyzed for each cookstove. Figure 22 shows representative images for each of the three cookstoves at 15,000x magnification (see Appendix R for further details on protocol, grid identification, PM loading, and a catalogue of images).

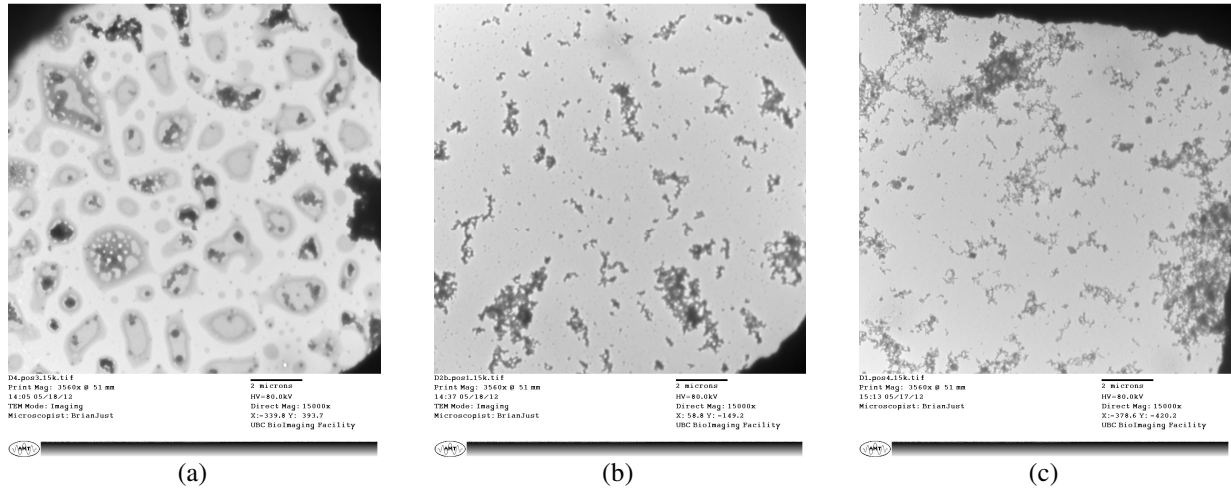


Figure 22. Example TEM imaging at 15k magnification; (a) three-stone, (b) Chulika, (c) Oorja

Qualitatively, there are obvious differences. Three-stone images consistently indicate what appear to be “oily,” evaporated droplets of volatile material with darker PM left behind. The improved cookstoves display spheres and chain agglomerates; at this level of magnification, there does not seem to be a large difference between them. At 150,000x magnification, more details emerge; see Figure 23.

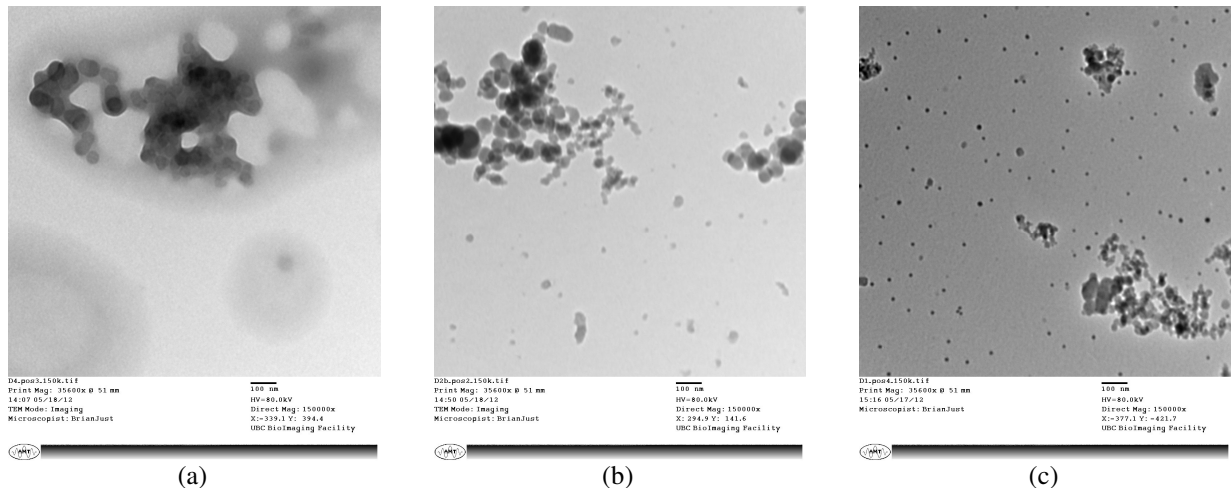


Figure 23. Example TEM imaging at 150k magnification; (a) three-stone, (b) Chulika, (c) Oorja

The (typical) three-stone image presented here is likely blurred due to its greater depth and/or residue left behind by evaporated material. The agglomerate is comprised of primary particles (spheres) that appear larger than those of the Chulika and Oorja images. The latter two display a tendency for similarly sized agglomerates; the Oorja appears to have smaller primary particle for both independent spheres and components of agglomerates.

300,000x was the highest magnification used with consistently good focus and is employed for most measurement of primary particle sizes, though selected 500,000x images are also analyzed. Figure 24 shows four representative examples. Appendix S provides detailed information on measurements corresponding to the indicated identification numbers and includes a catalogue of images analyzed.

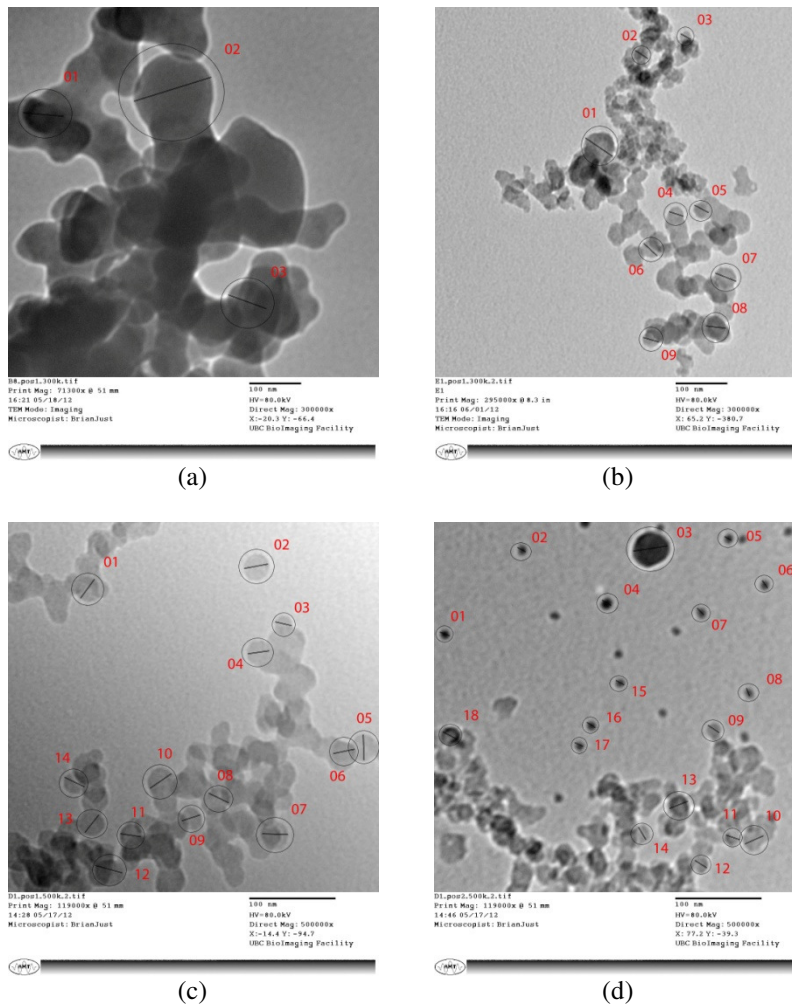


Figure 24. Example TEM imaging and primary particle (of agglomerates) sizing at high magnification; (a) three-stone at 300kx, (b) Chulika at 300kx, (c) Oorja at 500kx; (d) shows a number of individual primary particles for the Oorja at 500kx.

Focus was on sizing primary particles that form the building blocks of agglomerates since it was not easy to isolate a large number of individual primary particles for all stove types. Results of this sizing are displayed in Table 13.

Table 13. Average particle size within agglomerates (error based on standard deviation)

Cookstove	Avg particle size, nm	N
Three-stone	57.7 ± 23.6	52
Chulika	46.1 ± 19.2	83
Oorja	27.2 ± 10.5	105

It is important to note that it is not straightforward to distinguish small particles in some agglomerates, e.g., the mid-upper portion of Figure 24(b). This may bias results towards (larger) particles with more defined boundaries. For all images, it is possible that particles counted as components of agglomerates are actually independent particles that collided with an agglomerate on the TEM grid. At first glance, there appear to be lower quantities of nanoparticles (relative to the number of agglomerates) than predicted based on SMPS data; some agglomerates probably deposit via impaction.* Because of the relatively small number of TEM grids / agglomerates analyzed, it is overly presumptive to state that TEM imaging validates the particle size distributions reported by the SMPS. However, it is probably not coincidental that measurements are in close agreement with the size distribution summary of Figure 20, in which the modes are approximately 60 nm, 35 nm, and 25 nm for the three-stone, Chulika, and Oorja, respectively. Much of the sub-100 nm content from the SMPS data is likely composed of particles that are essentially spherical and not part of agglomerates.

Two key observations are noted from TEM imaging. First, for the three-stone, high OC content is suggested by the “oiliness” of the images and the fact that there is visual evidence of much evaporated volatile material; clumps / clusters of what appears to be (formerly) internally mixed EC are left behind. In comparison, both improved stoves show primarily clearly defined chain agglomerates and independent spheres (refer to Figure 1 and Figure 2) with little evidence of volatile matter.

Second, the Oorja appears to produce more small clearly defined spheres seen in Figure 24(d) than are evident in images from the other stoves. Though relatively few of these were measured, the Oorja spheres were 12.4 ± 6.4 nm (N=50) while Chulika spheres were 21.9 ± 5.0 nm (N=8).† Commentary on the Oorja’s tendency to produce more independent particles (that did not coagulate) appears below.

* Recall from Appendix F that the d_{50} for impaction deposition in the TPS with the present operating conditions is ~300 nm. This calculation was based on aerodynamic diameter, the size of a water drop with the same drag/mass ratio as the particle of interest. The non-spherical nature of soot agglomerates means that aerodynamic diameter can be significantly smaller than mobility diameter (the basis of the SMPS measurement).

† Few independent spheres were measured for the three-stone and standard deviation was very high; results are not reported here but appear in Appendix S.

It is beyond the scope of this work to comment on differences (if any, once accounted for statistically) in the size of the primary particles produced by different cookstoves.

3.4 Additional discussion

3.4.1 Commentary on particle size

The improved cookstoves exhibit higher combustion efficiency and produce far fewer PICs than the three-stone fire. Normalized and corrected PM emission concentrations by mass were 8.25, 3.81, and 1.18 mg/m³ for the three-stone, Chulika, and Oorja, respectively. Despite this reduction in mass, the increased quantities of smaller particles (e.g., those smaller than 30 nm) would present health concerns should these particles prove capable of deeper penetration into the cardio-respiratory system than particles of greater diameter, as may be suggested by some of the research summarized in section 1.2.2. The combination of potentially more harmful, deeply inhalable particles and the body's ability to filter certain sizes (recall Figure 3) may yield a size range (e.g., 10-30 nm) of particles best avoided. This is a question for further study by health scientists.

Particles resident in the atmosphere for long periods of time are expected to undergo changes in size, composition, mixing state, etc. How long these ultrafine particles remain in the atmosphere and retain their small size may be relevant for certain climate considerations. But regarding human health, it must be emphasized that the path the particles took from the cookstove to PM monitoring instruments (via the exhaust system) is much longer than the typical path from cookstove to a human tending it (a distance of perhaps a meter or less) or other humans in the same building. Conversely, it is also worth noting that most cookstove users will not stand directly in the plume, so inhaled particles are not necessarily the same as the ones measured here.

For another perspective, Wallace et al. reported a geometric mean particle size of 8.8 ± 1.5 nm in a series of tests with a gas burner used to boil 350 mL of water in a saucepan (2008).^{*} Since gas stoves are considered an efficient and “clean” combustion-based alternative to biomass, it is interesting to note that efficiency gains (more complete combustion) correspond to emissions of smaller particles (albeit in much lower quantity by mass). From a health standpoint, this should be considered in the context of Figure 3, which indicates that below 10 nm, nasal passages are more effective at preventing particles from reaching the lungs, with a resulting drop in alveolar deposition.

3.4.2 Commentary on EC/OC content

Table 10 indicates a trend of increasing particle “blackness” (higher relative EC content) during the progression from three-stone to Chulika to Oorja. From a climate perspective, this suggests that large-scale deployment of improved cookstoves has potential to influence the earth's radiative balance due to the displacement of large quantities of highly scattering OC from three-stone fires (recall from Table 12 that *overall* EC quantities emitted are

^{*} The test took place in a North American kitchen and used an SMPS; gas content was not specified. Peak concentrations and emissions rate are not comparable because test conditions were considerably different.

fairly uniform across the different stoves), though any such effect is likely small and must be combined with considerations to particle size and morphology.

TEM imaging seems to support the measurement of high volatile / OC content from the three-stone fire (and accompanying lower combustion efficiency) relative to the improved cookstoves. Fuel for all stoves had similar chemical content. Given that the three-stone fire is uncontrolled in time and temperature, pockets of volatile and pyrolyzed material may be quenched before there is a chance to further oxidation, with resulting larger particle sizes and higher OC content. This could be especially true given the large fluctuations in combustion conditions in the open fire. Also, lower combustion temperature likely means the existence of more solid fuel in the emissions (larger size, more OC). Meanwhile, both improved stoves direct combustion products through a hotter combustion chamber (temperature, geometry), and for longer periods (time) that further improve combustion by "smoothing out" fluctuations that occur in the traditional fire.* Increased temperature and time of combustion (i.e., exposure to higher temp and more O₂) promotes more oxidation of carbon and decomposition of organics. The resulting products are smaller and are composed of more of the non-OC fraction of carbon.

3.4.3 Relevance of size and composition for scattering-based instruments

As discussed previously, the large difference between DustTrak and corrected PM results (Table 8) indicates a need to consider EC/OC content when using a scattering-based PM estimation device (such as a DustTrak or nephelometer) to quantify PM across different cookstove types. Particle size should also be considered. Given that scattering intensity is proportional to the sixth power of particle diameter, one may expect that emissions with larger particles (e.g., three-stone fire) would be over-predicted relative to cookstoves that produce smaller particles (e.g., the two improved stoves tested). Further tests would be required to determine the relative contributions of size and EC/OC content on scattering-based PM mass measurements.

3.5 Recommended future work

Study of the implications of this research is warranted for both climate and health scientists. Other research could explore novel ways to exhaust, deposit, or collect potentially harmful ultrafine particles.

Future work at the UBC cookstove laboratory should include investigation of "full power" vs. "simmer" modes of operation. This study focused on a simmer / low boil condition. In the real world, often a fire is stoked in order to boil water, cook, or heat space rapidly. Also, in the preceding text it was briefly noted that the Oorja cookstove emits particles with different characteristics dependent on operating conditions and combustion chamber temperature. Further investigation that defines discrete operating points / conditions and takes full sets of data (including quartz filters for EC/OC analysis) could provide valuable information. The start-up and smouldering

* Both have a tall, insulated combustion chamber. The Oorja improves on this by adding a forced (externally powered) air supply of fresh air to the combustion region.

phases of the complete burn cycle (see (Roden et al. 2006)) could be investigated in further detail to better characterize a full burn cycle.

It would also be worthwhile to use the existing experimental setup to test a gas burner, potentially with the inclusion of efficiency testing (e.g., to present particle counts under 30 nm per cooking task or unit of heat delivered, similar to how other EFs are reported in standardized tests like WBT 4.1.2).

Other tasks could include the study of other fuels and moisture contents to confirm whether similar trends are observed as in this research. Alternative cookstove models could be tested, especially ones that gain prominence or widespread distribution. An investigation of the relative contributions of particle size and EC/OC content to the light scattering-based over- and underestimations of PM mass would also be interesting.

Finally, previous research has studied the morphological properties of ultrafine atmospheric aerosols, e.g., (Xiong and Friedlander 2001), but a focused effort on cookstove emissions that more fully characterizes primary spheres and agglomerates would also be valuable. This could include a search for more primary spheres, the counting of statistically significant quantities of particles, and higher magnifications in order to further investigate structure and the differences between particles from discrete cookstoves (and/or operating conditions).

4 Conclusions

The study focused on a comparative, repeatable analysis of emissions from steady-state burn events with a three-stone fire and two improved cookstoves. Experiments mimicking actual fuels / cooking events or consideration to the likelihood of successful adoption are beyond the scope of the project.

The improved cookstoves demonstrated high combustion efficiency compared to the three-stone fire. Given that they are also designed to better focus energy onto a recipient vessel, the goal of reduction in biomass fuel usage is likely. The improved stoves reduced PM mass by a significant amount. However, there was a shift towards greater quantities of smaller nanometer-sized particles. This could have health implications and is a point for further consideration by health scientists (with further attention to composition shifts in those smaller particles) and also reinforces the need for adequate ventilation for *all* cookstoves, independent of type.

Particles from the improved stoves were smaller than those emitted by the three-stone fire and appeared slightly less likely to coagulate into chain agglomerates. PM emissions from improved stoves emitted a higher proportion of EC compared with total PM, with relatively little variation in overall EC levels. The reduction in highly scattering OC that would accompany a large-scale shift towards the usage of improved stoves could have an effect on the earth's radiative balance, but this would have to be investigated with consideration to other characteristics such as size and morphology.

References

- Andreatta, Dale. 2007. "A Report on Some Experiments with the Top-Lit Up Draft (TLUD) Stove". Presented at the ETHOS 2007 Conference, Kirkland, Washington, January 27, 2007.
http://bioenergylists.org/stovesdoc/Andreatta/TLUD_Report.pdf, accessed 18 July 2012.
- Anon. 2009. "The Water Boiling Test, Version 4.1.2 (DRAFT)". Maintained by the Partnership for Clean Indoor Air; the WBT can be used, produced, and disseminated without permission.
http://www.pciaonline.org/files/WBT4.1.2_0.pdf, accessed 18 July 2012.
- Auger, Floriane, Marie-Claude Gendron, Christophe Chamot, Francelyne Marano, and Anne-Catherine Dazy. 2006. "Responses of Well-differentiated Nasal Epithelial Cells Exposed to Particles: Role of the Epithelium in Airway Inflammation." *Toxicology and Applied Pharmacology* 215 (3) (September 15): 285–294.
- Azong-Wara, Nkwenti, Christof Asbach, Burkhard Stahlmecke, Heinz Fissan, Heinz Kaminski, Sabine Plitzko, and Thomas A. J. Kuhlbusch. 2009. "Optimisation of a Thermophoretic Personal Sampler for Nanoparticle Exposure Studies." *Journal of Nanoparticle Research* 11 (7) (August): 1611–1624.
- Ballard-Tremere, G, and H H Jawurek. 1999. "The 'Hood Method' of Measuring Emissions of Rural Cooking Devices." *Biomass and Bioenergy* 16 (5): 341–345.
- Bang, John J., Elizabeth A. Trillo, and Lawrence E. Murr. 2003. "Utilization of Selected Area Electron Diffraction Patterns for Characterization of Air Submicron Particulate Matter Collected by a Thermophoretic Precipitator." *Journal of the Air & Waste Management Association* 53 (February): 227–236.
- Berry, J P, B Arnoux, G Stanislas, P Galle, and J Chretien. 1977. "A Microanalytic Study of Particles Transport Across the Alveoli: Role of Blood Platelets." *Biomedicine / [publiée Pour l'A.A.I.C.I.G.]* 27 (9-10) (December): 354–357.
- Bond, Tami C., David G. Streets, Kristen F. Yarber, Sibyl M. Nelson, Jung-Hun Woo, and Zbigniew Klimont. 2004. "A Technology-based Global Inventory of Black and Organic Carbon Emissions from Combustion." *Journal of Geophysical Research* 109 (July 24): 43 PP.
- Brockman, John E. 2001. "Sampling and Transport of Aerosols." In *Aerosol Measurement : Principles, Techniques, and Applications*, eds. Paul A. Baron and Klaus Willeke. 2nd ed. New York: Wiley.
- Brown, D.M., M.R. Wilson, W. MacNee, V. Stone, and K. Donaldson. 2001. "Size-Dependent Proinflammatory Effects of Ultrafine Polystyrene Particles: A Role for Surface Area and Oxidative Stress in the Enhanced Activity of Ultrafines." *Toxicology and Applied Pharmacology* 175 (3) (September 15): 191–199.
- Cox, Prentiss. 2011. "Analysis of Cookstove Change-Out Projects Seeking Carbon Credits." *SSRN eLibrary* (May 12).
- Dixkens, J., and H. Fissan. 1999. "Development of an Electrostatic Precipitator for Off-Line Particle Analysis." *Aerosol Science and Technology* 30 (5): 438.
- Engineers in Technical and Humanitarian Opportunities of Service. 2012. "About ETHOS."
<http://www.vrac.iastate.edu/ethos/index.php>, accessed 18 July 2012.
- Environment Canada. 2012. "Particulate Matter." <http://www.ec.gc.ca/air/default.asp?lang=En&n=2C68B45C-1>, accessed 18 July 2012.
- Fan, C W, and J J Zhang. 2001. "Characterization of Emissions from Portable Household Combustion Devices: Particle Size Distributions, Emission Rates and Factors, and Potential Exposures." *Atmospheric Environment* 35 (7): 1281–1290.
- Flagan, Richard C., and John H. Seinfeld. 1988. *Fundamentals of Air Pollution Engineering*. Englewood Cliffs, New Jersey: Prentice-Hall, Inc. <http://resolver.caltech.edu/CaltechBOOK:1988.001>, accessed 18 July 2012.
- Forster, Piers, Venkatachalam Ramaswamy, Paulo Artaxo, Terje Berntsen, Richard Betts, and et al. 2007. "Changes in Atmospheric Constituents and in Radiative Forcing." In *Climate Change 2007: The Physical Science Basis. Contribution of Working Group I to the Fourth Assessment Report of the Intergovernmental Panel on Climate Change*. Cambridge, United Kingdom and New York, NY, USA: Cambridge University Press.
- Goudie, A.S., and N.J. Middleton. 2001. "Saharan Dust Storms: Nature and Consequences." *Earth-Science Reviews* 56 (1–4) (December): 179–204.
- Grieshop, Andrew P., Julian D. Marshall, and Milind Kandlikar. 2011. "Health and Climate Benefits of Cookstove Replacement Options." *Energy Policy* 39 (12) (December): 7530–7542.
- Guofeng, Shen, Wei Siye, Wei Wen, Zhang Yanyan, Min Yujia, Wang Bin, Wang Rong, et al. 2012. "Emission Factors, Size Distributions, and Emission Inventories of Carbonaceous Particulate Matter from Residential Wood Combustion in Rural China." *Environ. Sci. Technol.* 46 (7): 4207–4214.

- H.L. Green, and H.H. Watson. 1935. *Physical Methods for the Estimation of the Dust Hazard in Industry (with Special Reference to the Occupation of the Stonemason)*. Med. Res. Council Spec. Rept. His Majesty's Stationary Office, London.
- Hansen, A.D.A. 2005. *The Aethalometer*. Magee Scientific Company.
- Hendrix, Warren P., and Clyde Orr. 1964. "Thermal Precipitator." *Review of Scientific Instruments* 35 (10): 1373.
- Hinds, William. 1999. *Aerosol Technology: Properties, Behavior, and Measurement of Airborne Particles*. 2nd ed. New York: Wiley.
- ICRP. 1994. *Human Respiratory Tract Model for Radiological Protection*. ICRP Publication 66. Ann. ICRP 24 (1-3).
- Intergovernmental Panel on Climate Change. 2007. *Fourth Assessment Report: Working Group I: The Physical Basis for Climate Change*. Geneva, Switzerland.
- Janara Samuha Mutual Benefit Trust. 2010. "Clean Development Mechanism Project Design Document Form: Improved Cook Stoves CDM Project of JSMBT, V.1.1". United Nations Framework Convention on Climate Change (UNFCCC). <http://cdm.unfccc.int/Projects/Validation/DB/5PSUAXL0K3TOHZ7AO3DMCH0T6ZAT7U/view.html>, accessed 18 July 2012.
- Jawurek, H H, and Ballard-Tremeer. 1999. "Evaluation of the Dilution Chamber Method for Measuring Emissions of Cooking Devices." *Biomass Bioenergy* 17 (6): 481–494.
- Jetter, J J, and P. Kariher. 2009. "Solid-fuel Household Cook Stoves: Characterization of Performance and Emissions." *Biomass and Bioenergy* 33 (2): 294–305.
- Jetter, Jim. 2011. "What's Hot in Cook Stove Testing, Fuels, and Technology." http://www.pciaonline.org/files/Tuesday_Exciting_New_Developments_Jetter.pdf, accessed 18 July 2012.
- Jones, Heather. 2009. "Single Cylinder Research Engine (SCRE) Users Manual, Rev. E". Department of Mechanical Engineering, University of British Columbia.
- Kar, Abhishek, Ibrahim H. Rehman, Jennifer Burney, S. Praveen Puppala, Ramasubramanyaiyer Suresh, Lokendra Singh, Vivek K. Singh, Tanveer Ahmed, Nithya Ramanathan, and Veerabhadran Ramanathan. 2012. "Real-Time Assessment of Black Carbon Pollution in Indian Households Due to Traditional and Improved Biomass Cookstoves." *Environ. Sci. Technol.* 46 (5): 2993–3000.
- Kasper, Gerhard. 1982. "Hot-wire Thermal Precipitator with Low Inlet Losses and Low Size Selectivity." *Review of Scientific Instruments* 53 (1): 79.
- Kethley, T. W., M. T. Gordon, and Clyde Orr. 1952. "A Thermal Precipitator for Aerobacteriology." *Science* 116 (3014). New Series (October 3): 368–369.
- Kittelson, D.B., W.F. Watts, and J.P. Johnson. 2006. "On-road and Laboratory Evaluation of Combustion Aerosols, Part 1: Summary of Diesel Engine Results." *Journal of Aerosol Science* 37 (8) (August): 913–930.
- Lagally, Christie D. 2011. "A Morphological Survey of Particulate Matter Emissions from Spark-ignited Engines". Vancouver, BC: The University of British Columbia.
- Lighty, JoAnn Slama, John M. Veranth, and Adel F. Sarofim. 2000. "Combustion Aerosols: Factors Governing Their Size and Composition and Implications to Human Health." *Journal of the Air & Waste Management Association* 50 (9) (September 1): 1565–1618.
- Lin, Jyh-Shyan, and Chuen-Jinn Tsai. 2003. "Thermophoretic Deposition Efficiency in a Cylindrical Tube Taking into Account Developing Flow at the Entrance Region." *Journal of Aerosol Science* 34 (5) (May): 569–583.
- Lipsky, Eric M., and Allen L. Robinson. 2006. "Effects of Dilution on Fine Particle Mass and Partitioning of Semivolatile Organics in Diesel Exhaust and Wood Smoke." *Environmental Science & Technology* 40 (1) (January 1): 155–162.
- Lorenzo, R., R. Kaegi, R. Gehrig, L. Scherrer, B. Grobety, and H. Burtscher. 2007. "A Thermophoretic Precipitator for the Representative Collection of Atmospheric Ultrafine Particles for Microscopic Analysis." *Aerosol Science and Technology* 41 (10): 934.
- MacCarty, N., D. Ogle, D. Still, T. Bond, and C. Roden. 2008. "A Laboratory Comparison of the Global Warming Impact of Five Major Types of Biomass Cooking Stoves." *Energy for Sustainable Development* 12 (2) (June): 56–65.
- Maynard, Andrew D. 1995. "The Development of a New Thermophoretic Precipitator for Scanning Transmission Electron Microscope Analysis of Ultrafine Aerosol Particles." *Aerosol Science and Technology* 23 (4): 521.
- Menon, Surabi, James Hansen, Larissa Nazarenko, and Yunfeng Luo. 2002. "Climate Effects of Black Carbon Aerosols in China and India." *Science* 297 (5590) (September 27): 2250–2253.

- Messerer, A., R. Niessner, and U. Pöschl. 2003. "Thermophoretic Deposition of Soot Aerosol Particles Under Experimental Conditions Relevant for Modern Diesel Engine Exhaust Gas Systems." *Journal of Aerosol Science* 34 (8) (August): 1009–1021.
- Miller, A., G. Frey, G. King, and C. Sunderman. 2010. "A Handheld Electrostatic Precipitator for Sampling Airborne Particles and Nanoparticles." *Aerosol Science and Technology* 44 (6): 417–427.
- Naeher, Luke P., Michael Brauer, Michael Lipsett, Judith T. Zelikoff, Christopher D. Simpson, Jane Q. Koenig, and Kirk R. Smith. 2007. "Woodsmoke Health Effects: A Review." *Inhalation Toxicology* 19 (1) (January): 67–106.
- Oberdörster, G. 2007. "Biokinetics and Effects of Nanoparticles." In *Nanotechnology – Toxicological Issues and Environmental Safety and Environmental Safety*, ed. P. Simeonova, N. Opopol, and M. Luster, 28:15–51. NATO Security Through Science Series. Springer Netherlands. <http://www.springerlink.com/content/v300k8n1mg818484/abstract/>, accessed 18 July 2012.
- Peters-Stanley, Molly, and Katherine Hamilton. 2012. *Developing Dimension: State of the Voluntary Carbon Markets 2012*. Ecosystem Marketplace & Bloomberg New Energy Finance. http://www.forest-trends.org/documents/files/doc_3164.pdf, accessed 18 July 2012.
- Pope, Daniel P., Vinod Mishra, Lisa Thompson, Amna Rehana Siddiqui, Eva A. Rehfuess, Martin Weber, and Nigel G. Bruce. 2010. "Risk of Low Birth Weight and Stillbirth Associated With Indoor Air Pollution From Solid Fuel Use in Developing Countries." *Epidemiologic Reviews* 32 (1) (April 1): 70–81.
- Rehman, I. H., T. Ahmed, P. S. Praveen, A. Kar, and V. Ramanathan. 2011. "Black Carbon Emissions from Biomass and Fossil Fuels in Rural India." *Atmospheric Chemistry & Physics* 11 (July 1): 7289–7299.
- Renwick, L C, D Brown, A Clouter, and K Donaldson. 2004. "Increased Inflammation and Altered Macrophage Chemotactic Responses Caused by Two Ultrafine Particle Types." *Occupational and Environmental Medicine* 61 (5) (May 1): 442–447.
- Reynolds, Conor C. O., and Milind Kandlikar. 2008. "Climate Impacts of Air Quality Policy: Switching to a Natural Gas-Fueled Public Transportation System in New Delhi." *Environmental Science & Technology* 42 (16): 5860–5865.
- Roden, C A, T C Bond, S. Conway, A B Osorto Pinel, N. Maccarty, and D. Still. 2009. "Laboratory and Field Investigations of Particulate and Carbon Monoxide Emissions from Traditional and Improved Cookstoves." *Atmospheric Environment* 43 (6): 1170–1181.
- Roden, C. A., Tami C. Bond, Stuart Conway, and Anibal Benjamin Osorto Pinel. 2006. "Emission Factors and Real-Time Optical Properties of Particles Emitted from Traditional Wood Burning Cookstoves." *Environmental Science & Technology* 40 (21) (November 1): 6750–6757.
- Schlecht, P.C., and P.F. O'Connor, eds. 2003. "Elemental Carbon (Diesel Particulate): Method 5040, Issue 3." In *NIOSH Manual of Analytical Methods (NMAM)*, DHHS (NIOSH) Publication 94–113 (August, 1994), 1st Supplement Publication 96–135, 2nd Supplement Publication 98–119, 3rd Supplement 2003–154. 4th ed. National Institute for Occupational Safety and Health. <http://www.cdc.gov/niosh/docs/2003-154/pdfs/5040.pdf>, accessed 18 July 2012.
- Seinfeld, John H., and Pandis, Spyros N. 2006. *Atmospheric Chemistry and Physics: From Air Pollution to Climate Change*. 2nd ed. Hoboken N.J.: J. Wiley.
- Shrimali, Gireesh, Xander Slaski, Mark C. Thurber, and Hisham Zerriffi. 2011. "Improved Stoves in India: A Study of Sustainable Business Models." *Energy Policy* 39 (12) (December): 7543–7556.
- Smith, Kirk R., and Evan Haigler. 2008. "Co-Benefits of Climate Mitigation and Health Protection in Energy Systems: Scoping Methods." *Annual Review of Public Health* 29 (1) (April): 11–25.
- Smith, KR, R Uma, VVN Kishore, K Lata, V Joshi, Z Zhang, RA Rasmussen, and MAK Khalil. 2000. *Greenhouse Gases from Small-scale Combustion Devices in Developing Countries, Phase IIa: Household Stoves in India*. Washington, D.C.: U.S. Environmental Protection Agency, Office of Air and Radiation. http://ehs.sph.berkeley.edu/krsmith/publications/00_smith_3.pdf, accessed 18 July 2012.
- Still, D., and L. Winiarski. 2001. "Increasing Fuel Efficiency and Reducing Harmful Emissions in Traditional Cooking Stoves." *Boiling Point* 47: 36–39.
- Sunset Laboratory. 2010. "Sample Analysis Method for Organic and Elemental Carbon Aerosols." <http://www.sunlab.com/uploads/assets/product/Sunset%20Lab%20Analysis%20Method.pdf>, accessed 18 July 2012.
- Talbot, L., R. K. Cheng, R. W. Schefer, and D. R. Willis. 1980. "Thermophoresis of Particles in a Heated Boundary Layer." *Journal of Fluid Mechanics* 101 (04): 737–758.

- Thayer, D., K. A. Koehler, A. Marchese, and J. Volckens. 2011. "A Personal, Thermophoretic Sampler for Airborne Nanoparticles." *Aerosol Science and Technology* 45 (6): 734.
- The Partnership For Clean Indoor Air. 2012. "About PCIA." <http://www.pciaonline.org/node/2>, accessed 18 July 2012.
- Tillman, D. A., A. J. Rossi, and W. D. Kitto. 1981. *Wood combustion. Principles, processes, and economics*. New York, N.Y.: Academic Press.
- Tsai, Chuen-Jinn, and Hsin-Chung Lu. 1995. "Design and Evaluation of a Plate-to-Plate Thermophoretic Precipitator." *Aerosol Science and Technology* 22 (2): 172.
- TSI Incorporated. 2012. *Model 8533/8534 DustTrak DRX Aerosol Monitor: Operation and Service Manual, Revision G*. Shoreview, MN.
- Turpin, Barbara J., James J. Huntzicker, and Susanne V. Hering. 1994. "Investigation of Organic Aerosol Sampling Artifacts in the Los Angeles Basin." *Atmospheric Environment* 28 (19) (November): 3061–3071.
- United Nations Foundation. 2012. "Global Alliance for Clean Cookstoves." Accessed July 18. <http://cleancookstoves.org/the-alliance/>, accessed 18 July 2012.
- United Nations Framework Convention on Climate Change. 2012. "About CDM." <http://cdm.unfccc.int/about/index.html>, accessed 18 July 2012.
- US Department of State. 2012. "The U.S. Commitment." *The U.S. Commitment*. <http://www.state.gov/s/partnerships/cleancookstoves/commitment/index.htm>, accessed 18 July 2012.
- Venkataraman, C., G. Habib, A. Eiguren-Fernandez, A. H. Miguel, and S. K. Friedlander. 2005. "Residential Biofuels in South Asia: Carbonaceous Aerosol Emissions and Climate Impacts." *Science* 307 (5714): 1454–1456.
- Wallace, Lance, Fang Wang, Cynthia Howard-Reed, and Andrew Persily. 2008. "Contribution of Gas and Electric Stoves to Residential Ultrafine Particle Concentrations Between 2 and 64 Nm: Size Distributions and Emission and Coagulation Rates." *Environmental Science & Technology* 42 (23): 8641–8647.
- Wen, Jian, and Anthony S. Wexler. 2007. "Thermophoretic Sampler and Its Application in Ultrafine Particle Collection." *Aerosol Science and Technology* 41 (6): 624.
- WHO. 2009. *Global Health Risks: Mortality and Burden of Disease Attributable to Selected Major Risks*. Geneva: World Health Organization. http://www.who.int/healthinfo/global_burden_disease/global_health_risks/en/index.html, accessed 18 July 2012.
- World Bank. 2011. *Household Cookstoves, Environment, Health, and Climate Change: A New Look at an Old Problem*. Washington, D.C.: The World Bank. <http://climatechange.worldbank.org/sites/default/files/documents/Household%20Cookstoves-web.pdf>, accessed 18 July 2012.
- Wright, B. W. 1953. "Gravimetric Thermal Precipitator." *Science* 118 (3059). New Series: 195.
- Xiong, C., and S. K. Friedlander. 2001. "Morphological Properties of Atmospheric Aerosol Aggregates." *Proceedings of the National Academy of Sciences of the United States of America* 98 (21) (October 9): 11851–11856.
- Yuntenwi, Ernestine A.T., Nordica MacCarty, Dean Still, and Jürgen Ertel. 2008. "Laboratory Study of the Effects of Moisture Content on Heat Transfer and Combustion Efficiency of Three Biomass Cook Stoves." *Energy for Sustainable Development* 12 (2) (June): 66–77.
- Zhang, J., K R Smith, Y. Ma, S. Ye, F. Jiang, W. Qi, P. Liu, M A K Khalil, R A Rasmussen, and S A Thorneloe. 2000. "Greenhouse Gases and Other Airborne Pollutants from Household Stoves in China: a Database for Emission Factors." *Atmospheric Environment* 34 (26): 4537–4549.
- Zhang, Qunfang, Roja H. Gangupomu, David Ramirez, and Yifang Zhu. 2010. "Measurement of Ultrafine Particles and Other Air Pollutants Emitted by Cooking Activities." *International Journal of Environmental Research and Public Health* 7 (4) (April 16): 1744–1759.

Appendices

Appendix A: Exhaust system calibration and estimated dilution ratio

A.1 Exhaust system calibration

A.1.1 Overview

The exhaust system in Figure 25 was designed and assembled in the Proteus engine test cell at the UBC Clean Energy Research Centre (CERC) in 2011. Photos of the resulting system appear in Figure 26.

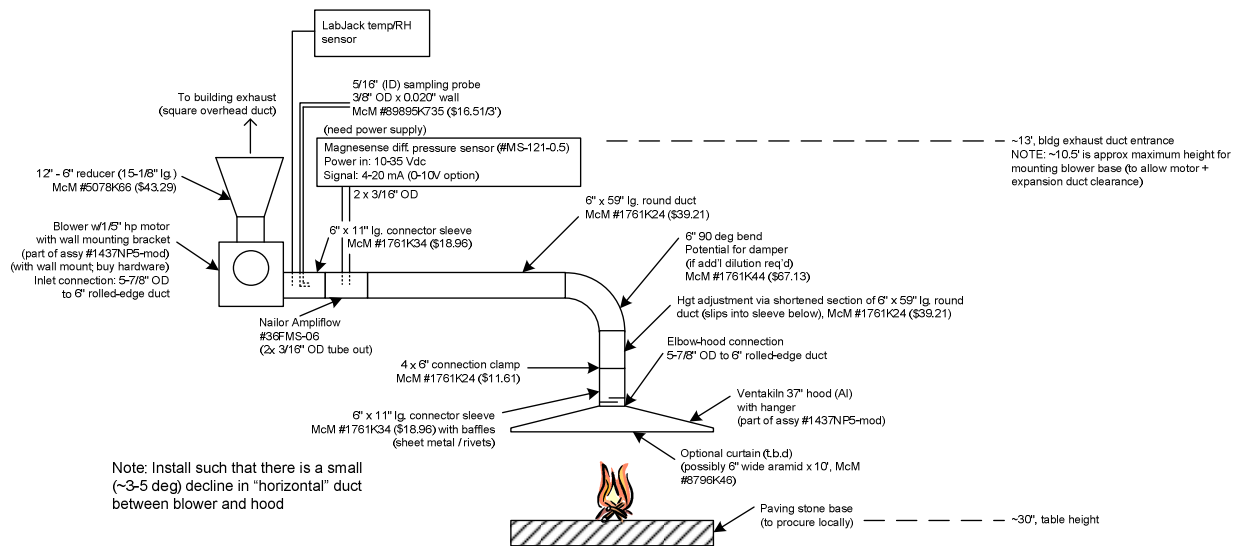


Figure 25. UBC cookstove test exhaust system

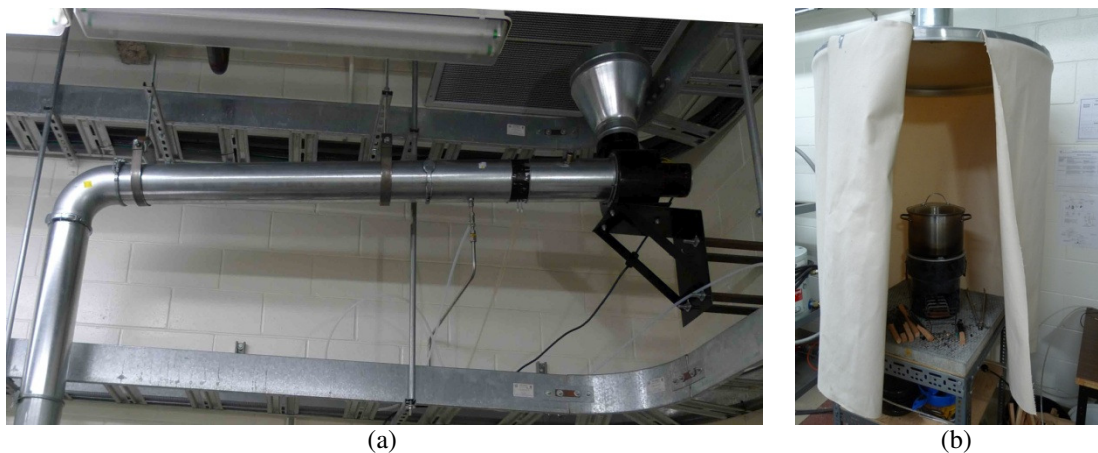


Figure 26. Photo of cookstove exhaust system, (a) upper assembly and (b) hood

Plume velocity was measured with a hot-wire anemometer as a function of distance below the duct inlet within the exhaust hood. Tests were done with the Chulika cookstove in place and its top surface 90 cm below the duct inlet. Data is summarized in Table 14.

Table 14. Plume velocity vs. distance below duct inlet in hood

Distance beneath duct opening, cm	Velocity, fpm	Velocity, m/s
10	525	2.67
20	165	0.84
30	75	0.38
40	67	0.34
50	62	0.32
60	52	0.26
70	28	0.14
75	10	0.05
80	4	0.02
85	3	0.02
90	2	0.01

For the experiments in this study, the top of the Chulika cookstove is 90 cm below the duct inlet. The same measurements for the Oorja cookstove and the three-stone bricks are 93cm and 108 cm, respectively.

The exhaust system flow rate was then calibrated on 22 Jan 2012.

A.1.2 Objective

Introduce CO₂ of known concentration into the exhaust hood. Measure resulting [CO₂] at emissions bench to determine lag time and to calibrate the flow rate (currently estimated via pressure drop across a flow multiplier).

A.1.3 Setup

Figure 27 details the testing setup used. The CO₂ supply was a 4.5% CO₂ / 95.5% N₂ mixture provided by Praxair (Order no. 14162773, Cust. Ref. No. XC862). Flow rate was measured with a Bios Defender 510-H volumetric flowmeter. The flow multiplier connected to the differential pressure sensor was a Nailor Ampliflow 36FMS-06, essentially a multi-probe Venturi effect meter. A provided calibration constant converted pressure drop to flow velocity (and thus flow rate when combined with cross-section geometry); it is this constant which is corrected here. The differential pressure sensor was a Dwyer MS-121-LCD. The CO₂ analyzer was the same used within the AVL emissions test bench (detailed elsewhere). The lab temperature during testing was 285 K.

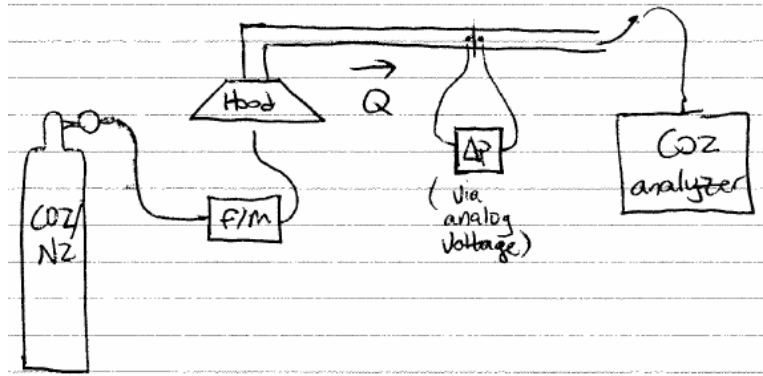


Figure 27. Sketch of exhaust flow rate calibration test setup

A.1.4 Method

The exhaust system was warmed up (> 30min) with a rotameter and BIOS flowmeter set to introduce ~30 lpm of the bottled mixture into the exhaust hood when the mixture tank valve was opened. Gas was cycled on/off twice at one minute intervals, then cycled on/off three times in two minutes-on / one minute-off intervals. During “on” events, mixture flow rate was measured constantly. Averaged readings at ~0.5 Hz were recorded. Throughout, the CO₂ analyzer recorded [CO₂], while analog voltage feedback from the differential pressure sensor was recorded by the StoveTester LabVIEW program. Both programs recorded data at 1 Hz.

A.1.5 Results

For each “gas on” event, it was necessary to evaluate feedback and determine the time it took for the CO₂ to reach the emissions bench. Typically, it took 10 seconds for a noticeable change in [CO₂] feedback. The value would ramp up and settle after an average of 23 seconds had elapsed.

Table 15 summarizes the measurements. The final column is a calculation of flow rate based on [CO₂] data. Shaded columns highlight the difference between the estimated and “true” flow rate. The calibration constant provided by Nailor overpredicts flow rate by ~20%.

Table 15. Summary of exhaust flow calibration data

Run #	Q_tot (scfm), calculated from Δp	[CO ₂] _{tot} (ppm)	Q_CO ₂ (lpm)	[CO ₂] _{back} (ppm)	Q_tot (scfm), from CO ₂ fdbk
1	260.2	635.1	30.0	415.0	214.7
2	260.5	640.8	29.9	416.3	209.8
3	260.5	635.5	30.1	411.9	212.1
4	260.4	632.5	30.2	410.1	213.7
5	260.5	631.2	30.2	410.5	215.7

A new calibration constant was determined (341.1 vs. the Nailor-provided value of 416.6). This is a multiplier that functions as follows:

$$Q = 341.1\sqrt{p}$$

where p has the units of inches of water and Q is in scfm. Recalculating flow rates for each run using the new constant, measurement error is 2% or less, using the voltage (thus, Δp) to calculate.

A.1.6 Comments

The lag time (cookstove to emissions bench) for detection is on the order of 10 seconds, with more than double that time required for the CO₂ analyzer to stabilize with a large step change. For steady-state combustion (which, for fires, is actually not very steady with regards to levels of CO₂ emissions), it will be assumed that there is a ~15 second lag.

A new calibration constant was determined which enables better knowledge of the actual exhaust flow rate based on analog feedback from the differential pressure sensor. The calibration is an average of five averaged measurements. It should be noted that it was done at only one flow rate (the exhaust fan is single-speed) and at one temperature (room temperature on the day of calibration, noted above).

During actual tests, temperature was recorded, with flow rate corrections applied as needed.

A.2 Dilution ratio

There is no clear definition of dilution ratio for the tests that comprise this research. It can be estimated by comparing total exhaust volume of oxygen to the volume of oxygen required for stoichiometric combustion (in this example, only CO₂ and CO are considered).

$$Dilution = \frac{[O_2]_{meas}}{\{[CO_2]_{meas} - [CO_2]_{back}\} + 0.5 \cdot [CO]_{meas}}$$

By this definition, dilution ratio during the cookstove tests was typically around 150:1.

Appendix B: Flow requirements and isokinetic probe sizing

The total flow requirement for the instruments (with quartz and PTFE filter collection and TPS pumps on) is approximately 25 lpm (see Table 16). Based on a circular duct size of 15 cm (6”) and an estimated total exhaust flow rate of 5380 lpm (~190 scfm), an isokinetic sampling probe should have an inner diameter of ~10.4 mm (0.41”). Considering the constantly operating devices only, velocity matching yields an inner diameter of ~7.3 mm (0.29”).

A thin-walled stainless steel tube with 8.5 mm (0.335”) inner diameter was chosen (optimal for ~17 lpm). The tube was bent with a gentle (6.35 cm / 2.5”) radius of curvature and situated to reside in the center of the duct with its opening facing into the exhaust flow.*

Table 16. Flow rate requirements

Device	Flow, lpm	Always on?
Filter 1	~6	No
Filter 2	~6	No
TPS	~1	No
DustTrak DRX 8533	3	Yes
Aethalometer AE 21	1	Yes
SMPS 3080	0.3	Yes
APS 3321	1	Yes
AVL bench (gases)	7	Yes
Total, always on	12.3	
Total, peak	~25	

* A thin-walled nozzle inlet may be loosely defined as a tube with the ratio of external to internal diameter of less than 1.1 (Brockman 2001). In this case, the exterior diameter is 0.375” and the interior diameter is 0.335”; the ratio between the two is 1.12.

Appendix C: Gaseous phase emissions instrumentation details

Routing for the primary gas line is via ~15 m of $\frac{3}{8}$ " (outer) diameter PTFE followed by ~10 m through a heated stainless steel line. Residence time was measured to be ~15 seconds. The secondary CO₂ line was $\frac{3}{8}$ " (outer) diameter PTFE, ~15 m long.

The instrumentation contained within the AVL emissions bench at CERC is summarized in Table 17.

Table 17. AVL Emissions Bench specifications (UBC SCRE Users Manual, Rev. E, (2009))

Exhaust Component	Make	Model	Operating Principle	Range
Total Hydrocarbons (tHC)	Pierburg	FID 4000 hhd	FID	0 – 1500 ppm
Carbon Monoxide (CO)	ABB	Uras 14 EGA	FID	0 – 2300 ppm
Nitric Oxide (NO)	Pierburg	CLD 4000 hhd	Chemi-luminescent	0 – 2600 ppm
Oxides of Nitrogen (NOX)	Pierburg	CLD 4000 hhd	Chemi-luminescent	0 – 2600 ppm
Methane (CH ₄)	Pierburg	FID 4000 hhd	FID	0 – 3900 ppm
Oxygen (O ₂)	ABB	Magnos 106 EGA	Para-magnetic	0 – 22% vol
Carbon Dioxide (high) (CO ₂)	ABB	Uras 14 EGA	NDIR	0 – 15% vol
Carbon Dioxide (low) (INT CO ₂)	ABB	Uras 14 EGA	NDIR	0 – 5.0% vol

General Specifications:

Repeatability	< 1% FS
Noise (Peak-Peak)	< 2% FS
Drift	< 2% FS/8h
Linearity	< 2% of point between 15% and 100% of measuring range
	< 1% FS

Appendix D: Estimate of PM diffusion losses

Aerosols adhere to tube walls. Aerosol concentration at surfaces is zero, so there exists a concentration gradient, with subsequent diffusion (losses) of particles to the walls. Hinds (1999) provides an equation for the penetration (fraction of entering particles that exit) for fully developed laminar flow through a tube with circular cross section,

$$P = 1 - 5.50\mu^{2/3} + 3.77\mu \quad \text{for } \mu < 0.009$$

with dimensionless deposition parameter

$$\mu = \frac{DL}{Q}$$

where D is the diffusion coefficient of the particles (a function of mean velocity and mean free path), L is the tube length, and Q is the volume flow rate through the tube. Hinds notes that losses do not depend on tube diameter for a given flow rate since the extra distance that particles must diffuse in a larger tube is offset by the longer time for diffusion permitted by that larger distance.

In the cookstove emissions testing setup, after ~50 cm of open section from the stove top to the exhaust collection inlet, exhaust is routed through a 6" diameter galvanized steel duct (of ~250 cm length). A 1/2" line (length ~270 cm) following an isokinetic sampling port carries it to various instruments. Further downstream, it tees to 3/8" lines (~20 cm), and then 1/4" lines (50-150 cm) draw air through various PM instruments with flows corresponding to Table 16 in Appendix B. Table 18 lists dimensions and rough flow rates used in this analysis.

Table 18. Flows and dimensions for diffusion losses

Section	Flow rate	Length (cm)
1 (6" dia)	0.09 m ³ /s (190 scfm)	~250
2 (1/2" dia)	~5 lpm	~270
3 (3/8" dia)	~5 lpm	~20
4 (1/4" dia)	~1 lpm	~100

Deposition / penetration is a function of particle size, so it is necessary to complete the calculation over a range of particle diameters. For each, total penetration is obtained from the product of the penetrations for the different sections (this is not necessarily valid, but can approximate the total). Figure 28 shows penetration using data from Table 18 over a size range of 10 nm to 1 um.

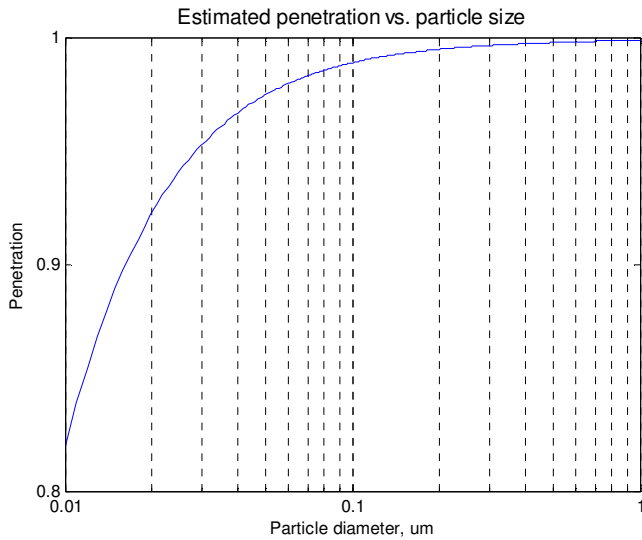


Figure 28. Penetration vs. particle diameter for cookstoves emissions test setup

There are significant losses of nanoparticles; the penetration of 100 nm particles is still high at ~0.99 but falls to ~0.82 for 10 nm particles. In order to minimize losses, it is necessary to understand where they come from. For the 10 nm size, “Section 1” has 0.999 penetration due to the high duct flow rate. The sampling line (Section 2) has 0.954 penetration and the short section of low-flow through the TPS has only 0.876 penetration.

All particulate monitoring instruments used in the tests are subject to the losses of sections 1-3, plus a short low-flow section just upstream of the measurement region. Omitting Section 4 (the ¼” line), penetration of 100 nm particles is greater than 0.99 and it is ~0.92 for 10 nm particles. Increasing the flow rate through Sections 2 and 3 (and “dumping” excess exhaust) is a viable way to reduce diffusion losses, but more losses come from the low flow ¼” line. The main lesson here is to minimize the distance traveled within this final section.

Appendix E: PM emissions instrumentation details

DustTrak DRX 8533 (TSI Incorporated 2012)

Measurement range	0.1 – 15 μm , .001 -150 mg/m^3
Resolution	$\pm 0.1\%$ of reading or .001 mg/m^3 , whichever is greater
Zero stability	$\pm 0.002 \text{ mg}/\text{m}^3$ per 24 hrs at 10 sec time constant
Operational humidity	0-95%
Flow accuracy	$\pm 5\%$ of factory set point, internal flow controlled
Operational temp	0-50C

The instrument is calibrated to ISO 12103-1, A1 test dust (formerly Arizona Test Dust).

Magee Scientific AE 21 (aethalometer)

The instrument measures “black” or “elemental” carbon aerosol particles by measuring light transmission through a quartz fibre filter tape. Sensitivity depends on the rate of aerosol collection and the minimum detectable increment of BC on the filter. Accuracy is relative and can be estimated by comparing aethalometer data against measurements obtained by other BC instruments.

The Magee Scientific operational definition of aerosol black carbon provides some insight into the measurand:

‘Black Carbon’ is that fraction of aerosol particulate matter that is insoluble in polar and non-polar solvents; is stable in a pure oxygen atmosphere to a temperature of 350°C; which displays the Raman spectral lines characteristic of both the graphitic structure and the features of microcrystallinity; and which is strongly optically absorbing in the visible spectrum. The actual quantitation of the material is performed by a chemical analysis of the CO_2 produced by combustion of a sample after extraction and thermal pre-treatment. The analysis yields a mass of carbon expressed in micrograms, and provides the basis for the calibration of the optical absorption measurement of sample ‘blackness’ in terms of a mass of ‘BC.’ (Hansen 2005)

Appendix F: TPS design and notes

A thermophoretic particle sampler (TPS) was developed by the author. This Appendix contains relevant background information on thermophoresis followed by design notes from other TPS designs. The final sections contain a short User's Manual and assembly drawings.

F.1 Introduction

Interest in aerosol monitoring extends to emissions research, occupational health, and the maintenance of industrial environments. Numerous instruments, both real-time and non real-time, are utilized in the study of aerosols; many focus on quantifying the size and concentration of particles.

Knowledge of the chemical composition and morphology of particles is necessary to gain a better understanding of their mechanisms and effects. One method is the off-line study of aerosol samples that have been collected onto grids or filters. Transmission electron microscope (TEM) support grids* are a medium that allows for subsequent analysis using various microscopic techniques including imagery and energy-dispersive x-ray spectroscopy. UFPs are the subject of much research but many collection processes used in the past (e.g., via diffusion and electrostatic precipitation) are not capable of sampling such small particles satisfactorily. Thermophoresis describes the movement, or “pushing,” of particles from high temperature to low temperature regions due to the higher mean velocities of gas molecules on the warmer side. This effect can also be utilized as a particle collection mechanism.

F.2 Thermophoresis

In the literature (e.g., Messerer et al. 2003; Lin & Tsai 2003), it is common to encounter an equation for thermophoretic velocity of the form

$$v_{th} = -K_{th} \frac{\mu_g \nabla T}{\rho_g T_p}$$

where μ_g and ρ_g are gas properties, T_p is the particle temperature, and ∇T is the temperature gradient near the particle; K_{th} , the “thermophoretic coefficient,” is subsequently defined in terms of gas / particle properties and is also dependent on a number of coefficients. Though references vary and the equation appears in various guises, a usual root source seems to be the article, *Thermophoresis in a heated boundary layer* (Talbot et al. 1980), in which the authors define thermophoretic velocity as

* Grids have a diameter of 3.05 mm and are coated with an electron-transparent film that varies in thickness from under 10 nm (e.g., carbon) to 50 nm (e.g., Formvar®), with various intermediate thicknesses and materials available.

$$U_T = - \frac{2C_s \nu \left(\frac{k_g}{k_p} + C_t \frac{\lambda}{R} \right) \left[1 + \frac{\lambda}{R} \left(A + B e^{-\frac{CR}{\lambda}} \right) \right] \frac{(\nabla T)_x}{T_0}}{\left(1 + 3C_m \frac{\lambda}{R} \right) \left(1 + 2 \frac{k_g}{k_p} + 2C_t \frac{\lambda}{R} \right)} \quad (F1)$$

The minus sign indicates motion in the direction of decreasing temperature gradient. For a clearer understanding of the equation, a brief overview of variables is warranted:

ν	kinematic viscosity of the gas ($=\mu/\rho$)
T_0	mean gas temperature in the vicinity of the particle
k_g	thermal conductivity of the gas
k_p	thermal conductivity of the particle
∇T	temperature gradient in the gas
R	particle radius

C_t is the “temperature-jump” coefficient and accounts for the temperature difference between the gas field and the surface of the studied (spherical) particle, with a heat flux boundary condition at the surface. It is on the order of unity and is determined from kinetic theory. C_m and C_s are the “momentum exchange” and “thermal slip” coefficients, respectively. Together, they couple the temperature distributions in the gas and particle with the velocity field; they come from the tangential velocity boundary condition of the particle. Like C_t , both C_m and C_s are on the order of unity and are determined by kinetic theory (Talbot et al. 1980).

Part of the numerator of equation (F1),

$$\left[1 + \frac{\lambda}{R} \left(A + B e^{-\frac{CR}{\lambda}} \right) \right]$$

is also referred to as the Cunningham coefficient, C_c . It corrects for the fact that a nonslip condition is not applicable as a boundary condition for high Kn ($=\lambda/R$) values (that is, for very small particles) in which drag force exerted by the fluid is smaller than that predicted by Stokes’ law (Seinfeld, John H. and Pandis, Spyros N. 2006). Its coefficients A, B, and C are determined by experiment.

λ is the mean free path of the suspending fluid and may be given by

$$\lambda = \frac{2\mu}{\rho\bar{c}}$$

where

$$\bar{c} = \left(\frac{8(\bar{R}/M)T}{\pi} \right)^{0.5}$$

\bar{R} is the ideal gas constant and M is the aerosol molar mass. By various substitutions, equation (F1) is reduced to a simplified

$$U_T = -K_{th} \frac{\nu(\nabla T)_x}{T_0} \quad (F2)$$

where

$$K_{th} = \frac{2C_s C_c \left(\frac{k_g}{k_p} + C_i Kn \right)}{(1 + 3C_m Kn) \left(1 + 2\frac{k_g}{k_p} + 2C_i Kn \right)} \quad (F3)$$

Coefficients are commonly assumed as in Talbot:

C_t	2.18
C_m	1.14
C_s	1.17
C_c	A = 1.20, B = 0.41, C = 0.88

Tsai and Lu (1995) designed a thermal precipitator which employed two temperature-controlled flat plates to create a high, uniform temperature gradient. They generated dry, neutralized, monodisperse aerosol particles and studied collection efficiency with a temperature gradient of up to nearly 900 °C/cm. Gravitational losses (small) and Brownian diffusion losses (important at small particle diameters, $\sim < 0.1 \mu\text{m}$) were accounted for. Experimental results were compared to various theories; it was found that the formula of Talbot et al. was the most accurate.

From equation (F2), it is clear that thermophoretic velocity increases with temperature gradient, a characteristic that can be controlled by a precipitation mechanism. Examination of the thermophoretic equation (F3) is necessary to fully understand how particle size (via variable Kn) and composition (via thermal conductivity, k_p). Table 19

displays the thermophoretic coefficient as a function of D_p ; the example was calculated assuming an aerosol temperature of 350K and a gas / particle conductivity ratio of 10. Because K_{th} (which can be considered as the dimensionless thermophoretic velocity) does not change by a large margin with particle size, from equation (F2) temperature gradient is seen to be the dominant design factor in a thermophoretic precipitation device.

Table 19. Particle size dependence of several dimensionless parameters relating to thermophoretic velocity

$D_p, \mu\text{m}$	C_c	Kn	K_{th}
100	1.00	0.002	0.64
0.1	3.55	1.65	0.59
0.001	274	164	0.57

To further analyze the effect of particle diameter on thermophoretic velocity, the two variables were plotted against each other in Figure 29 over a particle size range of 1 nm – 100 μm . It is clear that thermophoretic velocity changes very little above a Knudsen number of ≈ 1 . Air at a temperature of 350 K has a mean free path of ≈ 67 nm; particles smaller than this size are expected to have the same thermophoretic velocity (provided their thermal conductivities are similar). The literature agrees with this statement; the thermophoretic coefficient is commonly assumed to be a constant for $Kn \gg 1$.*

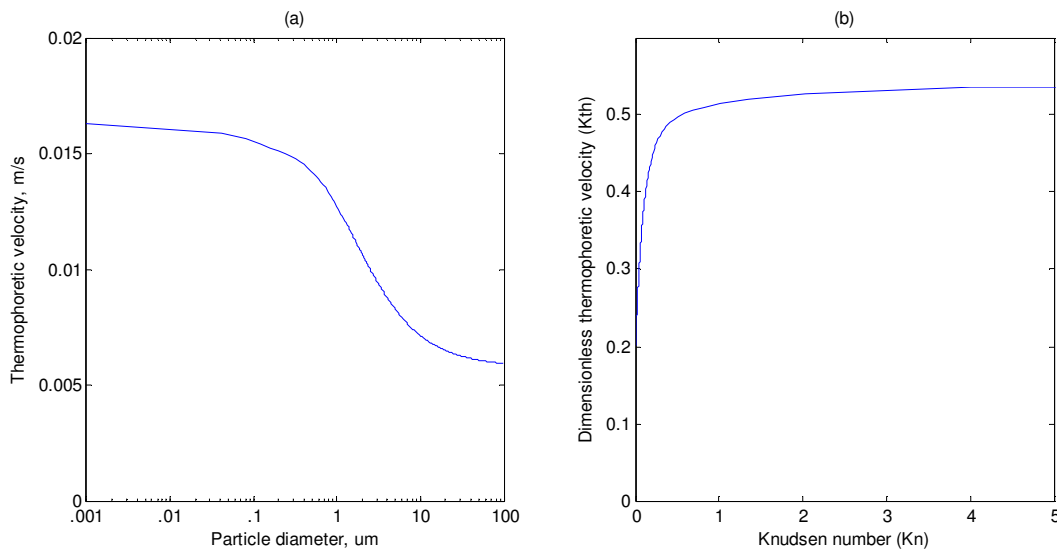


Figure 29. (a) dimensionless and (b) characteristic example of thermophoretic velocity vs. particle size ($k_g/k_p=10$, $\nabla T = 5 \times 10^5 \text{ K/m}$ and $T=350\text{K}$)

* E.g., $K_{th} = 0.55$ for both $Kn \gg 1$ and $Kn \approx 1$ in Messerer et al. (2003).

F.3 Existing thermophoretic samplers

Early predecessors to the TPS were called thermal precipitators. Green and Watson (1935) are credited with the first; it was a heated-wire-and-plate design in which air containing dust flowed past a heated wire suspended between two plates (of glass coverslips over brass). Dust deposited on the (cool) plates; the device was used to measure size distributions and concentrations of coal dust in British mines. Various permutations of their heated-wire-and-plate design have been used. Early plate-to-plate designs were capable of higher aerosol flow rates and better deposition uniformity. Wright (1953) passed air between a resistively-heated plate and an aluminum collecting plate in order to collect dust samples for inhalation experiments. He noted that performance was governed by power input independent of wide limits of temperature and air gap, and that plate parallelism and uniform air flow distribution were important factors. Another early design directed air between a resistively-heated top plate and a water-cooled bottom plate to precipitate airborne particles and bacteria onto a 3" diameter cover slip (Kethley, Gordon, and Orr 1952). In contrast to the heated-wire-to-plate and plate-to-plate techniques, Hendrix and Orr (1964) created a design that employed a heated aerosol stream to deposit particulate onto a cooled rotating disk.

In later years, the thermophoretic effect began to be utilized in the deposition of particles onto microscopy grids. Kasper (1982) improved on the original Green and Watson heated-wire-and-plate TPS design by arranging a well-defined aerosol flow to the TPS inlet; more recently, Bang et al. (2003) constructed a TPS that used a heated tungsten wire and a water-cooled grid support base. The plate-to-plate style TPS has been the dominant thermophoretic collection tool in the past ~15 years; a sample device schematic is depicted in Figure 30. The hot plate is actively heated; the cool plate may be actively or passively cooled. Aerosol sample is directed between the parallel plates, with subsequent deposition on the cool plate. Collection efficiency is theoretically proportional to thermophoretic velocity and length L , and inversely proportional to aerosol flow rate and gap h . However, there are losses to diffusion along the upstream flow channel and thermophoretic deposition on surfaces other than the desired location (collection grid).

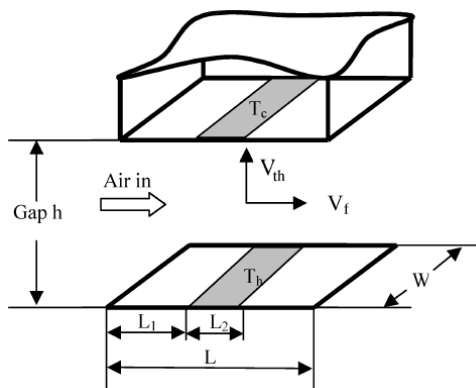


Figure 30. Plate-to-plate thermophoretic sampler (Wen and Wexler 2007), used with permission from Taylor and Francis.

Maynard (1995) constructed a plate-to-plate design with ΔT of 100°C and a plate separation of 0.1 mm, resulting in a temperature gradient of 10^6 $^{\circ}\text{C}/\text{m}$. In order to reduce the flow resistance with the narrow gap and a low-power portable air pump, the flow channel was quite wide (80mm). The grid was mounted on a removable holding stage constructed of phosphor bronze; a thermocouple was attached near the grid to allow temperature monitoring. A magnetic clamping system was employed to allow the grid to set flush with the plate surface, though a disadvantage of the technique was that it necessitated the use of ferrous grids. A 2 mm diameter heating element was mounted (within a ceramic mount) opposite the microscopy grid; it was not possible to attach a thermocouple directly to the element. 6V batteries supplied power of 5 V and ~ 1 A to the heating element. The device was capable of sampling particles to less than 5 nm, but deposition was not uniform, with regions of preferential deposition and deposition-free zones. The grid lattice, imperfect grid / substrate evenness (resulting in flow variations), less than optimal grid / substrate thermal contact, and temperature gradient variations were theorized as reasons for non-uniformity. Another shortcoming was the fact that the collection grid reached 30°C above ambient, which implies potential for heat damage of the grid.

Wen and Wexler (2007) improved upon Maynard's plate-to-plate design in several ways. Noting the trade-off between choosing a low aerosol flow rate to maximize thermophoretic deposition and the advantage of a high flow rate to minimize diffusion in the upstream region, they added a bypass channel just before the temperature gradient region, permitting a high flow rate in the upstream region and a low flow rate across the collection grid. Lorenzo et al. (2007) created a TPS with characteristics that overlap both of the designs. A 4 mm diameter heating element is mounted opposite a TEM grid which is held in place by a magnet; the heating element and TEM grid temperatures are monitored by thermocouples. Flow through the sampling channel is halted while the temperature gradient is established; an adjustable flow bypass is used to keep diffusion losses to a minimum. They calculate a thermophoretic migration velocity of 1 cm/s, noting that only particles from a limited height will be collected. Deposition is not uniform, though it is seen to be roughly constant ($\pm 10\%$) in the central section of the grid. Particle flux is highest near the center of the sampling channel. Large temperature gradients have variations that exceed 3%, potentially limiting the usefulness of high gradients for greater thermophoretic velocity. During experiments using Ag aerosols, TEM image analysis was compared with SMPS feedback and the size modes agreed to within 2%. The authors concluded that the TPS enables the quantification of particles in the 15-300 nm size range.

Two more recent TPS designs focused on portability and low flow to enable field sampling; both employ plate-to-plate design. Azong-Wara et al. (2009) developed a TPS for the study of occupational particle exposure. The optimized device has a temperature gradient of 1.5×10^4 K/m over a gap distance of 1 mm. Flow velocity is low (5.5 mm/s) with a very low flow rate (2 mL/min). They determined that a 6.5-mm section of the deposition region (of length 20mm) had adequate deposition uniformity for SEM tests. Thayer et al. (2011) built a device weighing 222 g (without battery, controller, and personal sampling pump) that consumes 7.2 W. It uses a hot plate (heated to 122°C with a Nichrome wire heater) and a cold plate (cooled to 12.2°C via a thermoelectric cooler) with a temperature gradient is 1×10^5 K/m. Their TPS is effective at capturing particles from 15 to 240 nm in diameter.

An interesting note is that collection efficiency is higher for 100 nm particles than for 15 and 51 nm particles, a result that contrasts with theory. As other authors have noted, particle collection decreased with increased flow. Results of deposition uniformity tests are displayed in the contour plots of Figure 31.

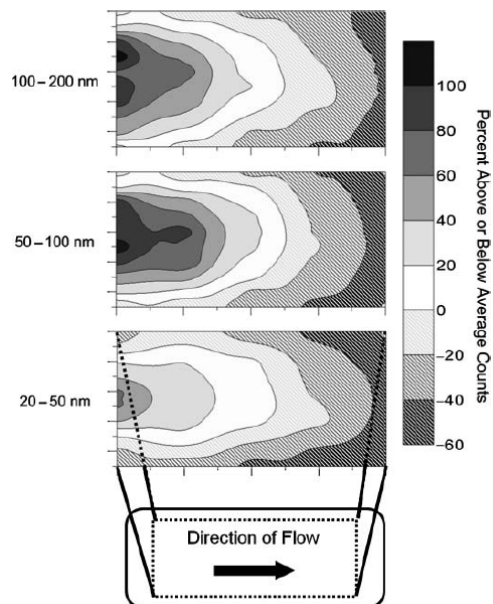


Figure 31. Deposition across the TPS of Thayer et al. (2011), used with permission from Taylor and Francis.

F.4 Other techniques

A review of lessons learned from existing aerosol sampling systems is not complete without a brief overview of other techniques; diffusion and electrostatic precipitation are other viable mechanisms for sampling aerosol particulates via TEM grids. In theory, diffusion is capable of being the mechanism for effective deposition of particles with small diameters but it is not effective for large diameters, nor is it easy to “focus” deposition into a specified area (such as a TEM grid).

Electrostatic precipitation passes an aerosol through an electric field after which they gravitate towards and collect onto a grounded substrate / TEM grid. Numerous designs have been used in the past and are well documented in the literature (see e.g., (Dixkens and Fissan 1999)). A recent design that focused on the creation of a portable electrostatic precipitator (ESP) is presented here; it is demonstrative for an overview of the process and will be useful in comparing the relative benefits of electrostatic precipitation vs. thermophoresis for aerosol sampling.

Miller et al. (2010) designed an ESP using a point-to-plane configuration as depicted in Figure 32. Aerosol particles are charged by ions produced by corona discharge at the anode. The charging mechanisms include diffusion charging (due to random collisions) and field charging (particles intersection with ion field lines). Diffusion charging efficiency is higher for small particles; field charging is higher for large particles.

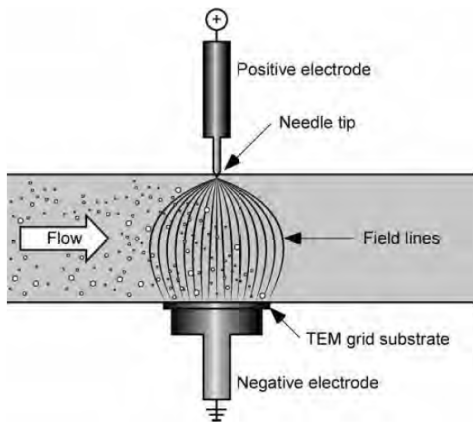


Figure 32. Configuration of ESP by Miller et al. (2010), used with permission from Taylor and Francis.

There are a few key equipment limitations to the ESP. High voltage is required (the range used was 5.6 – 6.8 kV) and charging current is limited by a desire to prevent arcing. Performance-wise, deposition uniformity on the TEM grid seemed acceptable. However, particles below 30 nm were difficult to charge and collect. Collection efficiency is relatively high though size-biased;

Figure 33 demonstrates the lower charging efficiency in the transition region between the diffusion- and field-dominated charging regimes. There may be restrictions on the testing and measurement of certain materials due to adverse reactions with an electric field or their resistance to charging. Thus, collection is dependent on both particle composition and size.

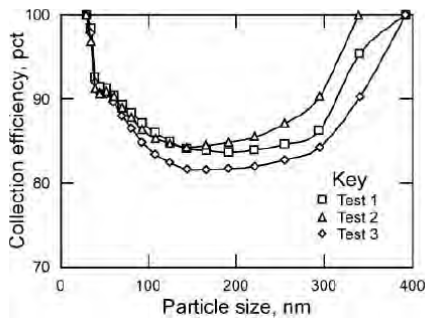


Figure 33. Sample collection efficiency for an ESP (Miller et al. 2010), used with permission from Taylor and Francis.

Some of the relative advantages and disadvantages of thermophoretic and electrostatic precipitation are presented in Table 20.

Table 20. Comparison of precipitation mechanisms

Thermophoretic precipitation	Electrostatic precipitation
Collection efficiency relatively independent of particle diameter under a certain range (~100 nm)	Nanoparticles smaller than 30 nm are difficult to charge and collect; lower efficiency in the 200 nm region
A wide range of aerosol particles can be collected	Aerosol particles must be able to hold a charge
High temperatures increase collection efficiency, but can be difficult to maintain accurately	High current increases charging efficiency, but is limited by arcing
High temperatures may vaporize or change chemical composition of particles	Charging may alter volatile particles
Low temperatures on the “cool” side can result in condensation of water onto the grid	Requires grounded, electrically conductive substrate and high voltage power source
Inevitable temperature gradients that extend beyond grid increase particle losses	Inevitable losses due to charge particles depositing outside the collection region
Power requirement is relatively modest and is limited to heating (and optional cooling)	High voltage requirement makes implementation more complex, especially with creation of a portable device

Both precipitation mechanisms share some features. High aerosol flow rate tends to minimize diffusion losses while decreasing sampling efficiency; a bypass flow just prior to the deposition region can minimize unwanted effects. Small size and weight is advantageous for portability that permits usage in a wider array of environments.

While the TPS has several advantages over the ESP, there are a few drawbacks to current designs. Based on the preceding comparisons, an “optimal” design would include:

- a smooth, flush collection area (if using a plate design) that does not alter the aerosol flow
- low power consumption
- a cool substrate / TEM grid without the need for active cooling
- a small, lightweight design
- minimal diffusion losses, possibly aided by high aerosol flow with a bypass just prior to the heated region
- interchangeable sampling heads that allow preparation of TEM grids in advance
- good thermal contact between the collection grid and the substrate
- a well-insulated heating element
- a repeatable temperature gradient
- adjustable aerosol flow rate for performance monitoring
- temperature feedback of the aerosol and grid to aid performance monitoring
- a design that enables uniform deposition, with no preferential or deposition-free zones

F.5 University of British Columbia TPS (previous)

A TPS was previously constructed at UBC by B.S. Brown and S. Rogak. Contrary to the plate-to-plate designs commonly encountered for aerosol particle precipitation onto TEM grids, the design used a heated aerosol stream through a tube that impinges onto a cool substrate / TEM grid as shown in Figure 34.

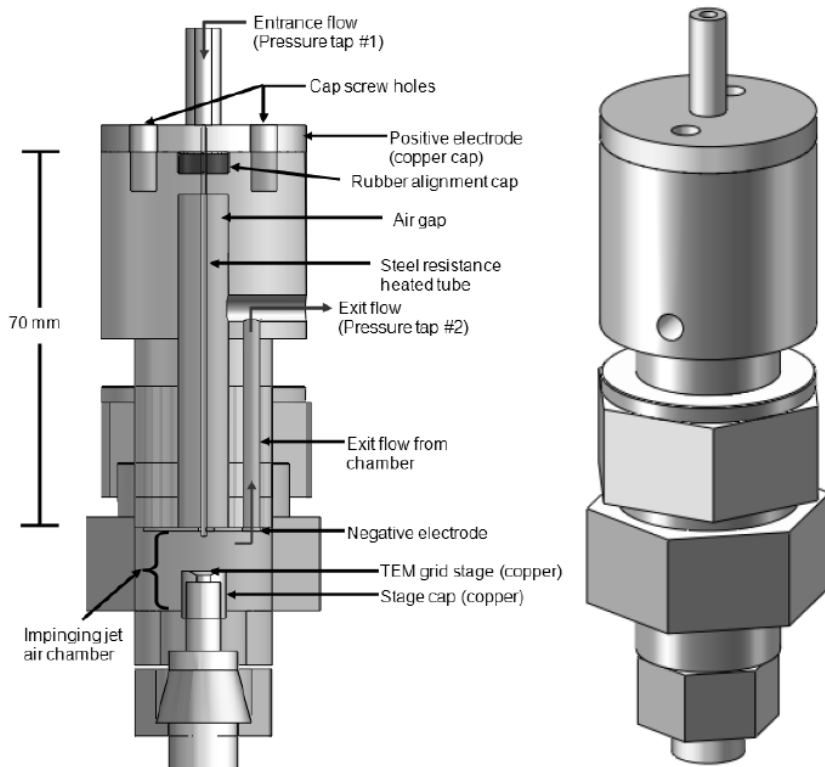


Figure 34. Previous version of UBC TPS (Images: (Lagally 2011)).

This “impinging jet” design is novel for a several reasons, including:

- The jet flow is perpendicular to the grid surface, so deposition should be axisymmetric.
- Particle deposition will be highest near the stagnation point (where particle radial velocities are lowest); if properly aligned, this high deposition region will occur at the center of the TEM grid.
- The heated mass (a thin hypodermic needle) is relatively small, theoretically enabling the use of a small power supply.
- A compact arrangement allows for a small, lightweight design.

Users and observers of the current TPS noted a few areas of potential improvement:

- It is difficult to accurately set / determine the jet-to-grid distance; in addition, the distance is influenced by the tightness of screw-on connections.
- Electrical contact to the heated tube can be intermittent.

- The TEM grid is held in place by gravity via a slip-fit connection; this makes the device unidirectional and there is the potential for poor thermal contact between the grid and the cool thermal mass.
- Occasional soot build-up inside the heated tube requires cleaning and is a potential source for contamination.
- Occasional water condensation on the TEM grid during sampling poses a problem.
- Threaded connections to the TPS base are easily stripped.
- The large power supply and pump used make the overall setup quite bulky.

F.6 New TPS design

The new TPS has interchangeable heating tubes comprised of standard (4") Luer lock hypodermic needles coated with a thermally conductive, electrically insulating material; heating is via current running through a spiral wrapping of Nichrome wire. Further design improvements include a low-pitch screw in base with a slip-fit magnetic cap that holds a TEM grid in place. The overall assembly is pictured in Figure 35(a) with the modular heating portion shown in Figure 35(b).

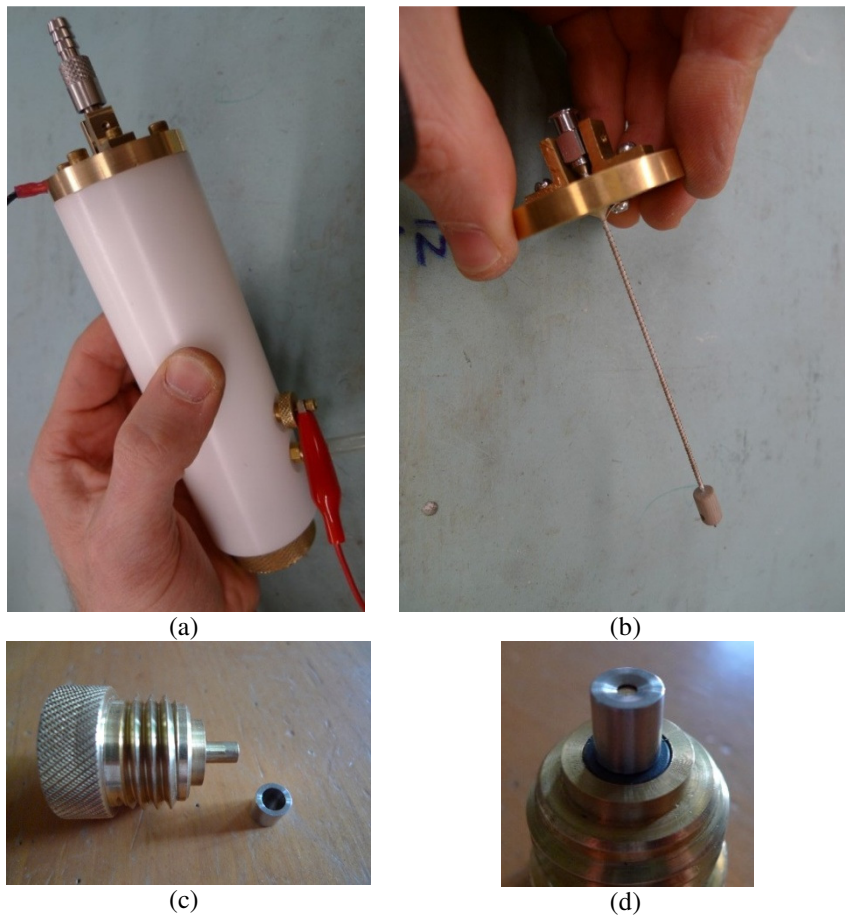


Figure 35. New TPS (a) overall body, (b) heated tube, (c) removable base and magnetic cap, (d) close-up view of magnetic cap and TEM grid location

F.7 Design notes

The final design was based on measurements of exhaust flow rate and temperature across several needle diameters and power input levels. Additionally, the following equation from Hinds (1999) (p126) was used to estimate d_{50} (cutoff diameter), the size at which the masses of the particles larger and smaller than d_{50} that pass through the system are equal.

$$d_{50}\sqrt{C_c} = \left[\frac{9\pi D_j^3 (Stk_{50})}{4\rho_p Q} \right]^{1/2}$$

In the equation, C_c is the Cunningham coefficient, D_j is the jet diameter, and Stk_{50} is the Stokes number for 50% collection efficiency (given by Hinds as 0.24 for a circular jet). Q is the flow rate and ρ_p is particle density (assumed 1000 kg/m^3). For each of three needle sizes, input voltage,* and flow rate were varied. Peak exit temperature was recorded while exit velocity, d_{50} , and Reynolds number (Re) were calculated. Data appears in Table 21.

Table 21. TPS parametric analysis results

Heated tube gauge	Input voltage	T, K	Δp , psi	Q, lpm	U, m/s	d_{50} , μm	Re
16	5	311.8	0.5	2.69	33.4	0.353	2646
	5	305.5	1.0	3.92	47.8	0.276	3924
	5	304.9	1.5	4.81	58.5	0.241	4824
	5	303	2.0	5.66	68.5	0.216	5708
18	5	328.5	0.5	1.27	32.4	0.310	1673
	5	318.8	1.0	1.98	49.1	0.229	2674
	5	311.8	1.5	2.74	66.6	0.180	3770
	5	309.6	2.0	3.30	79.7	0.157	4568
20	5	355.8	1.5	1.18	72.3	0.150	2176
	5	352.7	2.0	1.70	103.2	0.112	3156
16	7	329	0.5	2.69	35.1	0.363	2530
	7	321.8	1.0	3.78	48.4	0.291	3620
	7	316.8	1.5	4.72	59.5	0.250	4580
	7	313.8	2.0	5.57	69.6	0.223	5449
18	7	342.2	0.5	1.89	50.2	0.245	2411
	7	367.3	1.0	1.09	31.1	0.359	1319
	7	330	1.5	2.60	66.7	0.193	3413
	7	326.5	2.0	3.26	82.7	0.163	4316
20	7	407.1	1.5	1.13	79.5	0.167	1893

* Resistance of the heating element for the 16 gauge needle tested was 11.5Ω . 18 gauge: 12.7Ω . 20 gauge: 11.4Ω .

Heated tube gauge	Input voltage	T, K	Δp , psi	Q, lpm	U, m/s	d_{50} , μm	Re
16	10	375.2	0.5	2.36	35.2	0.417	2010
	10	349.3	1.0	3.59	49.7	0.313	3222
	10	342.3	1.5	4.62	62.7	0.264	4212
	10	337	2.0	5.43	76.2	0.241	4826
18	10	426	0.5	0.94	31.3	0.417	1024
	10	396.8	1.0	1.75	54.1	0.276	2004
	10	375	1.5	2.36	68.8	0.221	2813
	10	362.3	2.0	2.83	79.6	0.192	3458
20	10	500	1.5	0.94	80.6	0.212	1344
	10	493.1	2.0	1.46	123.8	0.154	2114

The 18 gauge needle had a wider achievable temperature range than the (larger) 16 gauge needle and lacked the high pressure drop associated with the 20 gauge needle. With 10 V applied across the heating element, it heated aerosol to about 100 K above ambient (which was 294 K in the laboratory on the day of testing). Cutoff diameter was calculated at ~0.28 μm for the needle / power / flow rate in bold in Table 21. It is important to note that this is *aerodynamic* diameter, the size of a water droplet with the same drag / mass ratio as a particle in question.

The TPS Instructions manual on the following pages details the instrument's operation and maintenance. Full drawings are available electronically.

TPS Instructions
Version 1.2, 18 April 2012
Brian Just

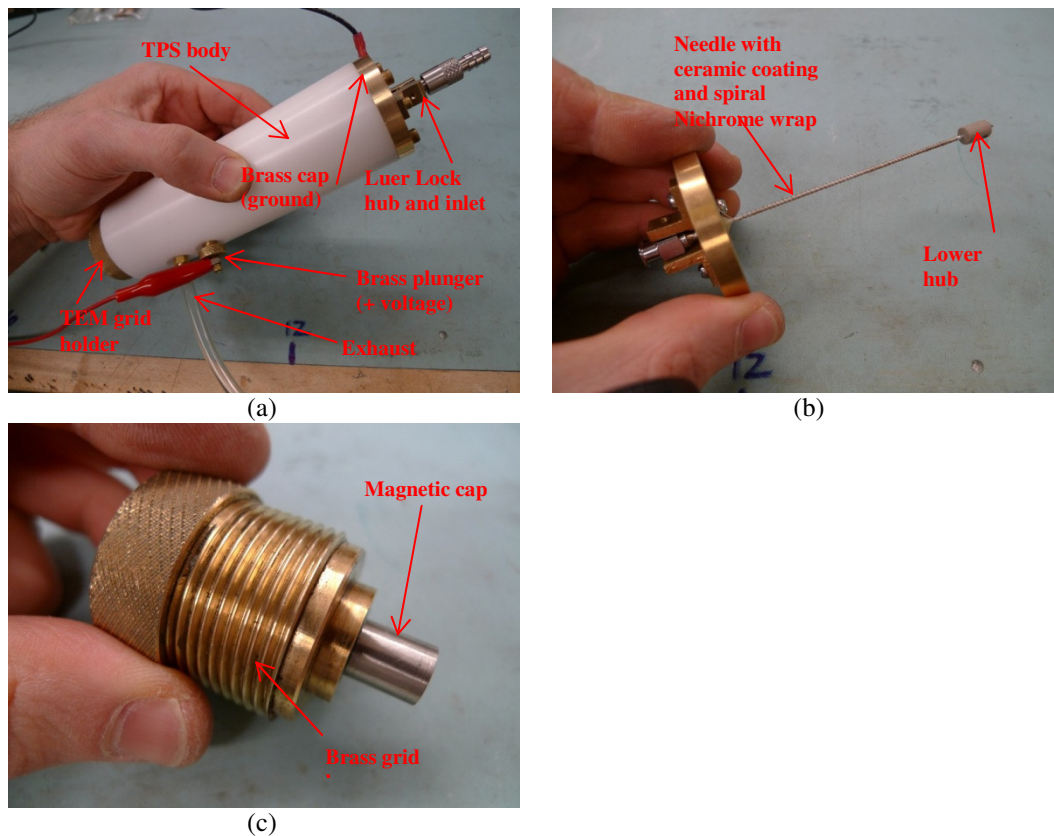
Update history

v1.0	Created document. Notes on sampling time taken from previous document by C. Lagally.
v1.1	Added notes on TEM grid fragility.
v1.2	Minor updates/notes.

Overview

The thermophoretic particle sampler (TPS) uses the thermophoresis to deposit particulate matter onto a 3.05mm diameter transmission electron microscopy (TEM) grid. The aerosol stream is heated via power applied to a 32 gauge Nichrome wire wrapped around a ceramic-coated hypodermic needle. For ease of connection, the needle has a Luer Lock connection on the upstream side. Power is applied via the provided power supply and voltage regulator (pre-set to the appropriate voltage); the TPS brass cap serves as ground while an alligator clip provides positive voltage to a brass screw terminal on the side of the unit. Sensitive and heated parts are contained within a robust, insulating Delrin body. See Figure 1 for a visual overview.

Figure 1. TPS overview: (a) TPS body with electrical connections, (b) internal needle assembly, (c) TEM grid holder



Accessories

The following accessories are included with the TPS (see Figure 2):

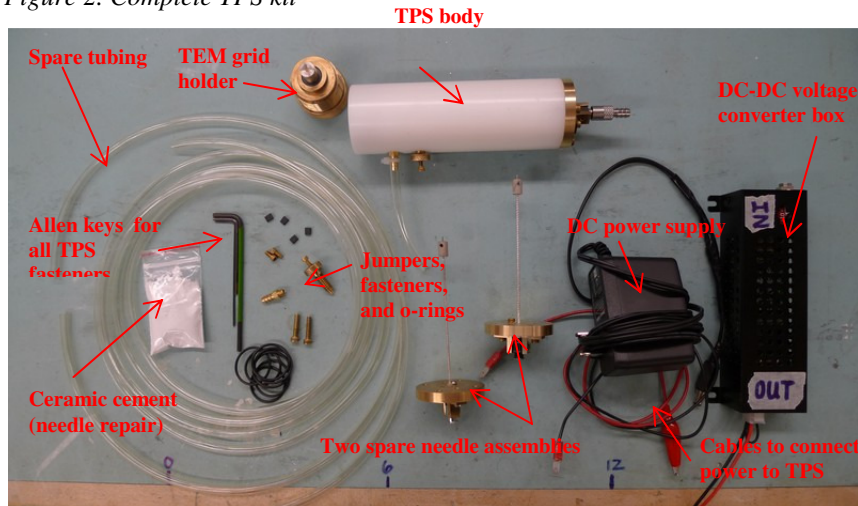
- Allen key x 3 (for Imperial fasteners and setscrews)
- O-rings (upper and lower seals)
- Power supply (100-240 VAC to 12VDC)

- Voltage regulator jumpers
- Spare fasteners

Items *not provided*:

- TEM grids (Ted Pella P/N 01813-F, Carbon Type B, 300 Mesh Cu)
- Europe to North America plug adapter

Figure 2. Complete TPS kit



Refer to assembly drawings (Figure 9 and Figure 10) for replacement part numbers and further detail.

General usage

The assembled TPS is relatively straightforward to operate. Steps are divided into subsections.

Preparation

These steps should be repeated at least once per testing day. They verify that the TPS interior is intact and operational.

1. Using a multimeter, test the resistance across the positive and ground terminals on the TPS. This is nominally approx. 11Ω . The reading may vary by $\pm 1\Omega$, as there is some variation between needle assemblies.
 - a. A low reading implies an electrical short circuit within the TPS. The most likely cause is that the ceramic coating on the needle has been damaged, or that the set screw on the lower hub has been overtightened. See instructions for needle replacement.
 - b. A higher reading signifies a broken connection. The most likely culprit is the positive connection not making contact. Check that the brass plunger is properly seated. If it isn't loose and there is still an open connection, unscrew the brass plunger and look through the hole. A setscrew should be visible and roughly aligned with the axis of the hole ($\pm 1\text{mm}$). [Refer to Figure 8 in the *Needle replacement* section.] If it is not, follow instructions for needle replacement (it could just need to be reinstalled).

Note: Virtually all TPS problems will be related to this resistance not reading in the 10-12 Ω range. The TPS will collect particles almost exclusively by impaction (and just large particles) if proper voltage is not applied. Because the voltage converter does not provide current feedback, it is necessary to do an occasional check to ensure that all is well.

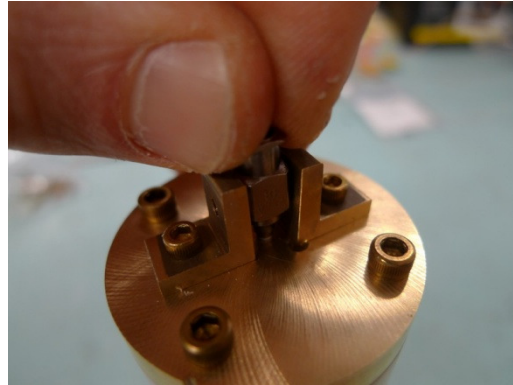
2. Gently, twist the Luer Lock connection with your fingers. It *should not* be loose or twistable. Tighten the two side brackets and setscrew that hold the Luer Lock (and thus the needle) in place. Repeat step #1.

Note: The most sensitive part of the TPS is the needle ceramic coating that is housed within the TPS body. If the needle is free to move (either in its axial direction or by twisting), the coating **will be damaged** by handling.

Figure 3. Steps for preparation



Step 1



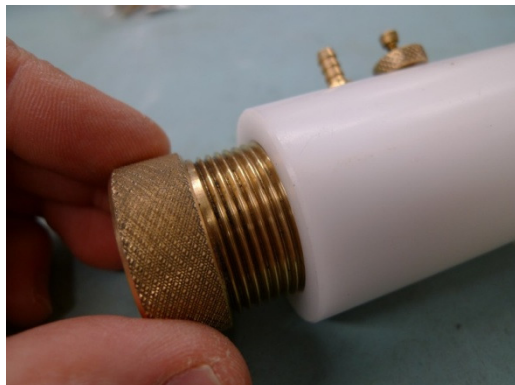
Step 2

TEM grid installation (see companion video)

3. Unscrew the brass base from the TPS body. Remove the (magnetic) nickel cap from the shaft. It should slide freely.
4. Using the tweezers, gently remove a TEM grid from its box, being careful to handle the grid by its edge only. Place the grid “shiny” side up on the brass shaft, using the lightly machined indentation as a guide to centering the grid. TEM grids are **easily damaged**. See note.
5. Replace the nickel cap with a slight twisting motion. It should slide very freely. If it does not, **do not** force it; remove and ensure that both the shaft and the cap interior are free of debris. When the cap is installed properly, a light magnetic pull should “snap” it in place.
6. Verify that an o-ring is in its groove inside the TPS body. Screw the brass base back into the TPS. When it is installed all the way, there will be a firm resistance. Do not overtighten past this point.

Note: TEM grids are extremely fragile. Take care to not drop, crease, or crumple the grid. If grid integrity is compromised, start with a new one; the cost of a TEM grid is low compared to the expense of wasted microscopy time.

Figure 4. Steps for TEM grid installation



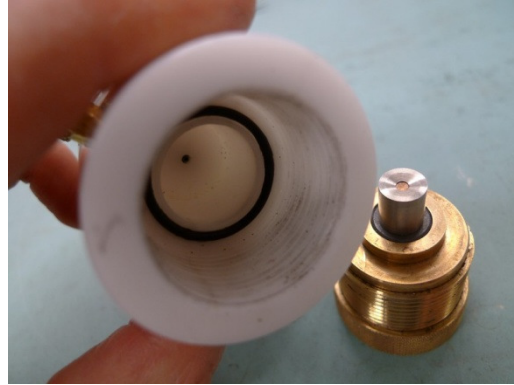
Step 3



Step 4



Step 5



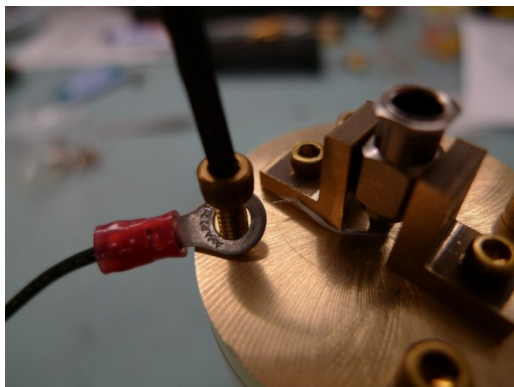
Step 6

Powering the TPS

7. Connect the black (ground) electrical terminal to one of the four brass #6-32 screws on top of the TPS (these hold the cap in place).
8. Connect the red (positive) electrical terminal to the screw on the plunger on the side of the TPS.
9. Connect both power leads to the black and red output wires on the “OUT” side of the voltage converter.
10. Connect power to the voltage converter by plugging in the provided DC power supply and inserting its jack into the “IN” side of the converter box. A green LED light in the controller should flicker briefly and then remain lit. The TPS is now powered. Warmup time is on the order of 10-20 seconds. If you wish, you can verify DC voltage output from the converter using a multimeter.

Note: The voltage converter is set to 12V, so why even use it (given that the provided power supply already gives this)? The reason is that the converter can change *any* 6-35 VDC power to a discrete output voltage. By chance, the provided power supply voltage equals the current setpoint for the TPS; this will not always be the case. N.B. the output voltage is user-adjustable via jumpers; contact Brian Just at UBC for instructions if this needs adjustment (see also Figure 11).

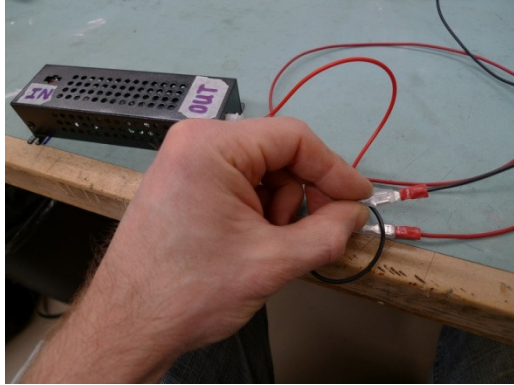
Figure 5. Steps for powering the TPS



Step 7



Step 8



Step 9



Step 10

Obtaining a TEM sample

11. The exhaust stream should be delivered to the TPS via a conductive tubing path. Connect the exhaust outlet to a flexible piece of black conductive silicon hose and slide this hose over the 3/16" barbed end of the stainless steel Luer Lock fitting (provided). Connect this Luer Lock fitting to the Luer Lock hub on the TPS. Tighten **by hand**; overtightening will damage the needle.
12. With TPS power on (steps 7-10), connect a pump to the TPS outlet (downstream side, 1/8" barbed connection on side) via a critical orifice.

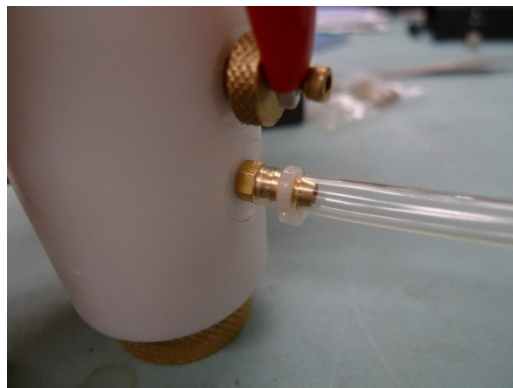
Note: Orientation of the TPS is not of critical importance; gravitational deposition is negligible. The magnetic TEM grid cap is designed to allow complete inversion of the instrument without slippage. For reference, with the recommended settings (power and flow rate), the cutoff diameter for impaction is estimated to be in the 250-300 nm range.

Warning: Aerosol exits the TPS at temperatures in excess of 400K; ensure that pump will not be damaged. A particulate filter may also be useful to reduce risk of damage to the pump.

Figure 6. Steps for obtaining a TEM sample



Step 11



Step 12

Determining sampling time

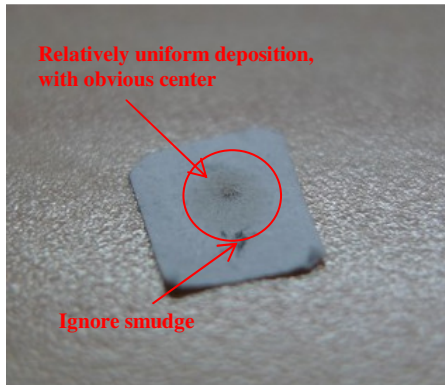
After exhaust/dilution setup is complete, proper sampling time must be established in order to collect enough particles to allow microscopy, while avoiding levels that would overload the grid. The following steps are recommended:

13. Load the TPS holder with a **clean white paper disc** in place of a TEM grid (steps 3-6).
14. With the exhaust stream and vacuum pump connected to the TPS and TPS power on, run consecutive samples of 10 second, 20 second, 30 second, etc. duration. Use a clean paper disc each time.

Incrementally increase sampling duration until tiny black specs are visible to the unaided eye on the paper surface. The dark sample spot should be just barely visible (to prevent grid overloading that makes it difficult to distinguish individual particles on the TEM). Refer to Figure 7, where a light deposition is visible over the outlined 3mm diameter ring; a slightly off-centered dark spot indicates the center of deposition.

15. Take the shortest sampling duration that reliably results in just-visible particulate loading and **subtract 10-15 seconds**. This gives a suitable final sampling duration. For reference, the sampling configuration used for the sample in Figure 7 required 60 seconds. Successful TEM grids were later analyzed using sampling times of 30 and 45 seconds.

Figure 7. Grid loading reference



Needle replacement (see companion video)

One spare needle assembly is provided. Done without training, needle replacement can be tricky and easily result in damage. Complete these steps only if necessary.

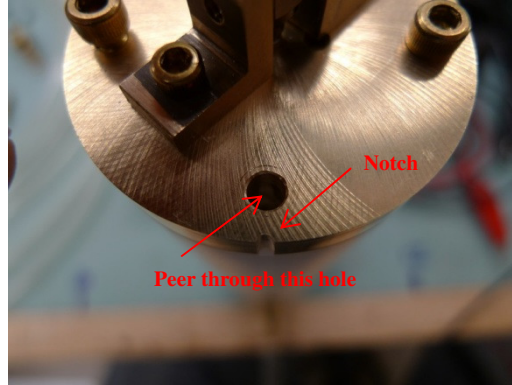
- a. If the exhaust stream is connected to the TPS, remove the Luer Lock connection.
- b. Remove the brass plunger (positive voltage connection).
- c. Remove the four brass screws that hold the brass cap in place (including the one providing the ground connection).
- d. **Carefully, while pulling on the Luer Lock hub**, slide the needle out of the TPS body. The entire needle assembly will come out. Place it on a clean workbench. Inspect the needle to determine why it is not working properly; use a multimeter and common sense. Typical problems include:
 - a. Short: chipped ceramic coating enables short circuit from Nichrome wire to needle; this normally happens near the brass cap or near the bottom (gray PEEK plastic) hub.
 - b. Short: overtightening of the setscrew in the bottom hub causes insulated setscrew tip to contact the needle. (This is a tricky problem; supplied needles are pretested with the setscrew properly aligned with the brass cap, and are just tight enough that the lower hub does not slip with respect to the needle during installation.)
 - c. Open: broken Nichrome wire.
- e. Fix any obvious problems. If this is not possible, proceed with the following steps to install the spare needle assembly.
- f. Ensure that the o-ring is still installed in its groove on the top surface of the TPS body. Check that the inside of the TPS is relatively free of debris.
- g. Check that the setscrew on the lower hub is roughly (± 5 deg) aligned with the notch on the brass cap. Then **carefully** slide the needle assembly into the TPS body with the **notch** in the brass cap **aligned with** the TPS air outlet. The hub on the bottom of the needle must slide into the locating hole in the TPS body. This is best done by “peering through” the mounting hole in the brass cap closest to the notch. Once it’s been started, **gently push** the needle assembly into place **by pressing down on the Luer Lock hub**; this ensures that there is no slippage between the brass cap and the needle (which will cause damage to the ceramic coating). There should be light resistance indicative of the locational clearance fit. The brass cap should rest flush with the TPS top surface.

- h. Immediately install at least two screws to attach the brass cap to the TPS body. Any twisting of the cap relative to the body will damage the ceramic coating.
- i. Double check that the needle assembly is properly aligned by looking through the hole for the brass plunger (positive voltage connection). See Figure 8 below. A setscrew should be visible and *roughly* aligned with the axis of the hole (± 1 mm). If it is not, repeat steps d-h, taking care that the setscrew on the hub aligns with the plunger hole. The needle can twist a few degrees to accommodate this, or the lower hub setscrew can be loosened and repositioned slightly (this is a last resort; the provided spare should be okay as is).
- j. Install all remaining screws and the brass plunger. Go to *Preparation Step 1* and check resistance.

Figure 8. Helpful views for needle installation: (a) visible setscrew indicates proper alignment, (b) hole to look through to help guide needle assembly lower hub into place



(a)



(b)

Additional reference

Figure 9, Figure 10 and Figure 11 show additional details.

Figure 9. TPS assembly drawing

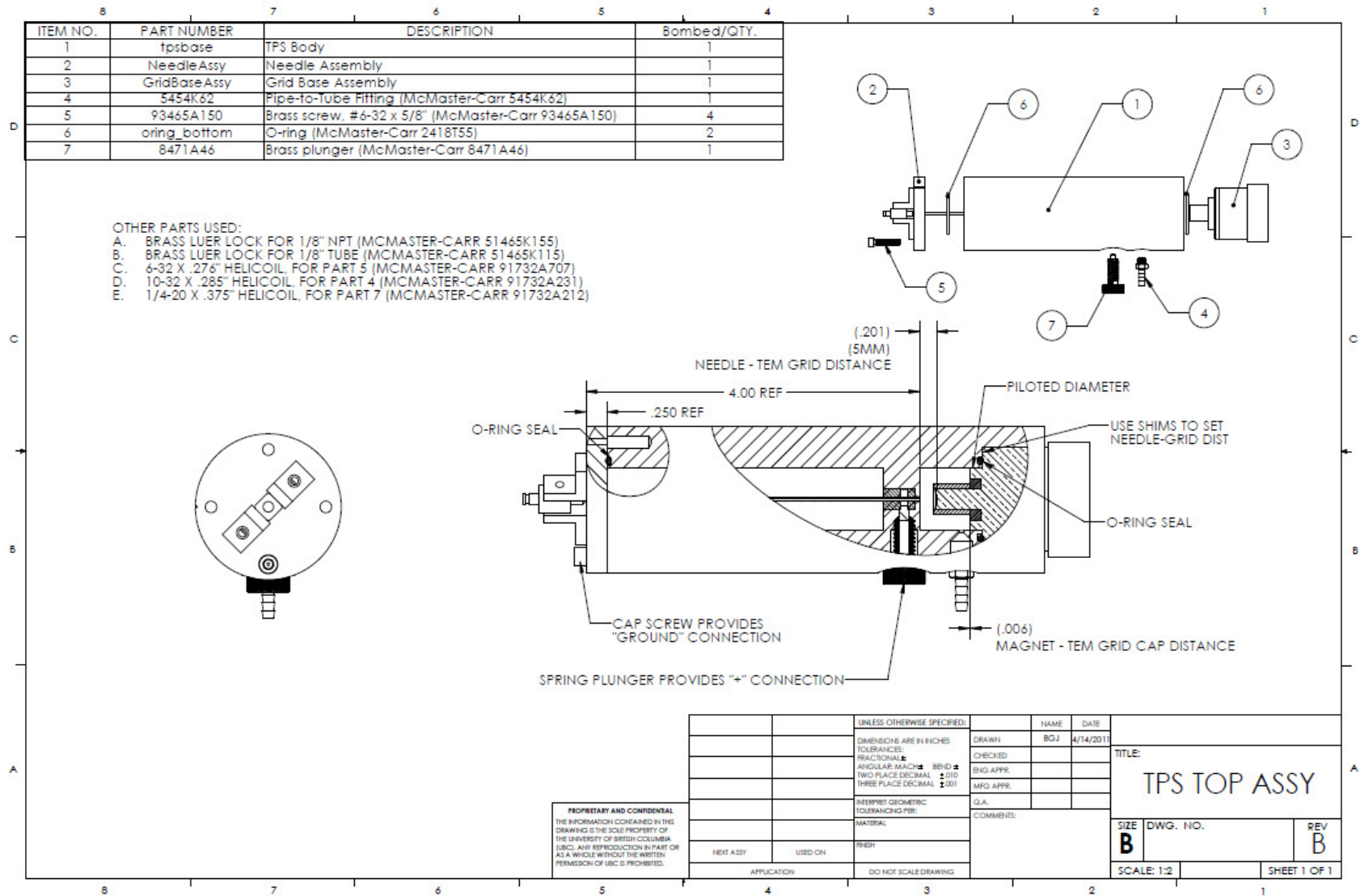
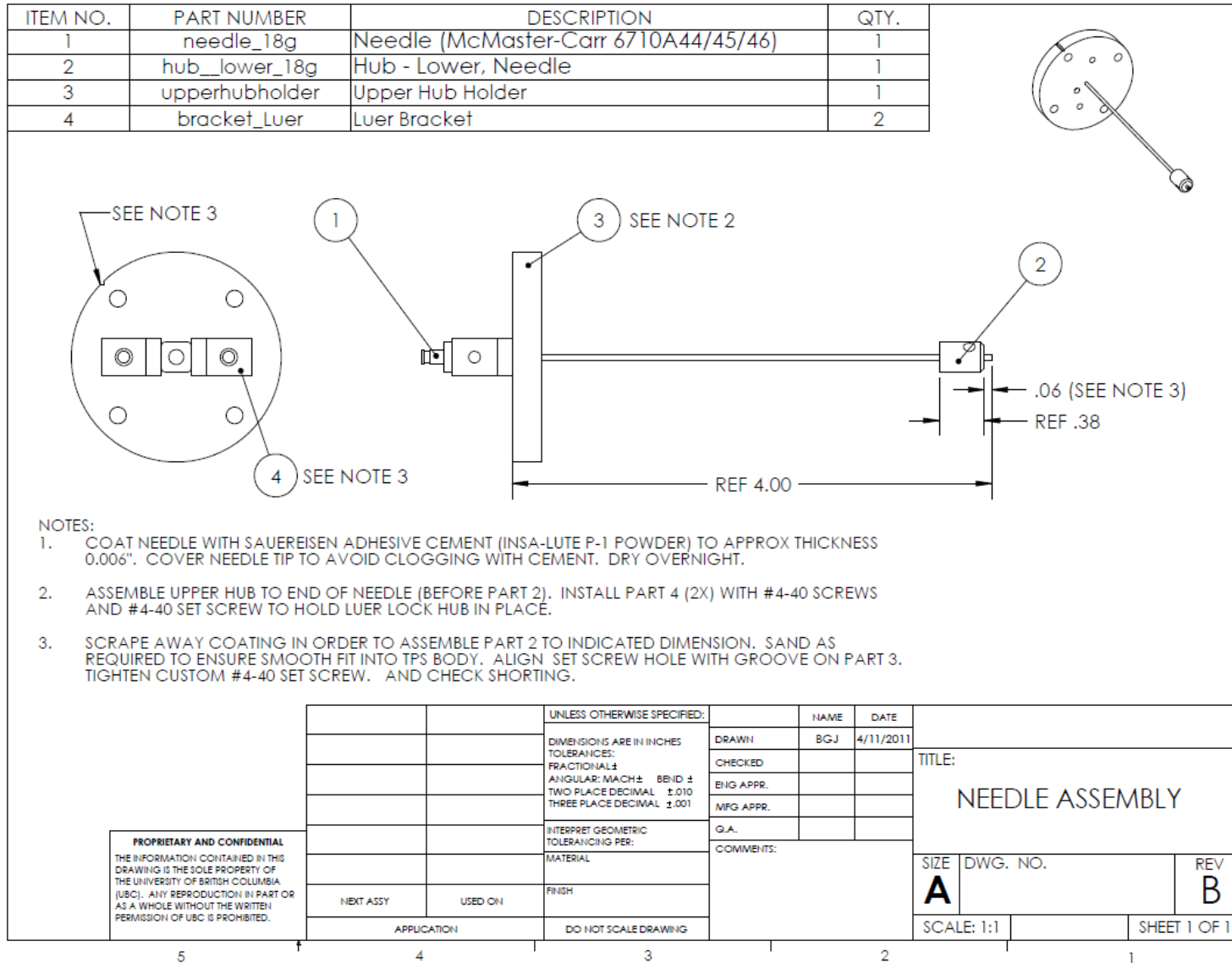


Figure 10. TPS needle assembly drawing



Output voltage		0	1	2	3	4	5	6	7
12V	<input type="checkbox"/>	<input type="checkbox"/>	<input type="checkbox"/>	<input type="checkbox"/>	<input type="checkbox"/>	<input type="checkbox"/>	<input type="checkbox"/>	<input type="checkbox"/>	<input type="checkbox"/>
5V	<input type="checkbox"/>	<input type="checkbox"/>	<input type="checkbox"/>	<input type="checkbox"/>	<input type="checkbox"/>	<input checked="" type="checkbox"/>	<input type="checkbox"/>	<input type="checkbox"/>	<input type="checkbox"/>
6V	<input type="checkbox"/>	<input type="checkbox"/>	<input type="checkbox"/>	<input type="checkbox"/>	<input checked="" type="checkbox"/>	<input type="checkbox"/>	<input type="checkbox"/>	<input type="checkbox"/>	<input type="checkbox"/>
9V	<input type="checkbox"/>	<input type="checkbox"/>	<input type="checkbox"/>	<input type="checkbox"/>	<input checked="" type="checkbox"/>	<input checked="" type="checkbox"/>	<input type="checkbox"/>	<input type="checkbox"/>	<input type="checkbox"/>
12V	<input type="checkbox"/>	<input type="checkbox"/>	<input type="checkbox"/>	<input checked="" type="checkbox"/>	<input type="checkbox"/>	<input type="checkbox"/>	<input type="checkbox"/>	<input type="checkbox"/>	<input type="checkbox"/>
13.5V	<input type="checkbox"/>	<input type="checkbox"/>	<input type="checkbox"/>	<input checked="" type="checkbox"/>	<input type="checkbox"/>	<input checked="" type="checkbox"/>	<input type="checkbox"/>	<input type="checkbox"/>	<input type="checkbox"/>
18V	<input type="checkbox"/>	<input type="checkbox"/>	<input type="checkbox"/>	<input checked="" type="checkbox"/>	<input checked="" type="checkbox"/>	<input type="checkbox"/>	<input type="checkbox"/>	<input type="checkbox"/>	<input type="checkbox"/>
24V	<input type="checkbox"/>	<input type="checkbox"/>	<input type="checkbox"/>	<input checked="" type="checkbox"/>	<input checked="" type="checkbox"/>	<input checked="" type="checkbox"/>	<input type="checkbox"/>	<input type="checkbox"/>	<input type="checkbox"/>

Figure 11. Default jumper settings for the DC-DC converter

Appendix G: Supplementary cookstove information

There are four models of the Chulika cookstove available. The CAMS 3 model was purchased (for INR 1633, C\$36) in India by Conor Reynolds in August 2012. It has a cast iron top plate, calcium carbonate ceramic block combustion chamber, 310 stainless steel inner shield, fired clay bottom tile, cast iron inner grate, and a 304 stainless steel outer hood. It is distributed by iSquareD, Bangalore, India.

The Oorja cookstove is distributed by First Energy (P) Ltd., Bangalore, India. It was purchased in India by Conor Reynolds in August 2012 for INR 1050 (C\$21).

Appendix H: Biomass fuel discussion and supplementary details

Ideally, the same fuel type and form would be combusted in all cookstoves. For the pellet-burning Oorja, tests were done with small pieces of wood and wood chips, but the resulting flame burned quickly and only for a few minutes; gasification was clearly not occurring in the way the stove was designed for. Only slightly better results were obtained by tightly packing the combustion chamber with vertically-oriented sticks. Conversely, an attempt was made to burn pellets in the three-stone fire and the Chulika cookstove. However, surface combustion dominated; the small pellets did not permit sufficient airflow through the fuel for satisfactory combustion. Testing proceeded with each stove using a fuel suitable to its design. Future testing could attempt to separate fuel shape from stove design in an evaluation of combustion characteristics, but this was not addressed in this study.

The pellets used in this research were manufactured by Premium Pellet Ltd., Vanderhoof, BC, V0J 3A0, Canada. They are packaged in 40 lb. bags; see Figure 36.



Figure 36. Wood pellet photograph

CHN analyses were completed at the UBC Mass Spectrometry Centre. Lab results appear on the following two pages and are summarized in Table 22.

Table 22. Fuel elemental analysis summary (numbers represent percentage dry mass)

Fuel	Carbon	Hydrogen	Nitrogen
Hemlock wood sticks	47.53	6.23	0.00
Premium Pellet Ltd. wood pellets	47.70	6.52	0.00

UNIVERSITY OF BRITISH COLUMBIA
Department of Chemistry
2036 Main Mall, Vancouver, BC V6T 1Z1
Tel: 604-827-4212, Fax: 604-822-2847

M.A.# E.A 8116
Date 05 MAR 2012

Request for Microanalysis Services

Submitted By: Brian Just

Supervisor: Rozak (Mech. Eng.)

Contact (tel. # and/or e-mail) [REDACTED]

Sample Name: CETL-HEM

Sample Information

Formula: Hemlock shavings

Call for sample drop off Ph#.....

Weigh under N₂? _____

Stability _____

Hygroscopic: _____

Volatile: _____

Sample storage: _____

Solvents used:

Hexane....., DCM....., MeCN....., MeOH..... THF...

H₂O....., Ether..., other.....

Theoretical or Range:

45 % N *approx*
50 % C
5 % H
____ % [Other]

MINIMUM WT REQUIRED FOR ANALYSIS ~ 5mg

Additional Information (if known)
Structure or Origin Confirmed by:

MS ----, NMR.... Other (Specify).....
(Provide analysis #)

Results (filled by analyst):

Elements determined	%N	%C	%H	
Analytical Results	<u>6</u>	<u>47.53</u>	<u>6.23</u>	

MAR 15 2012

UNIVERSITY OF BRITISH COLUMBIA
Department of Chemistry
2036 Main Mall, Vancouver, BC V6T 1Z1
Tel: 604-827-4212, Fax: 604-822-2847

M.A.# E.A 8117
Date 05 MAR 2012

Request for Microanalysis Services

Submitted By: Brian Just

Supervisor: Rajak

Contact (tel. # and/or e-mail) [REDACTED]

Sample Name: CET2-CP

Sample Information

Formula: Wood pellet powder

Call for sample drop off Ph#.....

Weigh under N₂? _____

Stability _____

Hygroscopic: _____

Volatile: _____

Sample storage: _____

Solvents used:

Hexane....., DCM....., MeCN....., MeOH.... THF...

H₂O....., Ether... , other.....

Theoretical or Range:

_____ % N

_____ % C

_____ % H

_____ % [Other]

MINIMUM WT REQUIRED FOR ANALYSIS ~ 5mg

Additional Information (if known)

Structure or Origin Confirmed by:

MS ---, NMR..., Other (Specify).....
(Provide analysis #)

Results (filled by analyst):

Elements determined	%N	%C	%H	
Analytical Results	∅	47.70	6.52	

RS
MAR 15 2012

Moisture content of the two fuels was reported on a dry basis. Regarding protocol, the following text is extracted from WBT 4.1.2, Appendix 1, Section 1.3 (Anon. 2009):

“Well-dried fuel contains 10-20% water while fresh cut wood may contain more than 50% water by mass (wet basis)...

“There are two ways of defining fuel moisture content: on a wet basis and on a dry basis. In the former, the mass of water in the fuel is reported as a percentage of the mass of wet fuel and in the latter case, it is reported as a percentage of the mass of the dry fuel. The calculations for each are shown below followed by a plot showing how both wood moisture on a wet basis and wood mass vary with wood moisture defined on a dry basis for one kg of oven-dry wood...

“The two moisture contents are related in this way:

$$MC_{wet} = \frac{MC_{dry}}{1 + MC_{wet}}$$

“Measuring moisture content can be done in two ways. The most precise way is to use the equations listed above by weighing a sample of the air-dry fuel (Mass of fuel)_{wet} and weighing it again after it has been completely dried (Mass of fuel)_{dry}. Take a small sample (200-300 g) of the fuel randomly from the stock of fuel to be used for the tests. Weigh the sample and record the mass...

“To dry the sample, put it in an oven overnight and then remove it and weigh the sample every two hours on a sensitive scale (± 1 g accuracy) until the mass no longer decreases. The oven temperature should be carefully controlled so that it doesn't exceed 110°C (230°F). If the wood is exposed to temperatures near 200°C (390°F), it will thermally break down and lose matter that is not water, causing an inaccurate measurement of moisture content.

“A second way to measure wood moisture is with a wood moisture meter. This device measures fuel moisture on a dry basis by measuring the conductivity between two sharp probes that are inserted in the wood. This is more convenient than oven-drying because the measurement can be rapidly done on site as the fuel is being prepared. The probes should be inserted parallel with the grain of the wood. The device may be adjusted for different species and calibrated for different ambient temperatures. The meter measures between 6% and 35-40% moisture (dry basis). If the sample of wood is wetter than the upper range of the meter, the meter will either show an error. Wood moisture can vary in a given piece of wood as well as among different pieces from a given bundle. When the meter is used, take three pieces of wood randomly from the bundle and measure each piece in three places. This yields nine measurements overall. The moisture of the bundle should be reported as the average of these nine measurements...”

Figure 37 displays raw data taken for the moisture content calculation with summary calculations highlighted in blue.

CAWP oven set to 105C										
Pellet container mass	6.6768	g								
				Wood sticks						
Date/time	Elapsed, h	Pellets (+cont), g	Pellets	1	2	3	4	5	Sum 1-5	
Mar 1, 9.30a	0.0	178.9682	172.2914	34.4878	49.1726	47.7638	49.3366	53.2724	234.0332	
Mar 2, 1.00p	27.5	168.0595	161.3827	31.4702	45.0074	43.6993	45.1292	48.7257	214.0318	
Mar 2, 4.00p	30.5	168.0411	161.3643	31.4893	44.9906	43.6986	45.128	48.7455	214.052	
Mar 5, 4.30p	103.0	167.9383	161.2615	31.4874	44.993	43.6982	45.1236	48.7598	214.062	
Mar 7, 10.00a	144.5	167.782	161.1052	31.4581	44.8741	43.6207	45.0203	48.6701	213.6433	
		mH2O	11.1862	3.0297	4.2985	4.1431	4.3163	4.6023	20.3899	
		M_{wb}	6.49%	8.78%	8.74%	8.67%	8.75%	8.64%	8.71%	
		M_{db}	6.94%	9.63%	9.58%	9.50%	9.59%	9.46%	9.54%	

Figure 37. Moisture content analysis raw data

Appendix I: Summary of testing protocol procedures

The following checklist was used during cookstove testing.

1. Background data:
 - a. Fan on
 - b. Verify clock synchronization
 - c. Background CO₂ line hooked up
 - d. LabView and AVL record data minimum 10 mins
 - e. Aethalometer on with several background measurements
 - f. Three SMPS scans (135 s each)
 - g. Three APS scans (135 s each)
2. Oorja: (approx 45 mins)
 - a. Set secondary dilution for aethalometer; disconnect aethalometer during start-up phase to prevent heavy loading and instrument “reset”
 - b. Load stove with 700g pellets (started with 1 tsp alcohol) with 5kg water set to boil
 - c. Video records flame condition at top
 - d. SMPS and APS scans throughout
 - e. Record temp and RH afterwards (quick LabView run)
 - f. Video off, end AVL data
 - g. During three test series, collect quartz and PTFE filters
 - h. During three test series, collect TEM grid samples
3. Chulika: (approx 80 mins)
 - a. Set secondary dilution for aethalometer; disconnect aethalometer during start-up phase to prevent heavy loading and instrument “reset”
 - b. Start five sticks with 1 tsp alcohol and several slivers of tinder with 5kg water set to boil
 - c. Transition to four-stick burn
 - d. Video records flame condition at stove entrance
 - e. SMPS and APS scans throughout
 - f. First ~20 mins is transition phase; continue steady-state burn for 60 mins past this
 - g. Record temp and RH afterwards (quick LabView run)
 - h. Video off, end AVL data
 - i. During three test series, collect quartz and PTFE filters
 - j. During three test series, collect TEM grid samples
4. Three-stone: (approx 70 mins)
 - a. Set secondary dilution for aethalometer; disconnect aethalometer during start-up phase to prevent heavy loading and instrument “reset”

- b. Immediately after Chulika test, transition burn remnants to a three-stone fire; build up with additional sticks; top with 5kg water set to boil
- c. First ~10 mins is transition phase; continue steady-state burn for 60 mins past this; aim for similar feed rate (~ four sticks) as Chulika, with similar [CO₂] levels
- d. Video records flame condition
- e. SMPS and APS scans throughout
- f. Continue steady-state burn for 60 mins once reached
- g. Record temp and RH afterwards (quick LabView run)
- h. Video off, end AVL data
- i. During three test series, collect quartz and PTFE filters
- j. During three test series, collect TEM grid samples

Repeat testing notes:

- k. Steps 3-5 comprise about 3.5 hrs of setup/testing time
- l. Oorja and Chulika require a cool combustion chamber; testing in this sequence gives adequate time for cooling

Appendix J: Sample data sheet from cookstove test

General info

04 Mar Date

1140 Time

Chulike #3 Stove/test number

_____ Other info

Preparation checklist

- Fan on
- FID flame on
- AVL bench Autocal
- Fire extinguisher on hand
- Clocks synchronized (LabVIEW, SMPS, and Emissions bench)
- _____ PC = n _____ aethalometer
- Background CO2 line hooked up
- Aethalometer data card installed
- Aethalometer on, with several background measurements
- Dilution voltage 2.49 V
- Verify APS COM7 connection to PC (do not unplug USB once it's working!)
- Change APS scan time to 135s (on PC via software)
- SMPS sample flow okay?
- 0.28 Flow rate (lpm)
- 5kg water ready
- Unused PM lines capped
- Filter pump off
- Filter line ball valve closed
- TPS ball valve off
- Prepare filters (enter ID's below)
- Prepare fire starter
- Video setup (MyCam: Device/Video Format/320x240 and 15 FPS)
- APS pump on

Background testing

1146 Emissions bench start time

50 LabVIEW DustTrak analog conversion factor

1147 LabVIEW start time

Auxiliary temp/RH display?

1147 _____ LabVIEW file name

TestH-010 DustTrak file name
1147 SMPS scan #1 1147 APS scan #1
1150 SMPS scan #2 1150 APS scan #2
1155 SMPS scan #3 1155 APS scan #3
Mar04-Chulika3 SMPS file name
Mar04-Chulika3 APS file name
 10 minutes (minimum) passed

Filters

Filter pump on
122121 Start time
Tef-08 Teflon filter label
1 Orifice number
Q-015 Quartz filter backup label
Q-016 Quartz filter label
2 Orifice number
 Filter pump off
122800 End time
180 ug Estimated loading

Coarse wavy
 Fine screen
 Quartz filter (moon side up)
 Teflon washer
 Fine Screen
 Teflon filter
 Teflon washer
 O-ring

} PM in 5-10 range (lower than prev. filters)
 Aim for ~150 ug
 < 10 mins
 50 ug after 2 min

Final preparation

Disconnect aethalometer
 Start fire
1158 Fire start time
 Video on
1158 Video start time
 Fire started?

Testing!

Reconnect aethalometer 2.50V
1159 Time aethalometer hooked up again
 Pot on to boil
 Temp probe in pot

<u>1200</u> SMPS scan #4	<u>1200</u> APS scan #4	_____	Notes
<u>1203</u> SMPS scan #5	<u>1203</u> APS scan #5	_____	Notes
<u>1206</u> SMPS scan #6	<u>1206</u> APS scan #6	_____	Notes

Remember: Real-life fire not steady-state, either; marked by tending + irregularity

Continue to monitor aethalometer, DustTrak readings

26 approx aethalometer 20 approx DustTrak 2.50
1209 SMPS scan #7 1209 APS scan #7 _____ Notes
1212 SMPS scan #8 1212 APS scan #8 _____ Notes
1215 SMPS scan #9 1215 APS scan #9 _____ Notes

Continue to monitor aethalometer, DustTrak readings

30 approx aethalometer 1.5 approx DustTrak 2.50 Dilution volt

"Steady"

✓ Chulika: Start filter collection

1218 SMPS scan #10 1218 APS scan #10 4-stick burn Notes
1221 SMPS scan #11 1221 APS scan #11 filters started Notes
1224 SMPS scan #12 1224 APS scan #12 _____ Notes

Continue to monitor aethalometer, DustTrak readings

12 approx aethalometer 3 approx DustTrak 2.49
1228 SMPS scan #13 1228 APS scan #13 filters done Notes
1231 SMPS scan #14 1231 APS scan #14 Aeth tape advance @ 1231 Notes
1234 SMPS scan #15 1234 APS scan #15 _____ Notes

Continue to monitor aethalometer, DustTrak readings

_____ approx aethalometer 3 approx DustTrak 2.49 Dilution volt

Water close to boiling?

1241 Water change time

1237 SMPS scan #16 1237 APS scan #16 _____ Notes
1243 SMPS scan #17 1243 APS scan #17 _____ Notes
1246 SMPS scan #18 1246 APS scan #18 _____ Notes

Continue to monitor aethalometer, DustTrak readings

60 approx aethalometer 10 approx DustTrak 2.49 Dilution volt
1249 SMPS scan #19 1249 APS scan #19 _____ Notes
1252 SMPS scan #20 1252 APS scan #20 _____ Notes
1255 SMPS scan #21 1255 APS scan #21 _____ Notes

Continue to monitor aethalometer, DustTrak readings

95 approx aethalometer 10 approx DustTrak 2.49 Dilution volt
1258 SMPS scan #22 1258 APS scan #22 _____ Notes
1301 SMPS scan #23 1301 APS scan #23 _____ Notes
1304 SMPS scan #24 1304 APS scan #24 _____ Notes

Continue to monitor aethalometer, DustTrak readings

80 approx aethalometer 2 approx DustTrak 2.49 Dilution volt

End ~
1318

1307 SMPS scan #25 1307 APS scan #25 _____ Notes

1310 SMPS scan #26 1310 APS scan #26 _____ Notes

1313 SMPS scan #27 1313 APS scan #27 _____ Notes

Continue to monitor aethalometer, DustTrak readings

76 approx aethalometer 12 approx DustTrak 2.50 Dilution volt

_____ SMPS scan #28 _____ APS scan #28 _____ Notes

_____ SMPS scan #29 _____ APS scan #29 _____ Notes

_____ SMPS scan #30 _____ APS scan #30 _____ Notes

TEM

1psi TEM pump setting (pressure drop) [0.5psi=1.4lpm, 1.0psi=2.3lpm, 2.0psi=3.3lpm]

131705 Collection time, based on target of at least 60 sec*mg/m3 (with 1psi pressure drop)

131740 Start time

35 s. End time

48 Grid label number

_____ Notes

Post test

Remove and package filters

APS pump off

DustTrak off

Shut down video

Turn off LabVIEW

Turn on LabVIEW for an instant to post-test temp/RH

Turn off AVL

2.51 Dilution voltage

Other notes

At start, feed a lot to get loads of char. @ 15 min, transition to a 4-stick burn

Stopped at H₂O boil #2

Appendix K: Gravimetric (PTFE filter) raw data, critical flow orifice calibration, and DustTrak repeatability

Filter mass data is tabulated in Figure 38; the final columns (at right) give the net mass of PM deposited, with reference to the cookstove test associated with the filter in question. Further compensations are made based on filter collection time and measurements from a dynamic blank.

Pretests March 02						Posttests March 12									
Label	m1, mg	m2, mg	m3, mg	avg	mx-mn	Label	m1, mg	m2, mg	m3, mg	avg	mx-mn	Diff, mg			
QC-01	187.031	187.034	187.034	187.033	0.003	QC-01	187.040	187.040	187.039	187.040	0.001	0.007			
QC-02	187.824	187.823	187.826	187.824	0.003	QC-02	187.827	187.826	187.825	187.826	0.002	0.002			
QC-03	187.635	187.633	187.631	187.633	0.004	QC-03	187.636	187.638	187.638	187.637	0.002	0.004			
												0.004 Avg			
Label	m1, mg	m2, mg	m3, mg			Label	m1, mg	m2, mg	m3, mg			Test	Time, s	DBadj diff, mg	
CET Tef-01	178.588	178.588	178.588	178.588	0.000	CET Tef-01	178.825	178.824	178.824	178.824	0.001	0.232	Oorja1	1934	0.175
CET Tef-02	174.751	174.754	174.751	174.752	0.003	CET Tef-02	175.098	175.094	175.098	175.097	0.004	0.340	Chulika1	910	0.314
CET Tef-03	189.554	189.549	189.551	189.551	0.005	CET Tef-03	189.883	189.881	189.884	189.883	0.003	0.327	3stone1	181	0.322
CET Tef-04	219.830	219.830	219.830	219.830	0.000	CET Tef-04	220.066	220.065	220.063	220.065	0.003	0.230	Oorja2	949	0.202
CET Tef-05	217.255	217.255	217.254	217.255	0.001	CET Tef-05	217.458	217.458	217.458	217.458	0.000	0.199	Chulika2	598	0.181
CET Tef-06	210.588	210.588	210.587	210.588	0.001	CET Tef-06	210.994	210.997	210.998	210.996	0.004	0.404	3stone2	360	0.394
CET Tef-07	203.257	203.264	203.263	203.261	0.007	CET Tef-07	203.488	203.490	203.488	203.489	0.002	0.223	Oorja3		
CET Tef-08	185.631	185.628	185.627	185.629	0.004	CET Tef-08	185.779	185.777	185.775	185.777	0.004	0.144	Chulika3		
CET Tef-09	176.229	176.231	176.232	176.231	0.003	CET Tef-09	177.360	177.362	177.358	177.360	0.004	1.125	3stone3		
CET Tef-10	182.722	182.718	182.721	182.720	0.004	CET Tef-10	183.301	183.297	183.297	183.298	0.004	0.574	--		
CET Tef-11	178.183	178.183	178.181	178.182	0.002	CET Tef-11	178.344	178.345	178.344	178.344	0.001	0.158	Oorja4	945	0.130
CET Tef-12	167.908	167.906	167.906	167.907	0.002	CET Tef-12	168.148	168.146	168.146	168.147	0.002	0.236	Chulika4	570	0.219
CET Tef-13	191.243	191.242	191.241	191.242	0.002	CET Tef-13	191.851	191.852	191.851	191.851	0.001	0.605	3stone4	419	0.593
CET Tef-14	185.941	185.942	185.942	185.942	0.001	CET Tef-14	186.383	186.382	186.381	186.382	0.002	0.436	Chulika5		
CET Tef-15	175.262	175.267	175.265	175.265	0.005	CET Tef-15	176.548	176.547	176.547	176.547	0.001	1.278	3stone5		
CET Tef-16	184.578	184.576	184.575	184.576	0.003	CET Tef-16	186.347	186.343	186.344	186.345	0.004	1.764	3stone6		
CET Tef-17	178.481	178.481	178.481	178.481	0.000	CET Tef-17	178.636	178.634	178.635	178.635	0.002	0.150			
CET Tef-18	174.948	174.944	174.945	174.946	0.004	CET Tef-18	174.977	174.976	--	174.977	0.001	0.027	Dyn blank	900	

Figure 38. Gravimetric raw data for PTFE filters

The orifice used to control flow through the PTFE filter was calibrated. Thirty measurements were taken; the average of all measurements is 6.3236 lpm. Figure 39 shows gravimetric mass (“m, filt,” Column 3) and PM mass from the DustTrak (“m, DT,” Column 4). DustTrak averages per stove are time weighted. Collection time is noted and the difference between the two numbers is noted and averaged.

Raw data for each stove / test over its steady burn period is averaged. Individual test averages are then averaged and standard deviation is reported. See Table 23.

Table 23. Averages of raw DustTrak data for each stove / test (all data in mg/m³)

Stove	Test 1	Test 2	Test 4	Averages
Three-stone	22.8	30.0	33.7	28.5 ± 5.6 (±20%)
Chulika	4.48	3.84	5.52	4.63 ± 0.84 (±18%)
Oorja	0.88	1.21	1.11	1.07 ± 0.17 (±16%)

Summary													
Test	Filter ID	m, filt	m, filt, w/DB adj	m, DT	diff	diff, w/DB adj	% diff	% diff, w/DB adj	coll time, s	DT_avg	q, m3/s		
Oorja1	Tef-001	0.232	0.175	0.166	-0.0660	-0.0088	-28.42%	-5.02%	1934	0.815	0.0926		
Oorja2	Tef-004	0.230	0.202	0.153	-0.0770	-0.0490	-33.43%	-24.20%	949	1.534	0.0921		
Oorja3	Tef-007	0.223		0.162	-0.0616		-27.60%						Uncorrected BC/PM (MATLAB):
Oorja4x	Tef-010	0.574		0.467	-0.1072		-18.68%						0.4839
Oorja4r	Tef-011	0.158	0.130	0.105	-0.0527	-0.0247	-33.37%	-19.03%	945	1.056	0.0916	corrected:	Corrected BC/PM:
							stdev		avg of 1,2,4	1.053		1.254	0.3303 w/o DB adj
					avg of 1,2,4		-31.74%	2.88%	-16.08%				0.4061 w/DB adj
					avg all		-28.30%	6.02%					(stdev)
Chulika1	Tef-002	0.3404	0.3135	0.3668	0.0264	0.0533	7.74%	16.99%	910	3.824	0.0913		
Chulika2	Tef-005	0.1991	0.1814	0.2254	0.0263	0.0439	13.19%	24.22%	598	3.576	0.0911		
Chulika3	Tef-008	0.1441		0.1886	0.0445		30.85%						Uncorrected BC/PM (MATLAB):
Chulika4	Tef-012	0.2358	0.2189	0.2695	0.0337	0.0506	14.31%	23.10%	570	4.486	0.0908		0.1622
Chulika5	Tef-014	0.4361		0.4959	0.0598		13.71%					corrected:	Corrected BC/PM:
							stdev		avg of 1,2,4	3.934		3.240	0.1813 w/o DB adj
					avg of 1,2,4		11.75%	3.51%	21.44%				0.1970 w/DB adj
					avg all		15.96%	8.73%					(stdev)
3stone1	Tef-003	0.327	0.322	0.924	0.5972	0.6025	182.56%	187.26%	181	48.453	0.0928		
3stone2	Tef-006	0.404	0.394	1.030	0.6253	0.6359	154.60%	161.48%	360	27.140	0.0927		
3stone4	Tef-013	0.605	0.593	1.588	0.9833	0.9957	162.49%	167.98%	419	35.969	0.0918		Uncorrected BC/PM (MATLAB):
3stone5	Tef-015	1.278		3.637	2.3583		184.47%						0.0230
3stone6	Tef-016	1.764		4.580	2.8158		159.61%					corrected:	Corrected BC/PM:
							stdev		avg of 1,2,4	35.012		12.860	0.0613 w/o DB adj
					avg of 1,2,4		166.55%	14.42%	172.24%				0.0626 w/DB adj
					avg all		168.75%	13.79%					(stdev)

Figure 39. Gravimetric vs. DustTrak PM mass comparison

Appendix L: Pollutant comparisons

Some comparisons excluded from the main text are interesting for reference. CO_2 is plotted vs. PM in Figure 40(a); Figure 40(b) shows more details due to x-axis rescaling. Figure 40(c-f) show similar detail for CO, CH_4 , and THC.

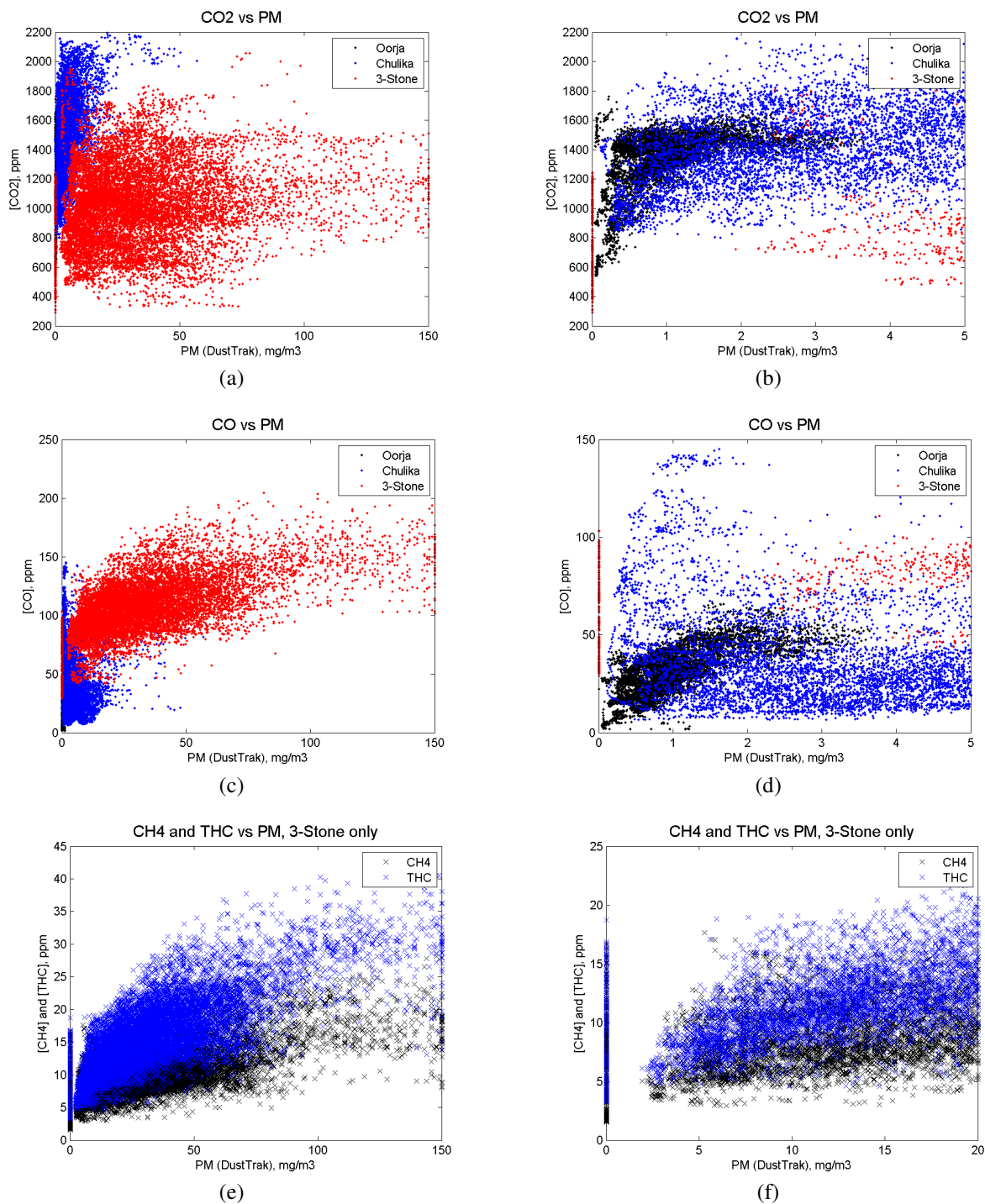


Figure 40. Gaseous pollutants vs. PM; (a), (c), and (e) show species as labelled; (b), (d), and (f) correspond to the previous plots with the x-axis adjusted to show greater detail

In Figure 40(a,b), it is observed that PM levels are significantly lower for the improved cookstoves vs. the three-stone fire, regardless of firepower (as indicated by CO₂ emissions levels), with the Oorja stove producing fewer particles than the Chulika.

Figure 40(c,d) indicates that the three-stone fire generally produces high levels of CO at the same time as PM with a roughly linear relationship between the two. The Oorja also shows a tendency to a linear relationship between increasing CO and PM (with both at significantly lower levels than the three-stone). Aside from some scatter (higher CO), the Chulika stove looks to exhibit relatively flat CO levels (within a wide band) with increasing PM.

Figure 40(e,f) shows CH₄ and THC vs. PM for the three-stone fire only (measured hydrocarbon emissions are negligible for the improved cookstoves). Both exhibit a roughly linear relationship; as PM emissions rise, so do CH₄ and THC emissions.

In summary, all gaseous PICs appear to be roughly linear with PM (itself a PIC). In other words, with incomplete combustion all PICs tend increase proportionally with some differences in relative amounts dependent on stove type.

Appendix M: Sunset Laboratory EC/OC analysis results

A summary of the method used by Sunset Laboratory is detailed below; full details of NIOSH Method 5040 are detailed by Schlecht and O'Connor (2003).

Part A

In a completely oxygen-free helium atmosphere, the sample is heated in four increasing temperature steps to remove all organic carbon on the filter. The transition from the third temperature to the fourth (from 500 °C to 700 °C) will quickly decompose inorganic carbonates, producing a sharp, characteristic peak. During this first phase there are usually some organic compounds that are pyrolytically converted to elemental carbon. As much as 30% of the organics may be pyrolytically converted to elemental carbon. This pyrolytic conversion is continuously monitored by measuring the transmission of a laser through the filter. As the organic compounds are vaporized, they are immediately oxidized to carbon dioxide in an oxidizer oven which follows the sample oven. The flow of helium, containing the carbon dioxide, then goes to a methanator oven where the CO₂ is reduced to methane. The methane, then, is detected by a flame ionization detector (FID).

Part B

After the sample oven is cooled to 525 °C, the pure helium eluent is switched to a 2% oxygen / helium mixture in the sample oven. Then the sample oven temperature is stepped up to 850 °C. During this phase, both the original elemental carbon and that produced by the pyrolysis of organics during the first phase (Part A) are oxidized to carbon dioxide due to the presence of oxygen in the eluent. The carbon dioxide, as in Part A, is then converted to methane and detected by the FID. As previously stated, the darkness of the filter is continuously monitored throughout all stages of the analysis.

Part C

After all carbon has been oxidized from the sample, a known volume and concentration of methane is injected into the sample oven. Thus, each sample is calibrated to a known quantity of carbon. This also provides a means of checking the operation of the instrument. Based on the FID response and laser transmission data, the quantities of organic and elemental carbon are calculated for the sample. (Sunset Laboratory 2010)

Raw data provided by Sunset Laboratory is shaded in Figure 41. Unshaded regions provide reference information about each filter.

Sample punch size: 1.50 x 1.00 cm		Corrected based on update (22 June 2012) sent by Sunset Labs														
Units ugC / cm ²																
Uncertainty +/- 5% of result (plus instrument LOD)																
Shaded is Sunset Orig Data																
Sample ID	OC(ug/sq cm)	OC unc	EC(ug/sq cm)	EC unc	TC(ug/sq cm)	TC unc	EC/TC ratio	Test	Notes	Collection time, s						
CET Q-01	1.69	0.18	0.00	0.10	1.69	0.28	0.000	Oorja 1	backup	1934						
CET Q-02	7.50	0.48	12.01	0.70	19.51	1.18	0.615	Oorja 1	Primary	(same)						
CET Q-03	2.52	0.23	0.00	0.10	2.52	0.33	0.000	Chulika 1	backup	910						
CET Q-04	8.11	0.51	16.67	0.93	24.79	1.44	0.673	Chulika 1	Primary	(same)						
CET Q-05	3.47	0.27	0.00	0.10	3.47	0.37	0.000	3Stone 1	backup	181						
CET Q-06	20.36	1.12	1.88	0.19	22.24	1.31	0.084	3Stone 1	Primary	(same)						
CET Q-07	2.18	0.21	0.00	0.10	2.18	0.31	0.000	Oorja 2	backup	949						
CET Q-08	6.55	0.43	13.04	0.75	19.60	1.18	0.665	Oorja 2	Primary	(same)						
CET Q-09	1.43	0.17	0.00	0.10	1.43	0.27	0.000	Chulika 2	backup	598						
CET Q-010	4.01	0.30	10.37	0.62	14.38	0.92	0.721	Chulika 2	Primary	(same)						
CET Q-011	4.06	0.30	0.00	0.10	4.06	0.40	0.000	3Stone 2	backup	360						
CET Q-012	21.16	1.16	5.15	0.36	26.31	1.52	0.196	3Stone 2	Primary	(same)						
Q-017	1.26	0.16	0.00	0.10	1.26	0.26	0.000	Oorja 4	backup	945						
Q-018	4.44	0.32	7.41	0.47	11.85	0.79	0.625	Oorja 4	Primary	(same)						
Q-018 Duplicate	4.68	0.33	7.01	0.45	11.70	0.78	0.600	Oorja 4	Primary	(same)						
Q-019	1.01	0.15	0.00	0.10	1.01	0.25	0.000	Chulika 4	backup	570						
Q-020	3.30	0.26	12.33	0.72	15.63	0.98	0.789	Chulika 4	Primary	(same)						
Q-021	4.07	0.30	0.00	0.10	4.07	0.40	0.000	3Stone 4	backup	419						
Q-022	34.48	1.82	4.22	0.31	38.70	2.14	0.109	3Stone 4	Primary	(same)						
Q-031/DB	3.04	0.25	0.00	0.10	3.04	0.35	0.000	Dynamic blank	backup	900						
Q-032/DB	3.53	0.28	0.00	0.10	3.53	0.38	0.000	Dynamic blank	Primary	(15 min dwell w/ room air)						
HB-001	0.19	0.11	0.00	0.10	0.19	0.21	0.000	Handling blank	n/a	(Prepared with others, never used)						
Theoretically perfect standard yield of 35.04ug of carbon																
Sucrose 35.04 ug	34.45	1.82	0.00	0.10	34.45	1.92	0.000									
Instrument blank	-0.04	0.10	0.00	0.10	-0.04	0.20	0.000									
Net (subtracting backup)																
Test	OC(ug/sq cm)	EC(ug/sq cm)	TC(ug/sq cm)	EC/TC ratio	EC/TC ratio	OC/TC ratio	Corresponding PTFE filter:			w/DB adjustment						
							PM mass (ug)	(ug/sq cm)*	EC/PM est	TC/PM est	PM mass (ug)	(ug/sq cm)*	EC/PM est	OC/PM est	TC/PM est	
Oorja 1	5.81	12.01	17.82	0.616	0.674	0.326	0.232	24.13	0.498	0.788	1.35	0.175	18.18	0.660	0.319	0.980
Oorja 2	4.38	13.04	17.42	0.665	0.749	0.251	0.230	23.95	0.544	0.727	1.38	0.202	21.04	0.620	0.208	0.828
Oorja 4	3.30	7.21	10.51	0.613	0.686	0.314	0.158	16.40	0.440	0.641	1.56	0.130	13.49	0.534	0.244	0.779
avg_Oorja	4.49	10.75	15.25	0.631	0.703	0.297		avg_Oorja	0.494	0.702	1.42		avg_Oorja	0.6049	0.2573	0.862
std_Oorja	1.26	3.11	4.11	0.030	0.040	0.040										
Chulika 1	5.59	16.67	22.27	0.673	0.749	0.251	0.340	35.39	0.471	0.629	1.59	0.314	32.59	0.512	0.172	0.683
Chulika 2	2.58	10.37	12.95	0.721	0.801	0.199	0.199	20.70	0.501	0.626	1.60	0.181	18.86	0.550	0.137	0.687
Chulika 4	2.28	12.33	14.61	0.789	0.844	0.156	0.236	24.51	0.503	0.596	1.68	0.219	22.75	0.542	0.100	0.642
avg_Chulika	3.48	13.13	16.61	0.728	0.798	0.202		avg_Chulika	0.492	0.617	1.62		avg_Chulika	0.5345	0.1362	0.671
std_Chulika	1.83	3.23	4.97	0.058	0.048	0.048										
3Stone 1	16.90	1.88	18.77	0.084	0.100	0.900	0.327	34.00	0.055	0.552	1.81	0.322	33.44	0.056	0.505	0.561
3Stone 2	17.10	5.15	22.25	0.196	0.232	0.768	0.404	42.04	0.123	0.529	1.89	0.394	40.93	0.126	0.418	0.544
3Stone 4	30.42	4.22	34.63	0.109	0.122	0.878	0.605	62.89	0.067	0.551	1.82	0.593	61.61	0.068	0.494	0.562
avg_3Stone	21.47	3.75	25.22	0.130	0.151	0.849		avg_3Stone	0.082	0.544	1.84		avg_3Stone	0.0835	0.4723	0.556
std_3Stone	7.75	1.69	8.34	0.059	0.071	0.071										
							* based on 3.5 cm dia circle			* based on 3.5 cm dia circle						

Figure 41. Sunset Laboratory summary

Repeatability can be roughly gauged by a comparison of EC/TC based on raw data for the three tests for each cookstove (with backup filter subtraction). For the three-stone, the average of the tests is 0.151 ± 0.071 . For the Chulika and Oorja, the averages are 0.798 ± 0.048 and 0.703 ± 0.040 , respectively. The three-stone displayed considerably higher variability between samples (based on standard deviation) as a percentage of average value.

Other notes:

- Filters were pre-baked at 700°C for one hour in order to remove carbon contamination.
- Before and after tests, filters were stored in 47mm diameter plastic containers, wrapped in foil, and frozen.

Appendix N: Emissions factors and GWP

Gaseous EFs are published in the text for completeness only and are useful only when factors such as cookstove efficiency are included. Likewise, though the data in Table 12 can be used to calculate GWP (in this case, GWP₁₀₀, 100-year GWP) as in Table 24, the information should not be interpreted without proper context.

Table 24. GWP comparison (without efficiency consideration)

Compound	GWP ₁₀₀	Three-stone	Chulika	Oorja
CO ₂	1 ^a	1524	1695	1707
CH ₄	25 ^a	141		
CO	1.9 ^a	192	51	48
NMHC	3.4 ^a	34		
EC	455 ^b	364	905	309
OC	-35 ^b	-159	-18	-10
	Sum	2096	2634	2054
	Sum, relative to three-stone	1.00	1.26	0.98

^a Ref: (Intergovernmental Panel on Climate Change 2007)

^b Ref: (Reynolds and Kandlikar 2008)

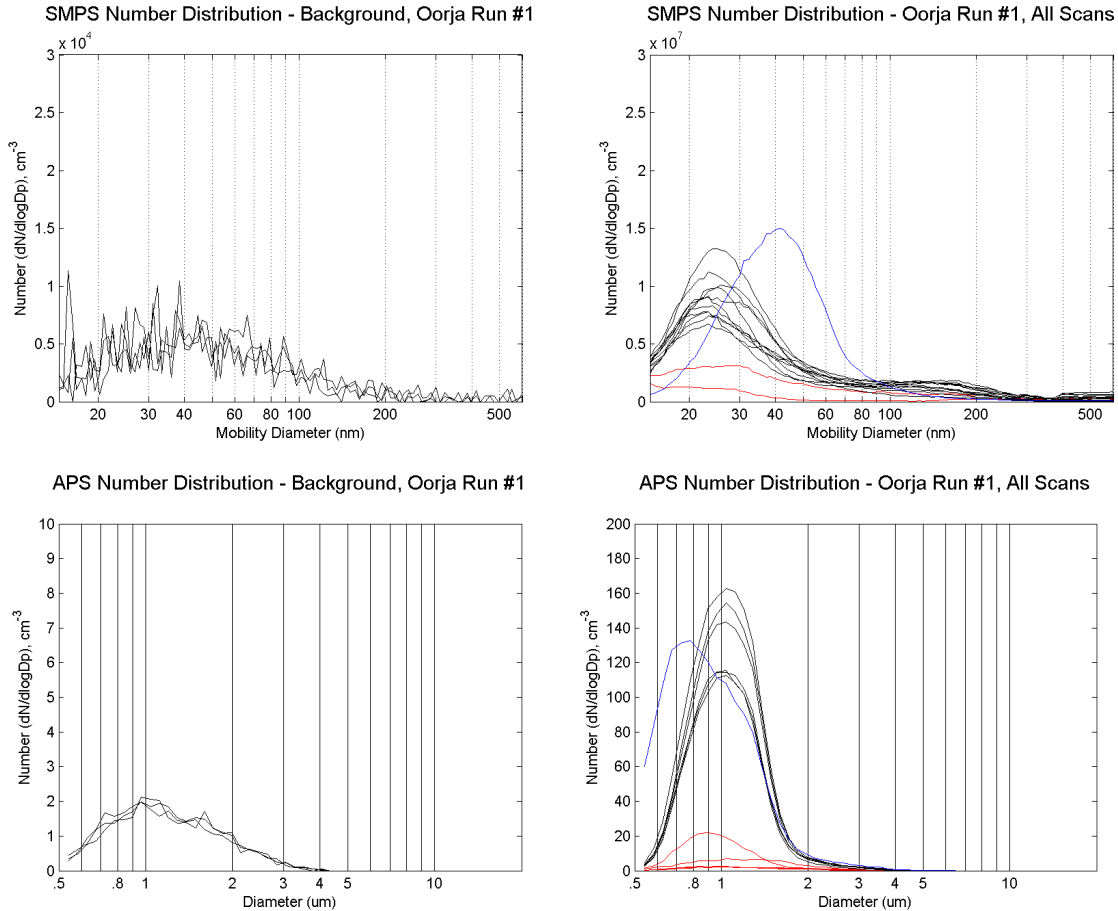
This demonstrates that on a per-fuel consumed basis (i.e., without accounting for efficiency gains by improved stoves), from a global warming perspective the improved stoves offer little or no improvement. Recall that the perfect stove would emit only CO₂; if the hemlock used (47.53% carbon by dry weight) were perfectly burned, it would emit 1743 g of CO₂ per kg dry fuel and nothing else. Avoidance of gaseous products with high GWP₁₀₀ such as CH₄ (of which the improved stoves emitted negligible amounts) and avoidance of EC particulates are beneficial for a good GWP “score.” Creation of (light scattering, global cooling) OC actually improves the score and helps account for the three-stone seeming “better” than the Chulika in this cursory investigation.

When included with results, the gain in efficiency achieved via use of an improved cookstove (i.e., the fact that less fuel is required) is likely to lower net GWP. The literature offers many examples of studies that compare the efficiency of traditional vs. improved cookstoves in terms of tangible performance criteria such as mass of a given pollutant per litre of water boiled.

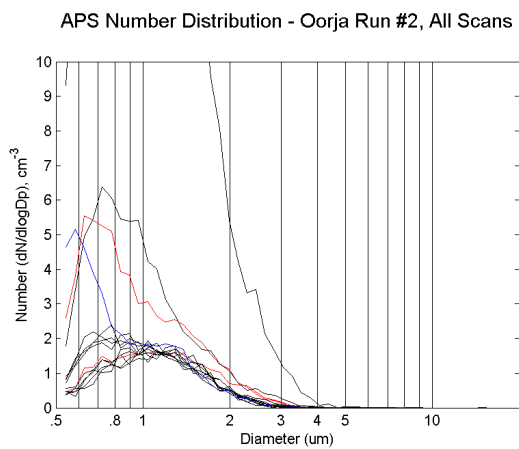
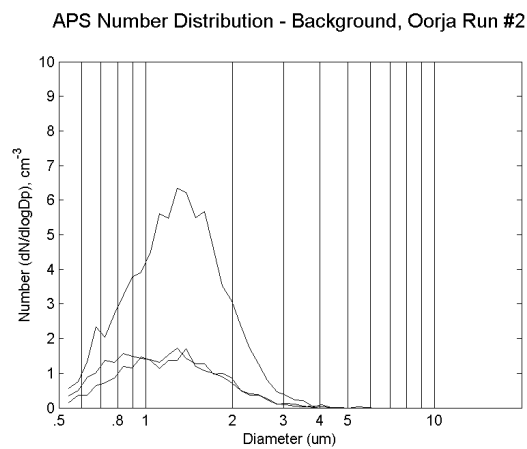
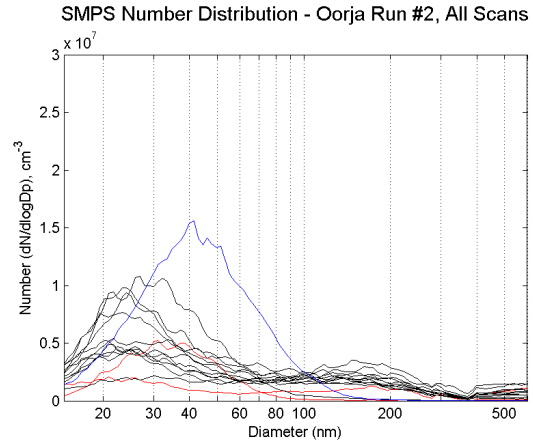
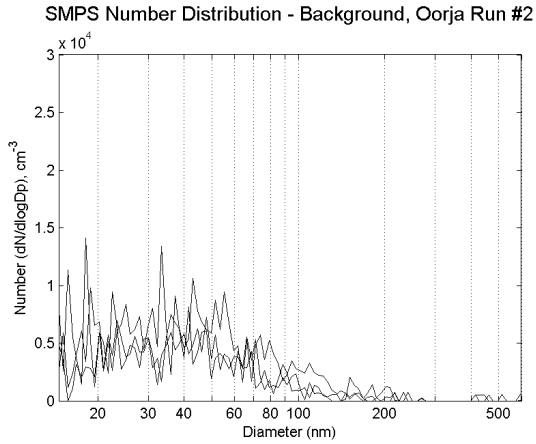
Appendix O: Overview of SMPS and APS scans

The following pages show minimally processed summaries of SMPS and APS scans taken for each cookstove test. Background scans appear to the left of scans taken during actual tests. Valid tests #1, 2, and 4 are presented along with a test (#6) that demonstrates problems encountered during some tests.

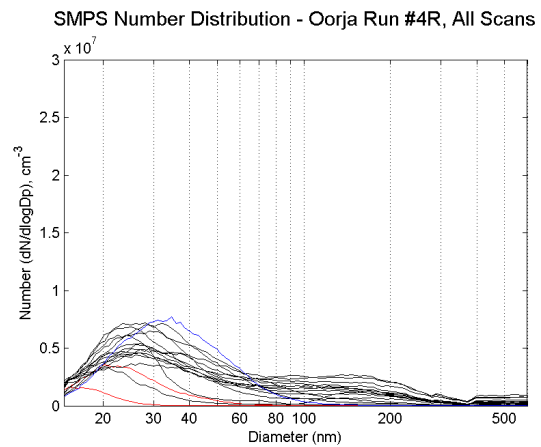
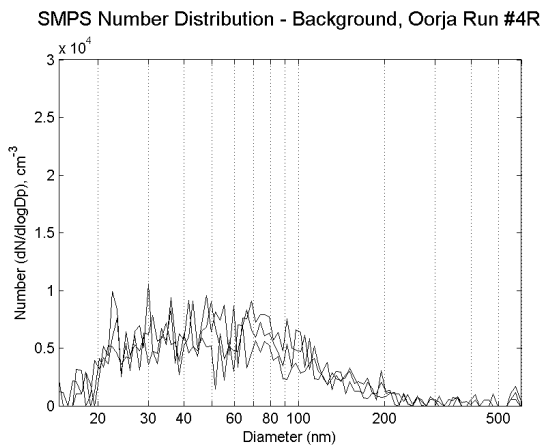
O.1 Oorja cookstove



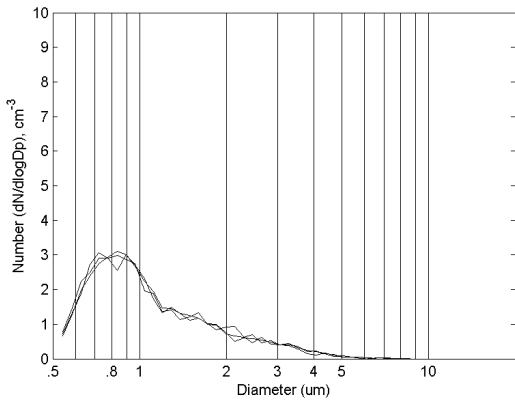
In the preceding set of plots, for the SMPS red indicates the first two runs after background (#4,5) while blue is the final run (#17). For the APS, red indicates the first few runs after background (#4-10) while blue is the final run (#17).



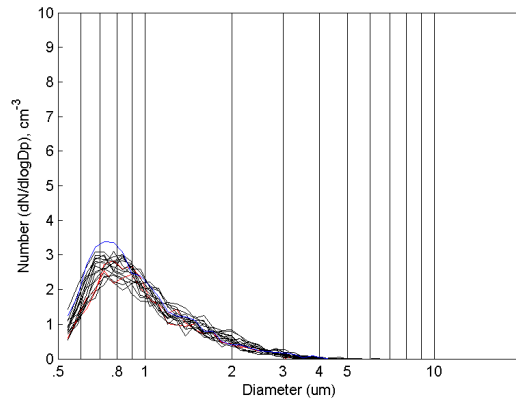
In the preceding set of plots, for the SMPS red indicates the first two runs after background (4,5) while blue is the final run (17). For the APS, red indicates the first few runs after background (4,5) while blue is the final run (17). Other apparent outliers are randomly in between.



APS Number Distribution - Background, Oorja Run #4R

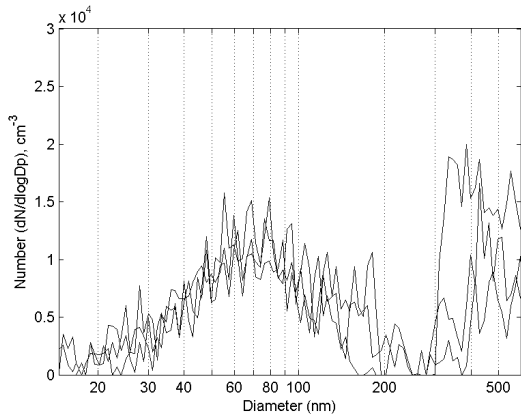


APS Number Distribution - Oorja Run #4R, All Scans

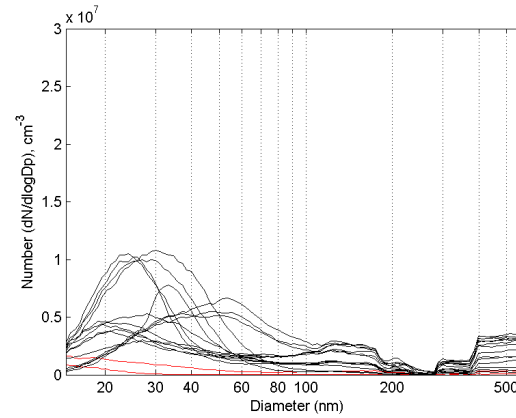


In the preceding set of plots, for the SMPS red indicates the first two runs after background (4,5) while blue is the final run (20). For the APS, red indicates the first two runs after background (4,5) while blue is the final run (20).

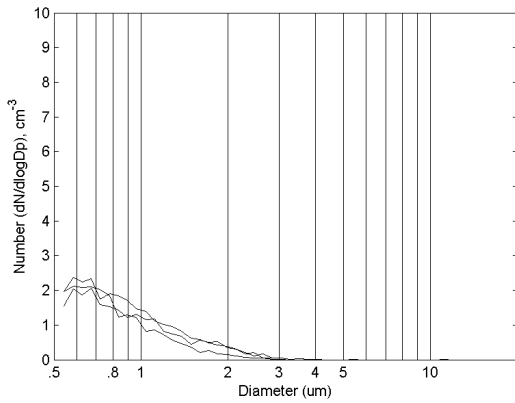
SMPS Number Distribution - Background, Oorja Run #6



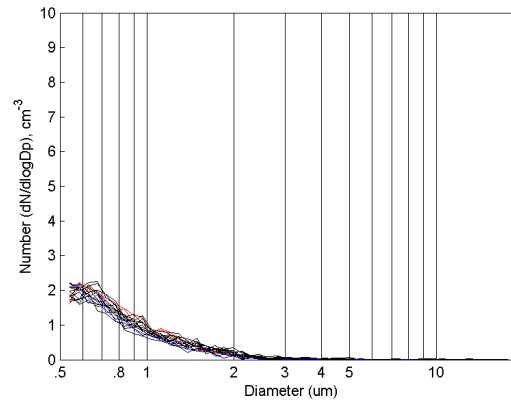
SMPS Number Distribution - Oorja Run #6, All Scans



APS Number Distribution - Background, Oorja Run #6



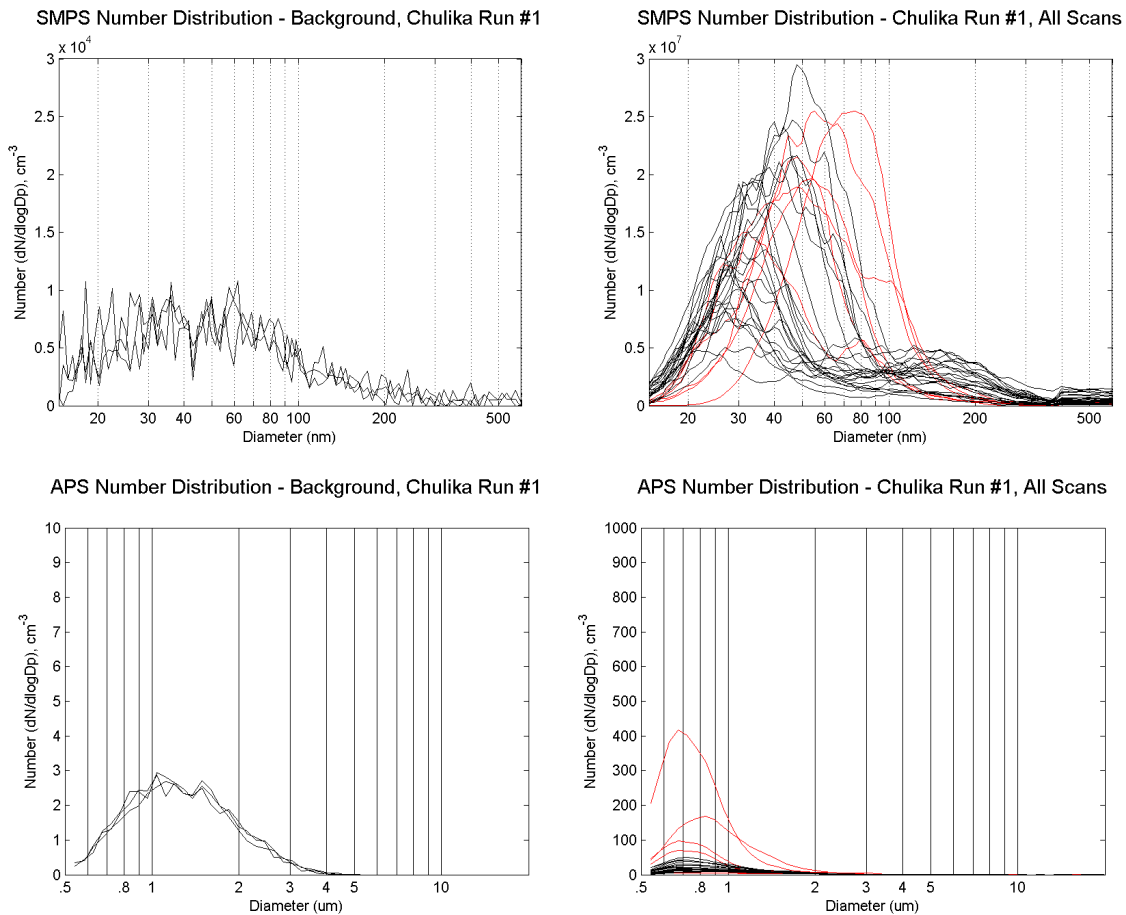
APS Number Distribution - Oorja Run #6, All Scans



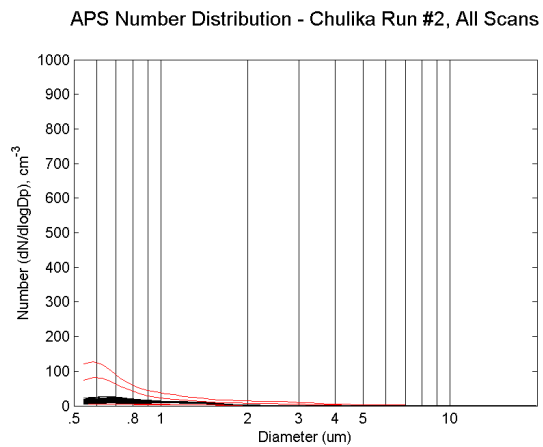
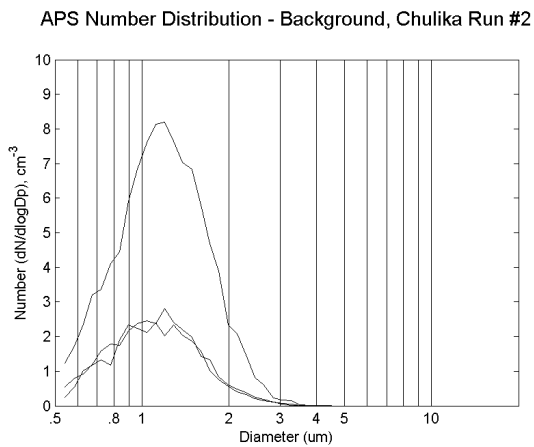
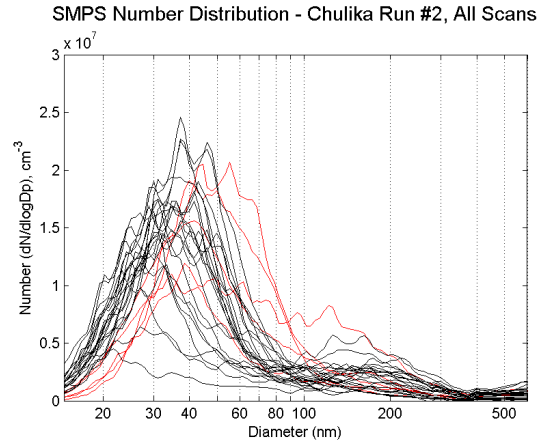
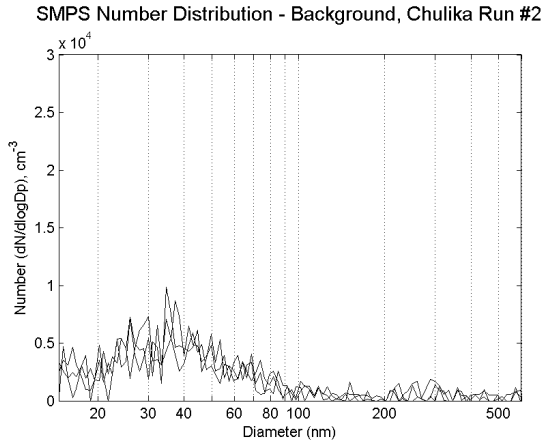
In the preceding set of plots, for the SMPS red indicates the first two runs after background (4,5). For the APS, red indicates the first two runs after background (4,5) while blue is the final run (19). These plots are included as an example of the “strange” SMPS data above 300 nm for tests excluded from the analysis. Further discussion appears later.

O.2 Chulika cookstove

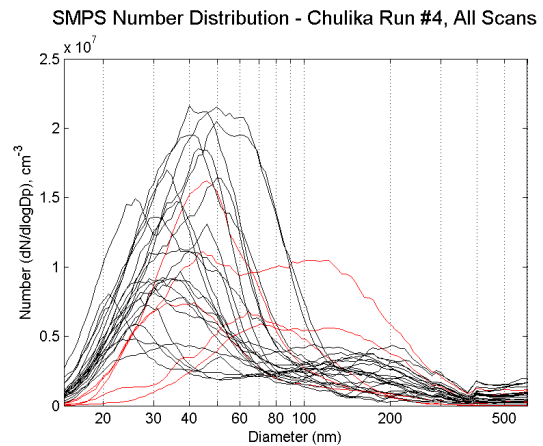
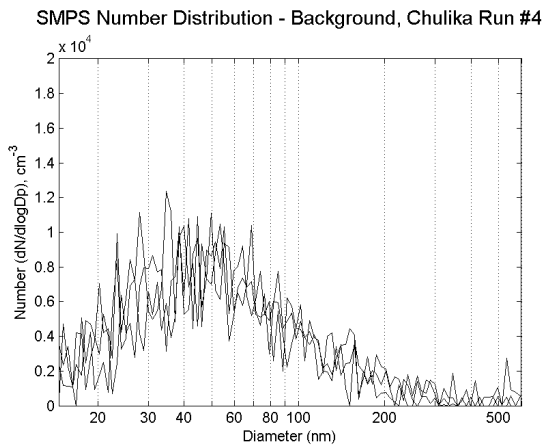
Red signifies scans during the “warm-up” period. Black “good” scans are random; there is no correlation between time and peak concentration.



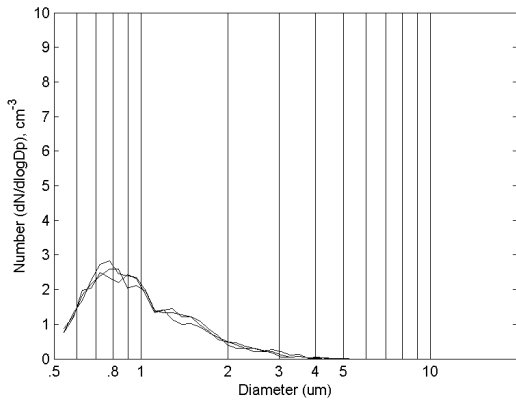
In the preceding set of plots, for the SMPS red indicates the first six runs after background (4-9). For the APS, red indicates the first six runs after background (4-9).



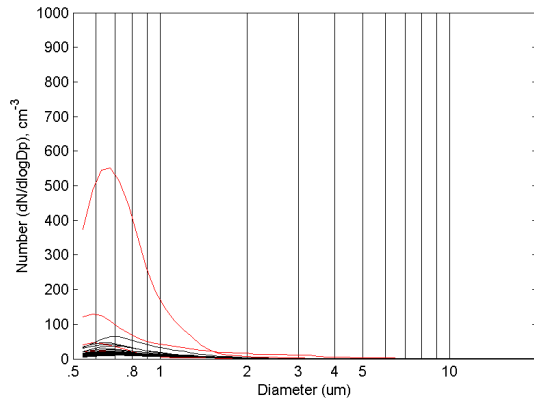
In the preceding set of plots, for the SMPS red indicates the first few runs after background (4-8). For the APS, red indicates the first six runs after background (4-8).



APS Number Distribution - Background, Chulika Run #4

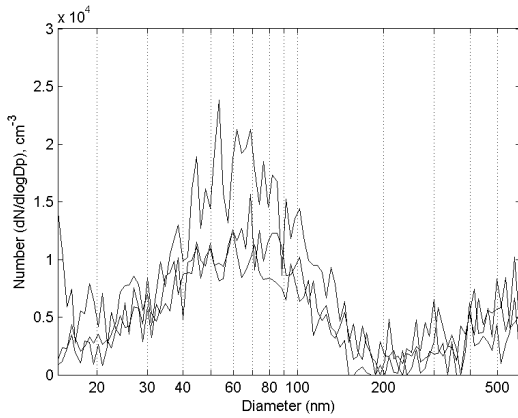


APS Number Distribution - Chulika Run #4, All Scans

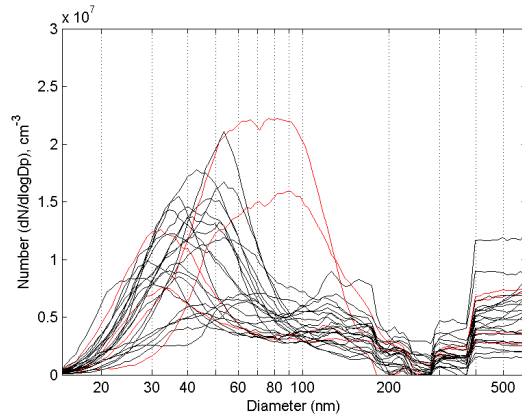


In the preceding set of plots, for the SMPS red indicates the first few runs after background (4-8). For the APS, red indicates the first six runs after background (4-7).

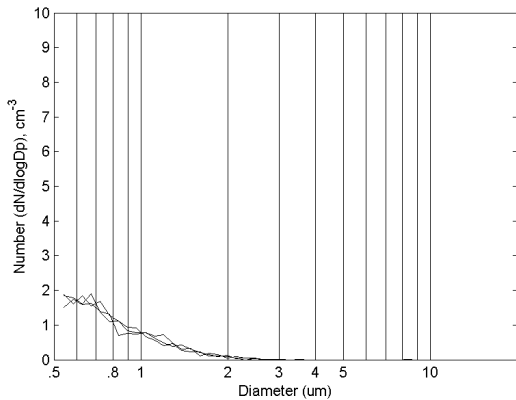
SMPS Number Distribution - Background, Chulika Run #6



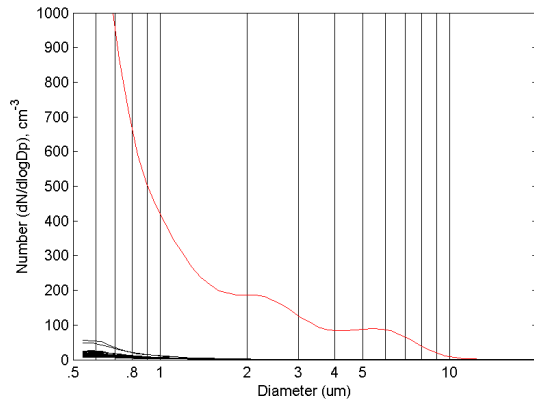
SMPS Number Distribution - Chulika Run #6, All Scans



APS Number Distribution - Background, Chulika Run #6



APS Number Distribution - Chulika Run #6, All Scans

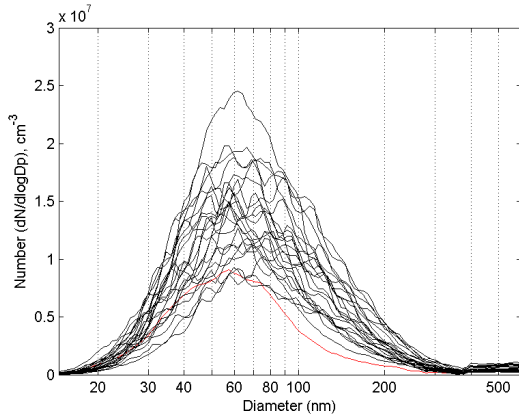


In the preceding set of plots, for the SMPS red indicates the first few runs after background (4-7). For the APS, red indicates the first six runs after background (4,5). As with Oorja Run #6, note the strange behaviour above ~300nm for SMPS. This occurred during runs 5 and 6 for all stoves, but most visibly for Chulika and the three-stone. The APS shows no notable spike in its measurement of sub-0.5 um particles, so this probably shouldn't be considered "real" data. Based largely on these "errors," test series 5 and 6 are excluded from most of the analysis.

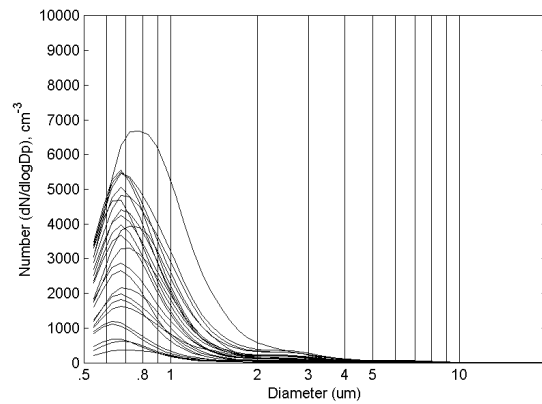
O.3 Three-stone fire

Background scans were not taken, as three-stone tests immediately followed Chulika testing. For all plots below, red signifies the first scan. For all subsequent (black) plots, there is no correlation between time and peak concentration.

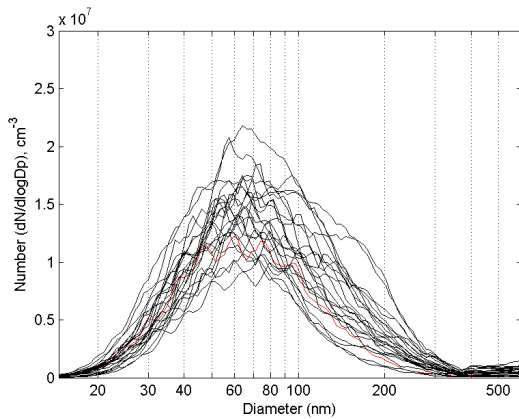
SMPS Number Distribution - 3-Stone Run #1, All Scans



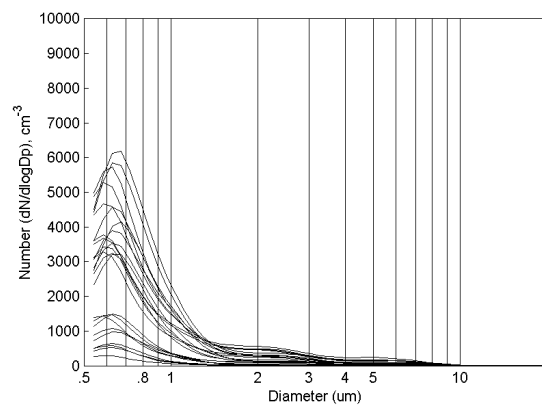
APS Number Distribution - 3-Stone Run #1, All Scans

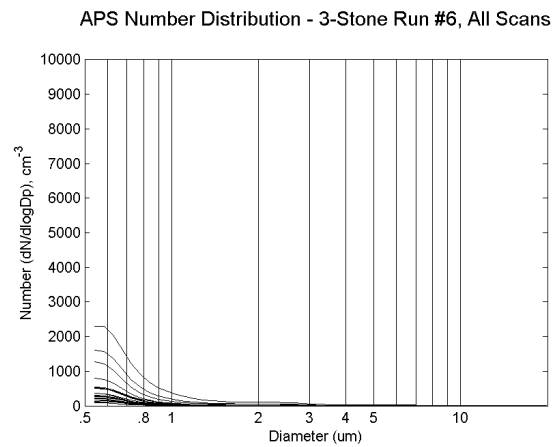
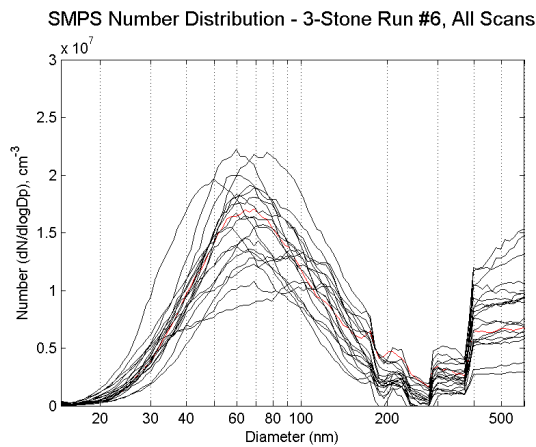
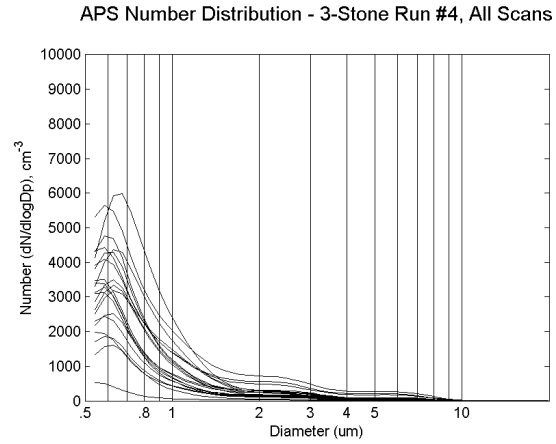
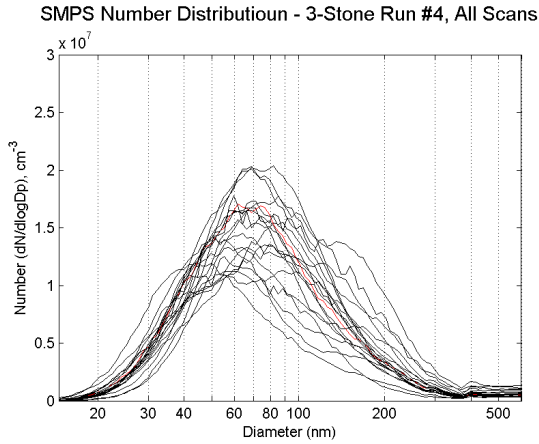


SMPS Number Distribution - 3-Stone Run #2, All Scans



APS Number Distribution - 3-Stone Run #2, All Scans





For APS runs 5 (not shown) and 6, APS intake was diluted at approximately 11:1; plot does not reflect this. As before, with runs 5 and 6, “strange” SMPS data exists above ~300 nm.

O.4 SMPS and APS “Good” Scans

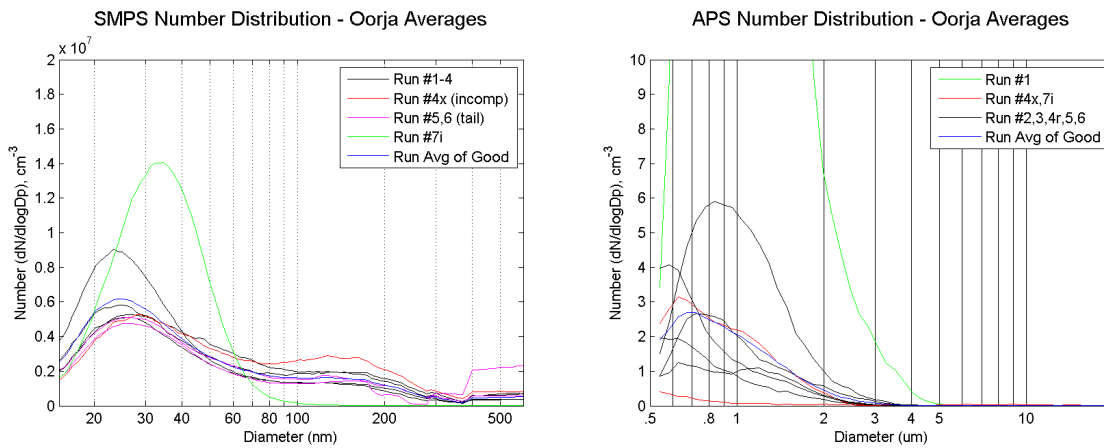
The next step was to pare the “early” and “late” scans from results, leaving the “good” ones that correspond to a steady flame condition. After this, average per-bin counts were determined for each test in order to get a single trace for each. These were summarized on a single graph for each of the three stove types (these in turn are later averaged across all tests for a given stove). Table 25 summarizes.

Table 25. Summary of SMPS / APS "good" scans

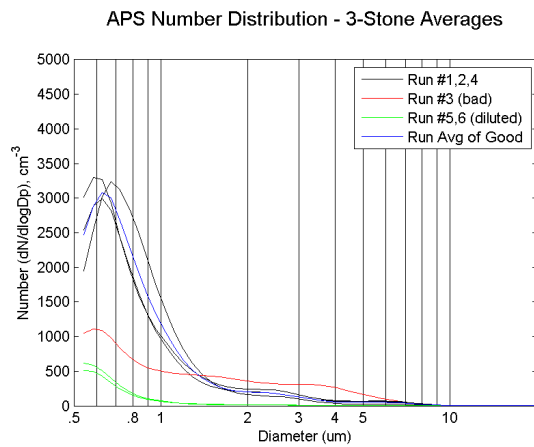
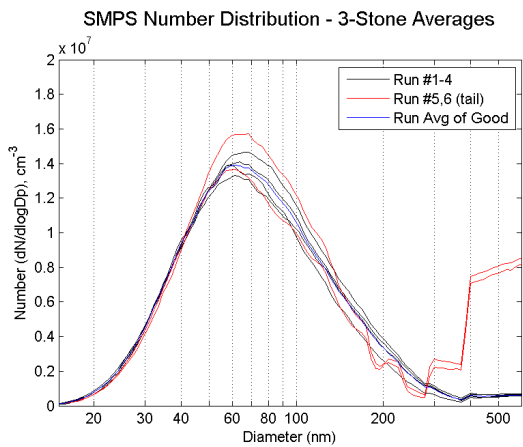
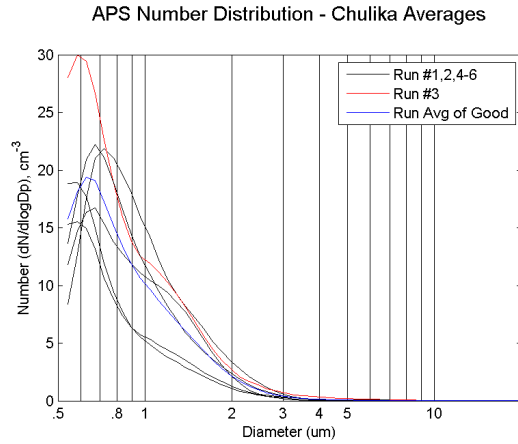
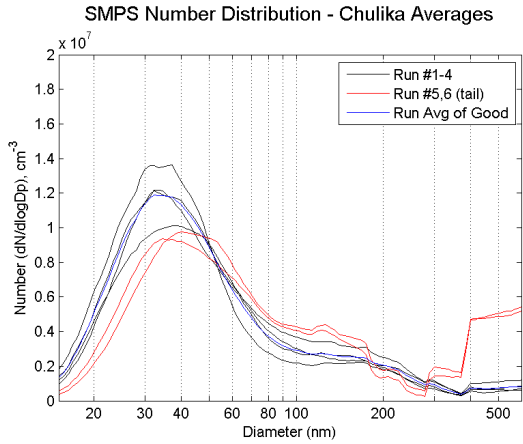
Run	Oorja APS	Oorja SMPS	Chulika APS	Chulika SMPS	3Stone APS	3Stone SMPS
1	11-16	6-16	10-33	10-32	1-24	1-24
2	6-16	6-16	9-30	9-30	1-24	1-24
3	6-16	6-16	7-27	7-27	1-20	1-20
4	6-19	6-19	8-30	8-30	1-20	1-20
5	6-19	5-19	6-27	7-27	1-19	1-19
6	6-18	6-18	6-28	8-28	1-20	1-20

Shaded boxes denote runs considered invalid.

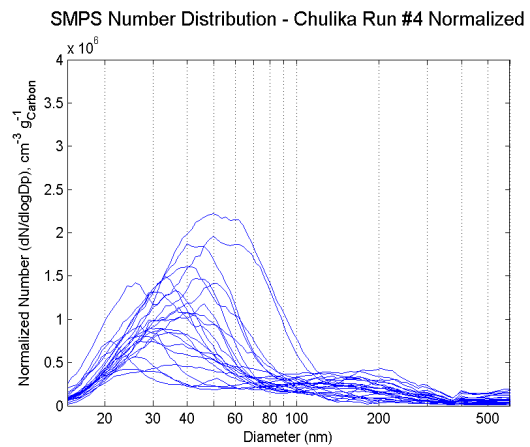
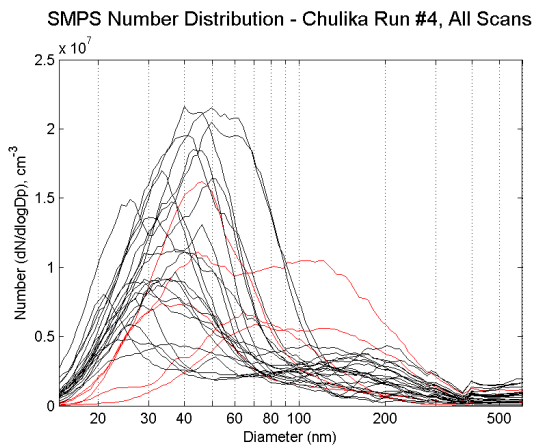
Ultimately, tests #1, 2, and 4 were selected for subsequent analysis based on complete and valid SMPS/APS data and problems with other instrumentation during tests #3, 5, and 6. Here, all "good" scans for all tests* are averaged on a per-bin basis to produce the following SMPS and APS plots.

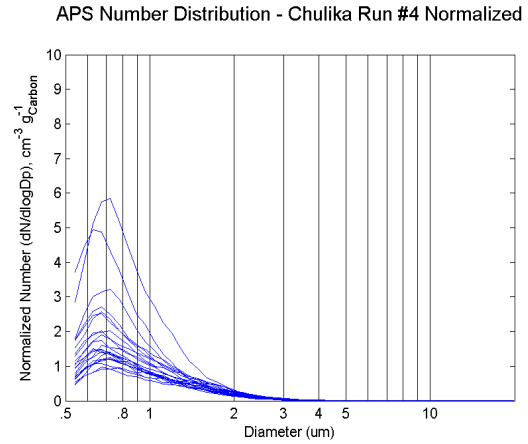
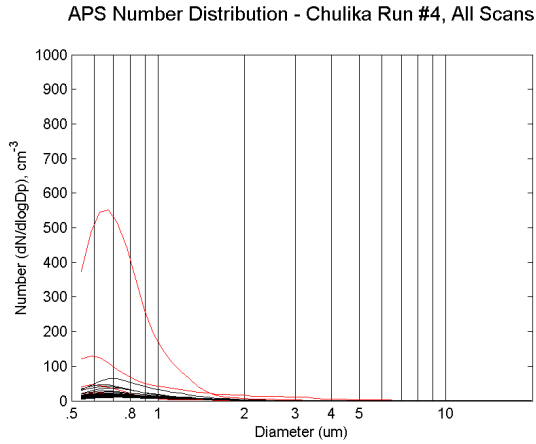


* Run 4x was an incomplete test for the Oorja stove only. Run7i used an alternate pellet source (Oorja only). Neither appears in subsequent analyses.

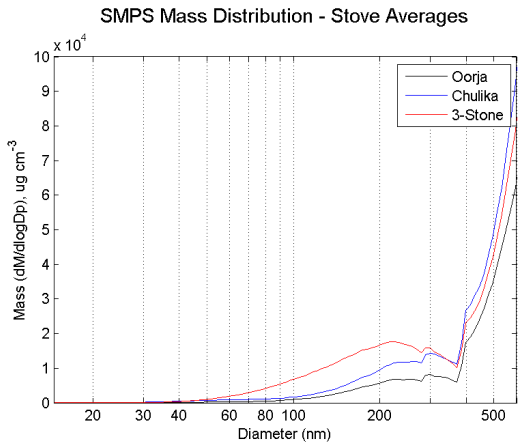


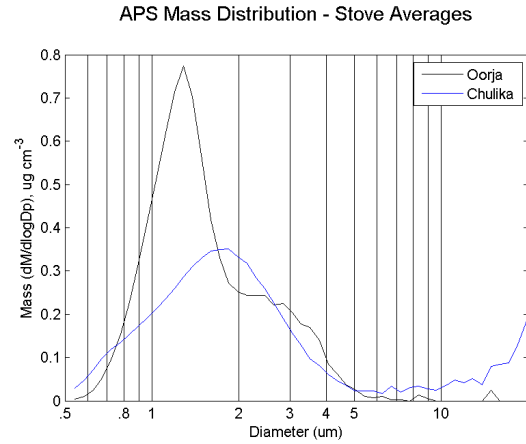
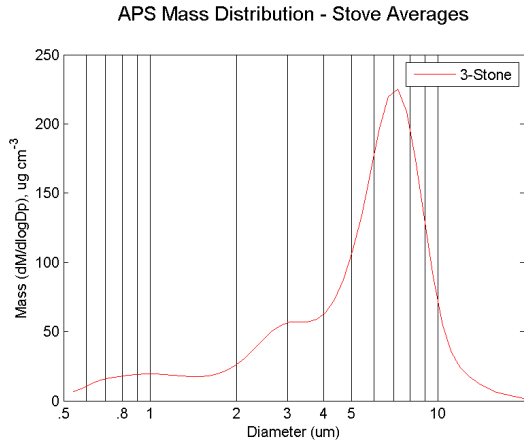
Scans were then normalized based on average carbon burn rate during each (135-second) scanning period. For brevity, only a single representative example is shown below. At left are reproductions of scans for Chulika test #4 from above; on the right are normalized plots that omit the pre-steady (red) data.





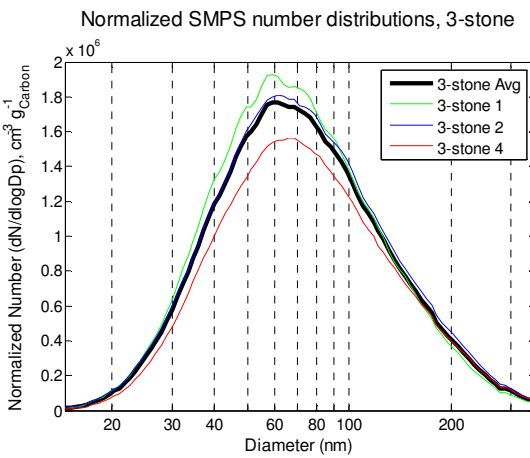
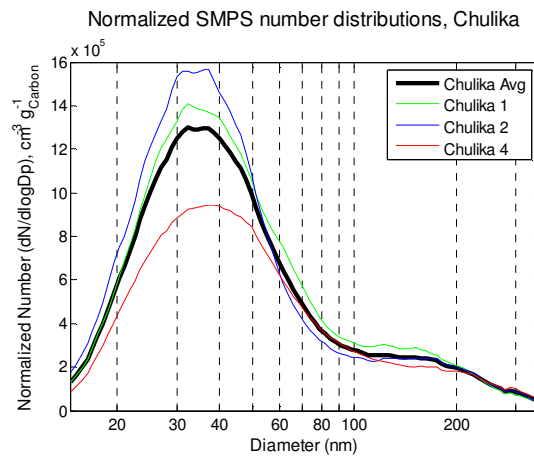
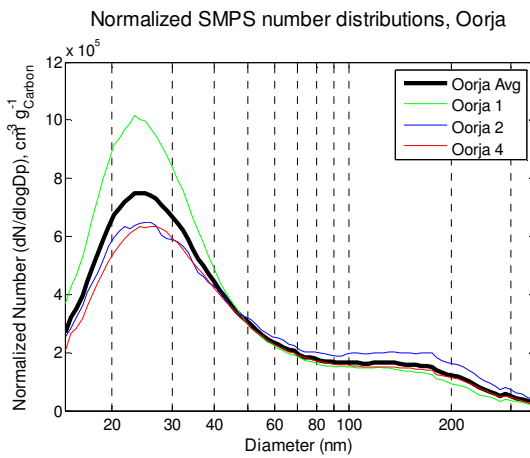
Normalized data across the valid tests is averaged and combined into plots that appear in the main body text. Distributions on a normalized mass basis were also investigated, but these were dominated by the > 300 nm artefact from the SMPS, even in tests #1, 2, and 4, where the artefact was close to negligible on a number distribution basis. Combining tests #1, 2, and 4 yields the following. The APS plots are separated into three-stone and Oorja / Chulika due to the large difference in y-scale.





O.5 Repeatability of SMPS scans

A breakdown of the tests that went into the creation of Figure 20(a) gives an idea of the repeatability between tests on a given cookstove. See below. Individual lines represent the averages of all “good” scans for a test.



Mode diameter is relatively consistent; the main difference between tests is amplitude (quantity of particles emitted).

Appendix P: Overview of combined SMPS / APS scans

Post-testing, it was discovered that the SMPS gave erroneous readings for larger particles due to an inability to reach higher voltages. The APS gives a single value for particle count in the $\sim 0.35\text{--}0.52\ \mu\text{m}$ range. This number helps to justify the exclusion of the suspect data from the SMPS. It is normalized and displayed on these plots as a point reference. The first two plots are reproduced from the text for convenience. The latter two show distributions based on mass. See Figure 42.

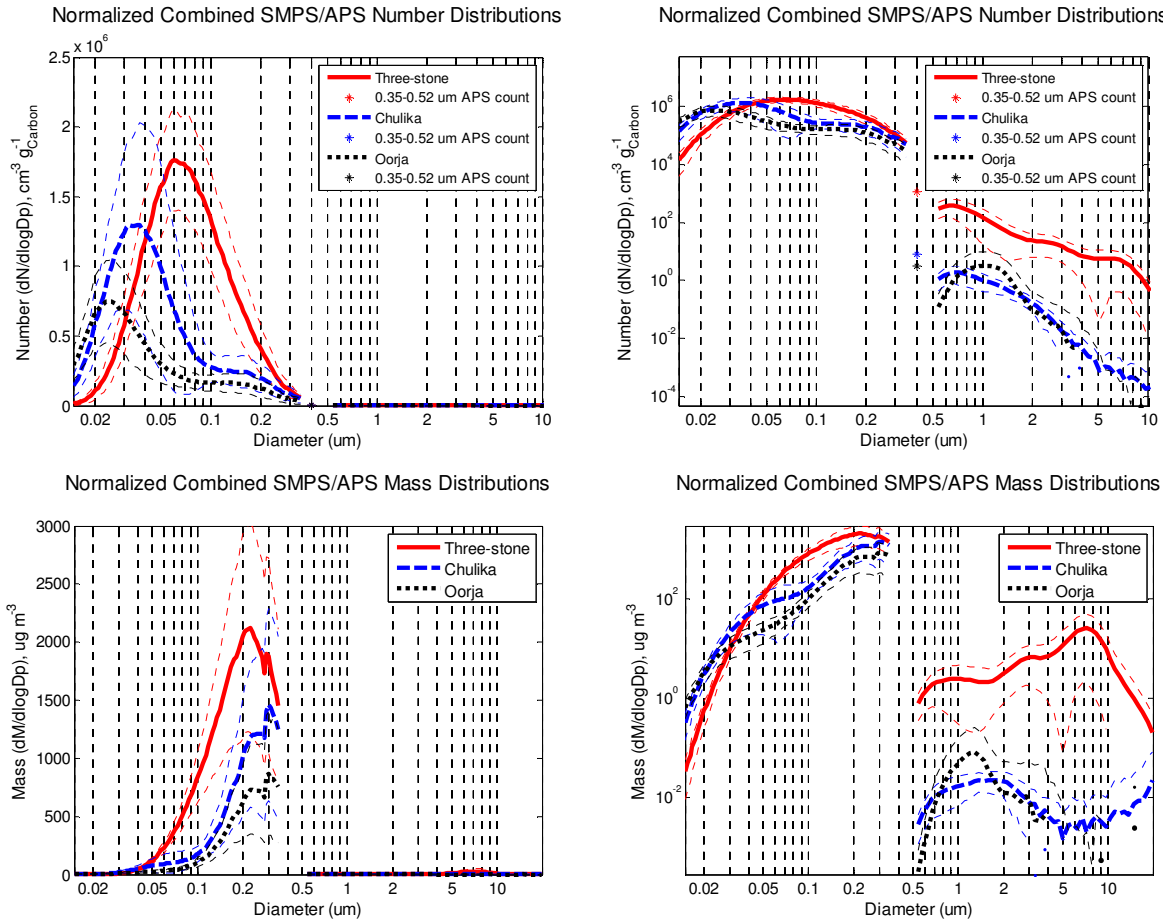


Figure 42. Normalized combined SMPS / APS distributions

Following the repair of the SMPS, another testing session occurred on 15 June 2012. As expected, the erroneous “tails” at larger diameters did not appear. An example of this erroneous data is copied from Appendix O alongside one of the follow-up tests (Figure 43).

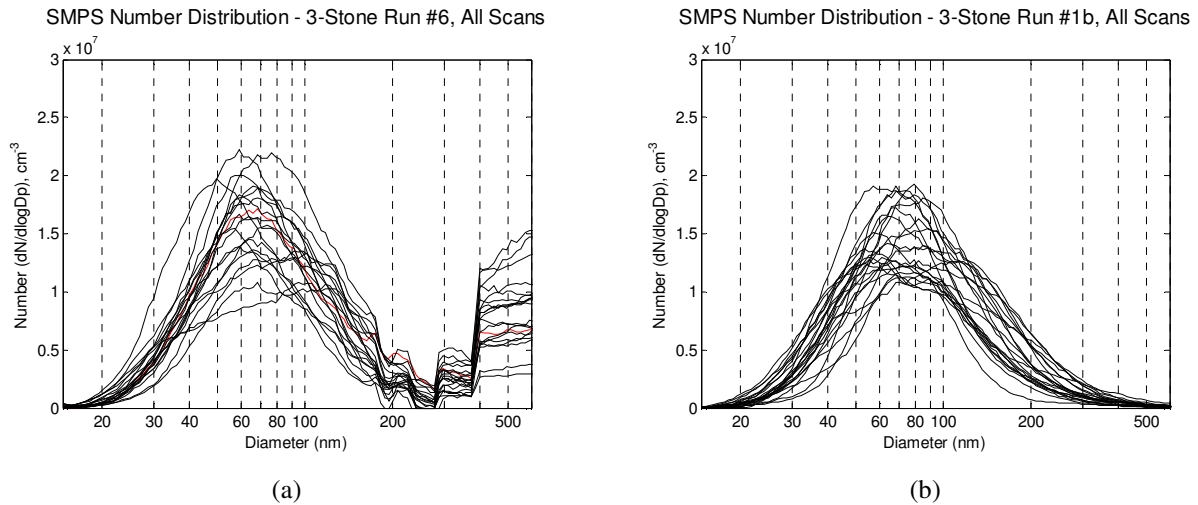


Figure 43. (a) Example of "bad" SMPS data, 3-stone test #6; (b) example of "good" SMPS data, 3-stone supplementary test #1b

A summary of results from the June 2012 testing is detailed in Figure 44. It shows general agreement with the trend noted on Figure 20(a), but no attempt is made to correlate data because a different wood supply (and moisture content) was used, the laboratory conditions were significantly different, etc. The black Oorja trace corresponds to "High" fan setting on the cookstove; during this set of tests, this setting dramatically affected size distribution. For further detail and discussion, see text and Appendix Q.

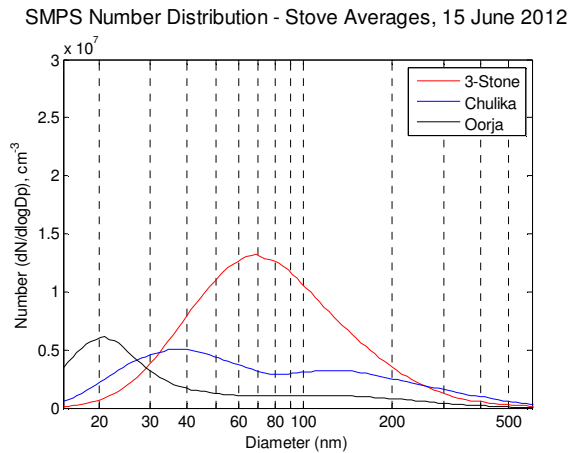


Figure 44. Averaged SMPS results (not normalized) from follow-up testing

Appendix Q: Investigation of Oorja operating modes

During the 15 June 2012 follow-up tests (see also Appendix P), the Low fan setting on the Oorja cookstove was used in accordance with the setting employed during the primary test series of March 2012. Likewise, an equivalent mass of pellets was used although they were from a different batch and moisture content was not tested. Environmental conditions in the (non-climate controlled) laboratory were also different (summer vs. winter).

During the first test, the flame was visibly lower than in previous tests; lower CO₂ emissions supported this observation. Interestingly, the SMPS traces from this period are shifted right (Figure 45(a)) compared to previous Oorja tests. The mode diameter is similar to that of the average of the three-stone fire. Additionally, PM mass emissions measured by the DustTrak are significantly higher than during the March 2012 tests.

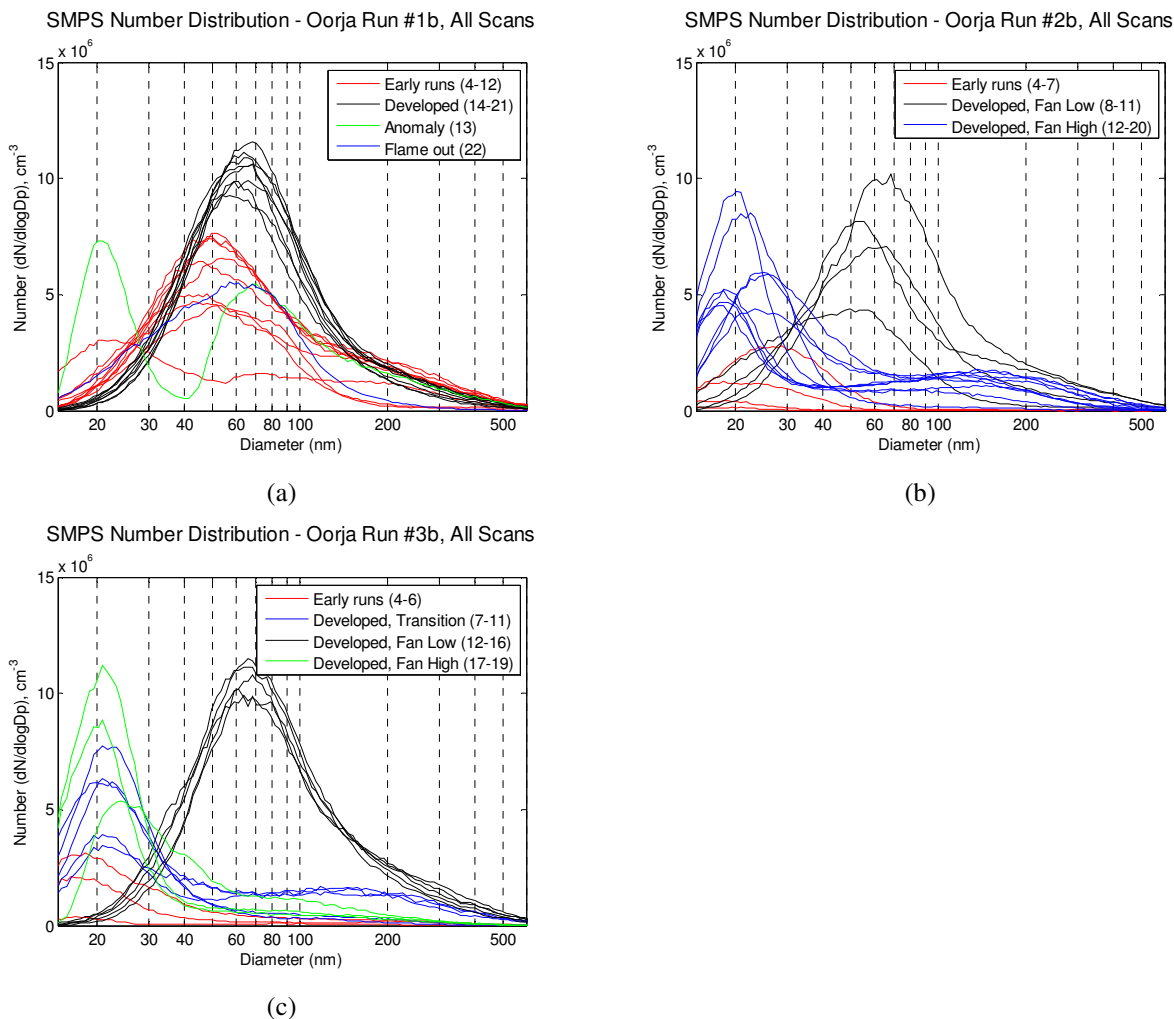


Figure 45. Oorja results from June 2012 follow-up tests

Partway through the next test (#2b), the fan setting was switched from Low to High. In a third test, the stove was started on High, switched to Low, and then turned back to High. Looking at Figure 45(b,c), the correlation between particle size distribution and fan setting is very clear.

Further study is warranted. Discrete operating conditions should be reproduced and emissions monitored in the same way as during the primary test series.

Appendix R: Overview of TEM imaging

R.1 Overview

TEM grids were collected for most test series; identification codes are indicated in Table 26. Collection time and averaged corrected DustTrak reading during collection time* are indicated in brackets and used for a comparative estimate of grid loading. Except where noted, pressure drop across the TPS was set to 1 psi corresponding to an estimated flow rate of 2.3 lpm. The number in bold is a “relative loading factor” normalized to the grid loading of Oorja Test 1 (D1) based on collection time, average corrected DustTrak reading, and TPS exhaust flow rate.

Table 26. TEM grid matrix

Stove	Test 1	Test 2	Test 4
Oorja	D1 [90s @ 2.01 mg/m ³] 1.00	B9 ^a [180s @ 0.49 mg/m ³] 0.48	B6 [90s @ 2.12 mg/m ³] 1.05
Chulika	D2 [45s @ 1.75 mg/m ³] 0.44	E1 [35s @ 7.29 mg/m ³] 1.41	B7 [60s @ 2.08 mg/m ³] 0.69
3-Stone	D4 ^b 30s @ 11.73 mg/m ³ 1.18	E3 ^c [10s @ 12.80 mg/m ³] 0.43	B8 [20s @ 9.57 mg/m ³] 1.06

^a The grid taken during Oorja test #2 (D5) was lost. In lieu of the desire to study three grids per stove type, grid B9 from test series #5 was used for the Oorja.

^b Second grid taken during this test because E1 (visually) appeared more heavily loaded than usual.

^c TPS pressure drop is 0.5 psi, yielding an estimated 1.4 lpm.

R.2 TEM imaging locations

For each grid, five locations were chosen for magnification and imaging. The first step was to roughly center the grid in the microscope and record the coordinates; this location was Point #1. Not recorded are the stagnation / impact regions near the grid center.[†] Other points are located relative to Point #1 as indicated in Table 27. If the carbon film is damaged in the region of interest, the nearest (intact) adjacent grid location was used.

Table 27. TEM imaging coordinates (in μm)

Point	Relative coordinates
1	(0, 0)
2	(+300, +300)
3	(-300, +300)
4	(-300, -300)
5	(+300, -300)

* Based on overall average gravimetric correction, not from the specific test in question.

[†] The center of the stagnation region is an alternate way to “set” the zero reference for Point #1. However, on some grids it is not obvious to locate and it is frequently the site of broken carbon film.

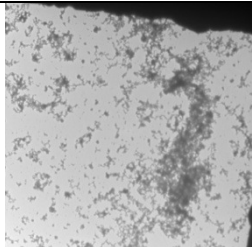
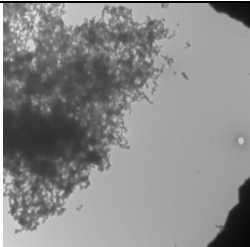
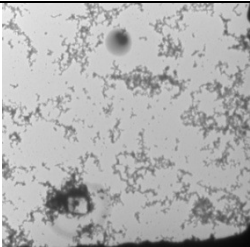
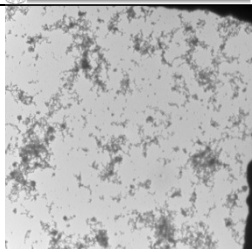
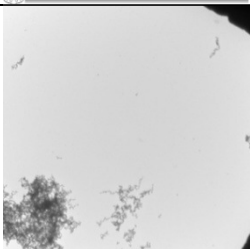
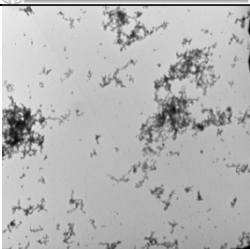
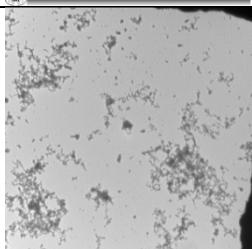
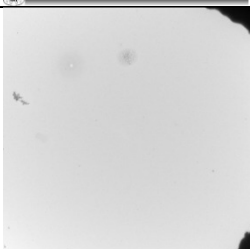
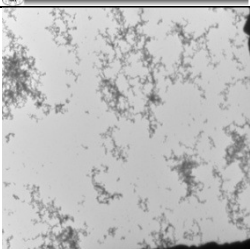

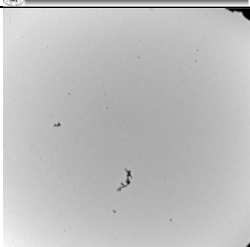
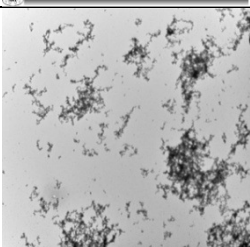
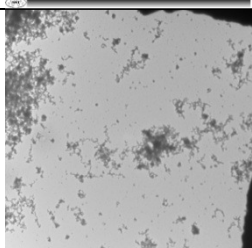
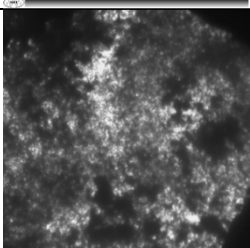
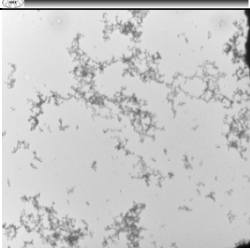
For each point, the nearest grid corner to the “right” (as viewed through the TEM camera, negative “x” in TEM coordinates) was located. The first image taken for each point (at lowest magnification, 15000x) shows a grid corner. Subsequent procedure is shown in Table 28.

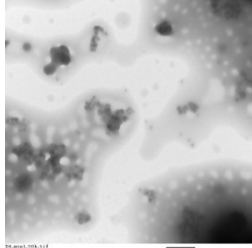
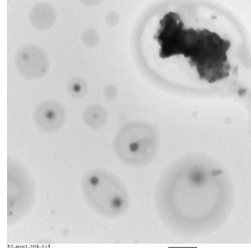
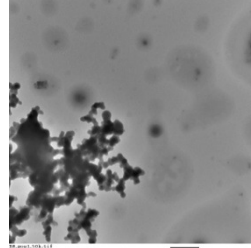
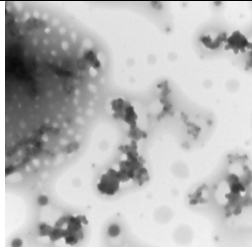
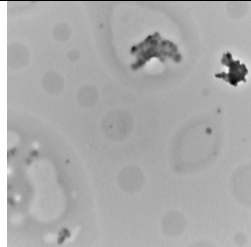
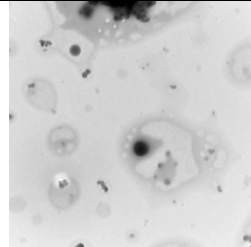
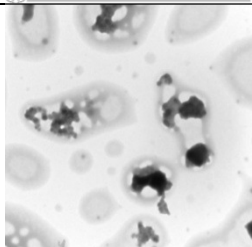
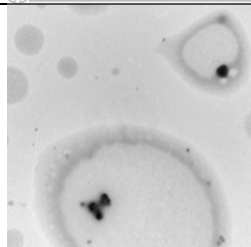
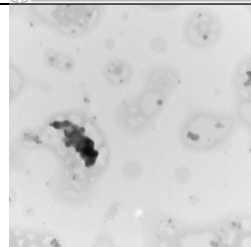
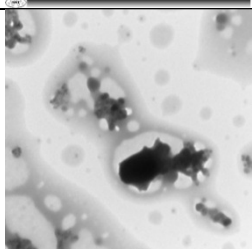
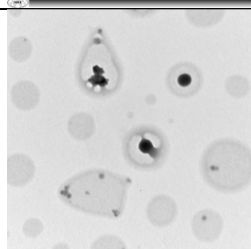
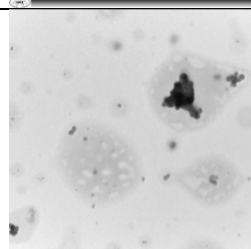
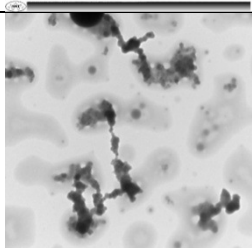
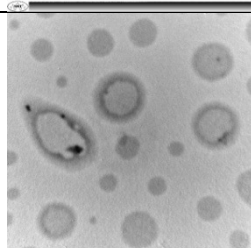
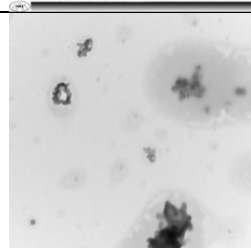
Table 28. TEM imaging steps

Step	Magnification	Procedure
1	15000 x	Move to center, record reference coordinates, record image of nearest grid corner to “right”
2	50000 x	Zoom in further, keep centered
3	150000 x	Focus on a region near the center that shows an agglomerate and adjacent smaller particles (if possible)
4	300000 x	Zoom in further, focusing on the region in Step 4
5	500000 x	Zoom in further (optional, doesn’t always provide useful information)

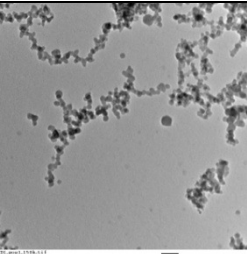
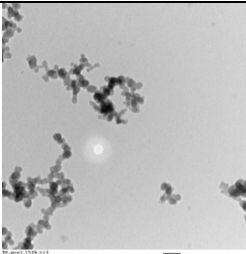
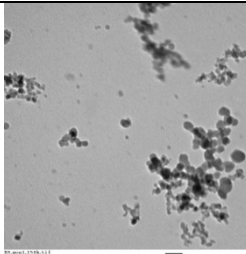
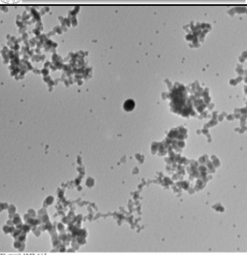

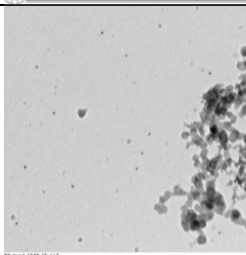
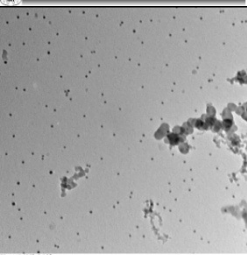
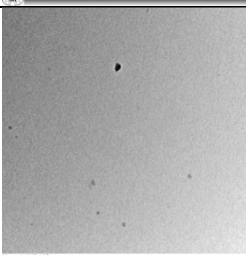
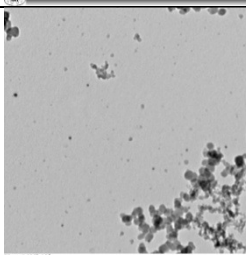
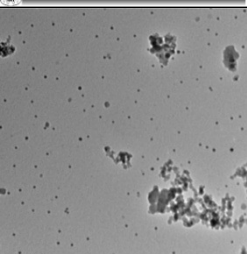
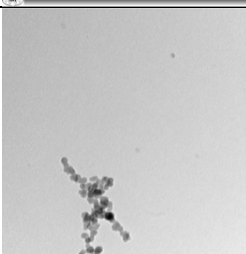
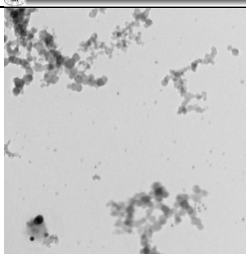
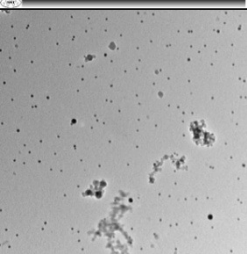
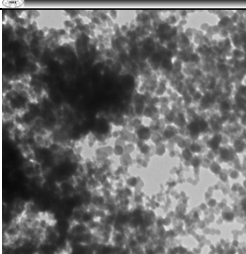
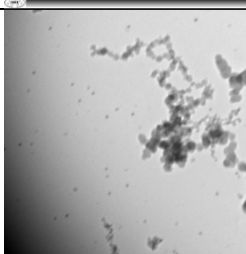
With only five imaging locations, counting is not done; rather, the goal was to look for trends and primary particle size between stove types.

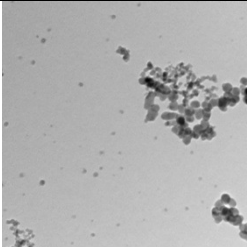
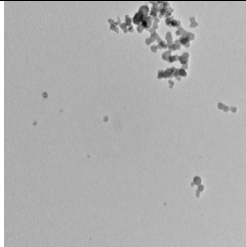
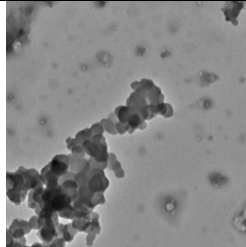
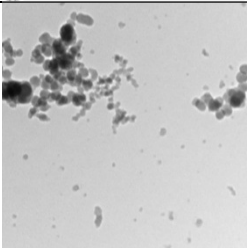
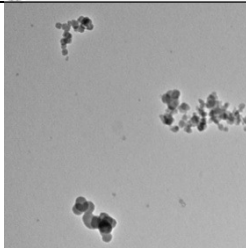
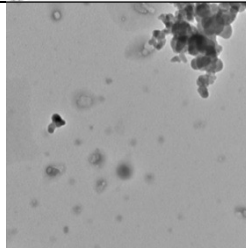
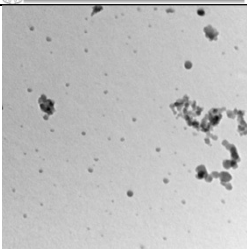
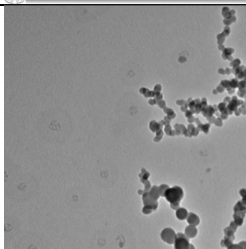
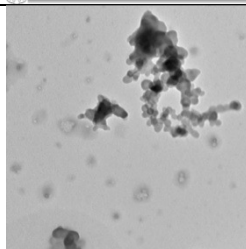
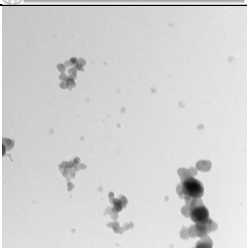
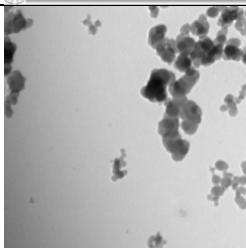
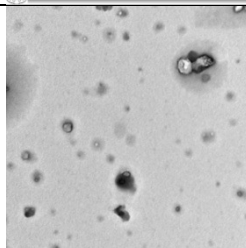
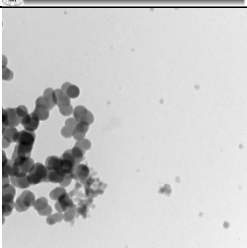
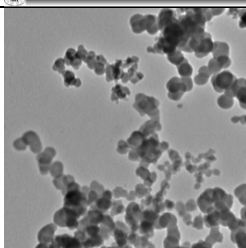
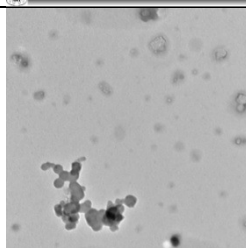
The following three pages show 15kx magnification. Oorja 1 appears to be more heavily loaded than Oorja 4 though points 1 and 5 for the latter show fairly dense agglomerates. At this level of magnification there does not appear to be a significant difference between the Oorja and Chulika particles. The three-stone is quite different, with each image showing what appear to be partially evaporated droplets that may be encasing the agglomerates.

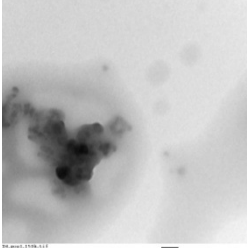
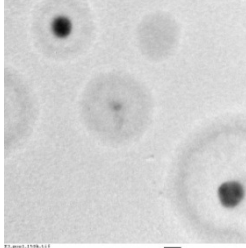
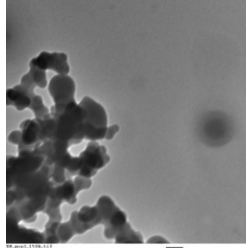
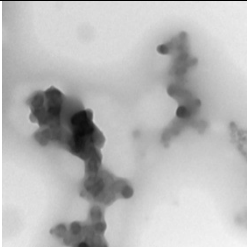
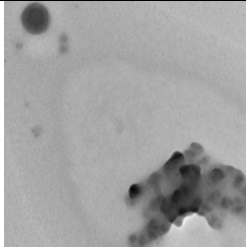
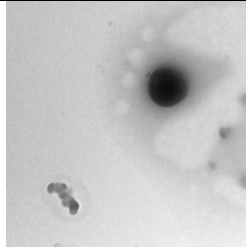
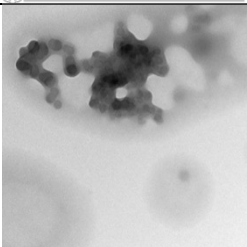
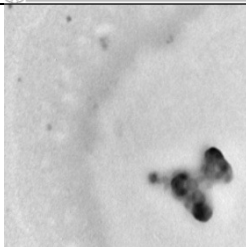
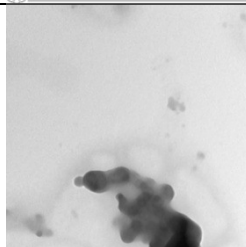
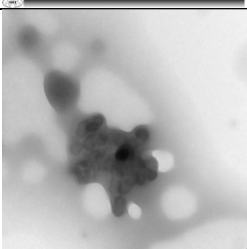

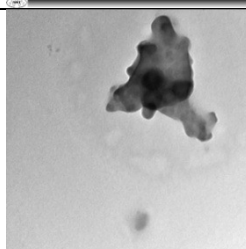
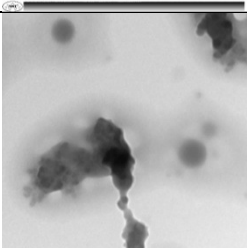
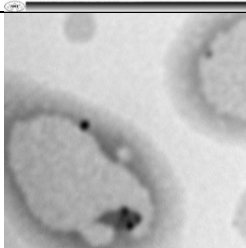
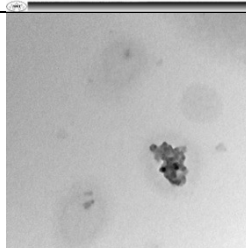
15kx magnification	Test 1 (D1)	Test 4 (B6)	Test 5 (B9)
Oorja point 1			
point 2			
point 3			
point 4			
point 5			

50kx magnification	Test 1 (D4)	Test 2 (E3)	Test 4 (B8)
3-Stone point 1	 <p> <small> Mx: 50kx, 1.000 x 10 mm 14.02.2018 14:15:12 DDP: Auto: 100.00% Microcomputer: 00.LanAust </small> </p>	 <p> <small> Mx: 50kx, 1.000 x 10 mm 14.02.2018 14:15:12 DDP: Auto: 100.00% Microcomputer: 00.LanAust </small> </p>	 <p> <small> Mx: 50kx, 1.000 x 10 mm 14.02.2018 14:15:12 DDP: Auto: 100.00% Microcomputer: 00.LanAust </small> </p>
point 2	 <p> <small> Mx: 50kx, 1.000 x 10 mm 14.02.2018 14:15:12 DDP: Auto: 100.00% Microcomputer: 00.LanAust </small> </p>	 <p> <small> Mx: 50kx, 1.000 x 10 mm 14.02.2018 14:15:12 DDP: Auto: 100.00% Microcomputer: 00.LanAust </small> </p>	 <p> <small> Mx: 50kx, 1.000 x 10 mm 14.02.2018 14:15:12 DDP: Auto: 100.00% Microcomputer: 00.LanAust </small> </p>
point 3	 <p> <small> Mx: 50kx, 1.000 x 10 mm 14.02.2018 14:15:12 DDP: Auto: 100.00% Microcomputer: 00.LanAust </small> </p>	 <p> <small> Mx: 50kx, 1.000 x 10 mm 14.02.2018 14:15:12 DDP: Auto: 100.00% Microcomputer: 00.LanAust </small> </p>	 <p> <small> Mx: 50kx, 1.000 x 10 mm 14.02.2018 14:15:12 DDP: Auto: 100.00% Microcomputer: 00.LanAust </small> </p>
point 4	 <p> <small> Mx: 50kx, 1.000 x 10 mm 14.02.2018 14:15:12 DDP: Auto: 100.00% Microcomputer: 00.LanAust </small> </p>	 <p> <small> Mx: 50kx, 1.000 x 10 mm 14.02.2018 14:15:12 DDP: Auto: 100.00% Microcomputer: 00.LanAust </small> </p>	 <p> <small> Mx: 50kx, 1.000 x 10 mm 14.02.2018 14:15:12 DDP: Auto: 100.00% Microcomputer: 00.LanAust </small> </p>
point 5	 <p> <small> Mx: 50kx, 1.000 x 10 mm 14.02.2018 14:15:12 DDP: Auto: 100.00% Microcomputer: 00.LanAust </small> </p>	 <p> <small> Mx: 50kx, 1.000 x 10 mm 14.02.2018 14:15:12 DDP: Auto: 100.00% Microcomputer: 00.LanAust </small> </p>	 <p> <small> Mx: 50kx, 1.000 x 10 mm 14.02.2018 14:15:12 DDP: Auto: 100.00% Microcomputer: 00.LanAust </small> </p>

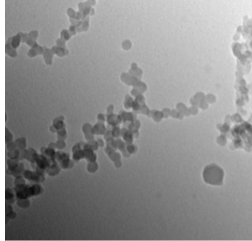
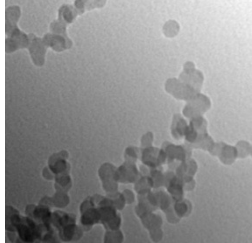
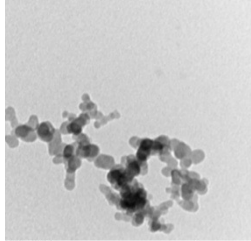
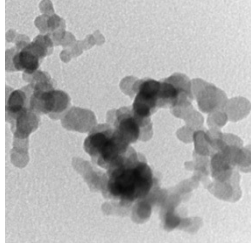
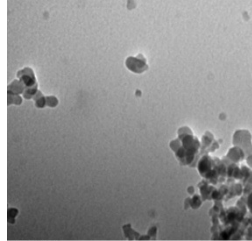
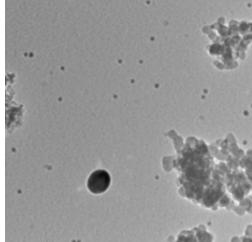
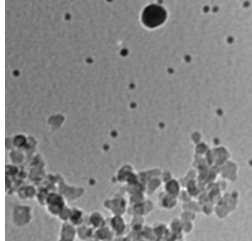
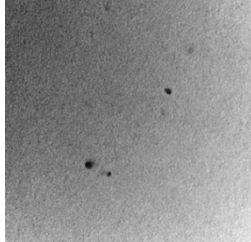
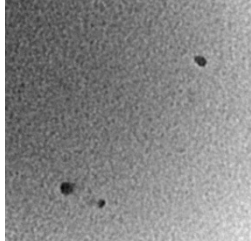
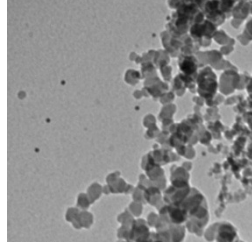
The following three pages step up to 150kx magnification. At this magnification, more details emerge. The Oorja images have large quantities of very small black particles and scattered amorphous chains in which primary particle constituents seem to be visible. The Chulika primary particles seem slightly larger, with no significant differences in agglomerates. Few standalone primary particles are visible in the three-stone images.

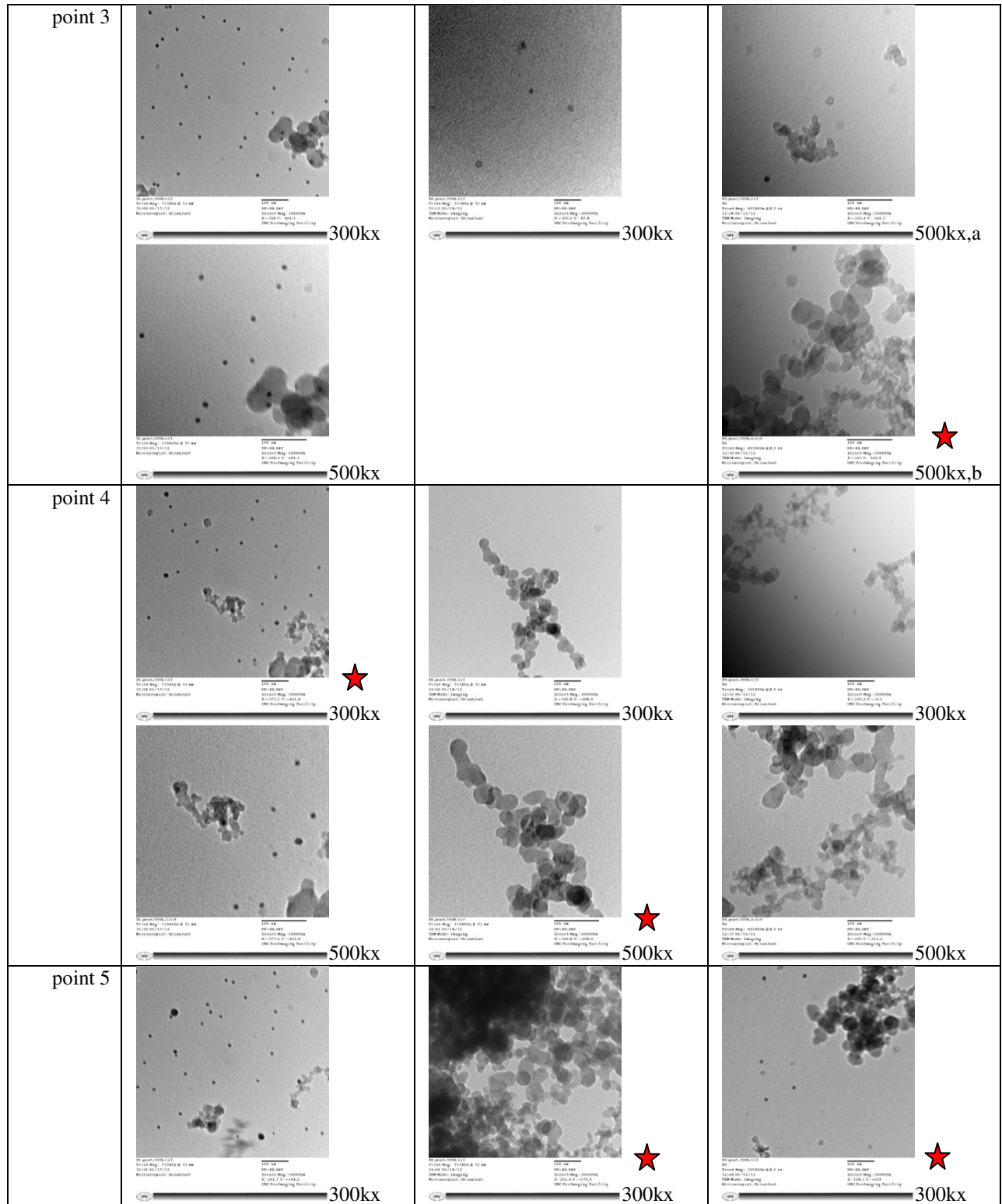
150kx magnification	Test 1 (D1)	Test 4 (B6)	Test 5 (B9)
Oorja point 1	 <p>Micrograph showing a network of dark, interconnected particles, likely primary particles or agglomerates, against a light background.</p>	 <p>Micrograph showing a network of dark, interconnected particles, likely primary particles or agglomerates, against a light background.</p>	 <p>Micrograph showing a network of dark, interconnected particles, likely primary particles or agglomerates, against a light background.</p>
point 2	 <p>Micrograph showing a network of dark, interconnected particles, likely primary particles or agglomerates, against a light background.</p>	 <p>Micrograph showing a network of dark, interconnected particles, likely primary particles or agglomerates, against a light background.</p>	 <p>Micrograph showing a network of dark, interconnected particles, likely primary particles or agglomerates, against a light background.</p>
point 3	 <p>Micrograph showing a network of dark, interconnected particles, likely primary particles or agglomerates, against a light background.</p>	 <p>Micrograph showing a network of dark, interconnected particles, likely primary particles or agglomerates, against a light background.</p>	 <p>Micrograph showing a network of dark, interconnected particles, likely primary particles or agglomerates, against a light background.</p>
point 4	 <p>Micrograph showing a network of dark, interconnected particles, likely primary particles or agglomerates, against a light background.</p>	 <p>Micrograph showing a network of dark, interconnected particles, likely primary particles or agglomerates, against a light background.</p>	 <p>Micrograph showing a network of dark, interconnected particles, likely primary particles or agglomerates, against a light background.</p>
point 5	 <p>Micrograph showing a network of dark, interconnected particles, likely primary particles or agglomerates, against a light background.</p>	 <p>Micrograph showing a network of dark, interconnected particles, likely primary particles or agglomerates, against a light background.</p>	 <p>Micrograph showing a network of dark, interconnected particles, likely primary particles or agglomerates, against a light background.</p>

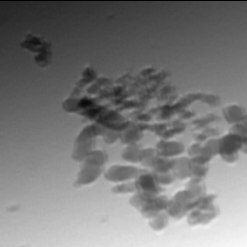
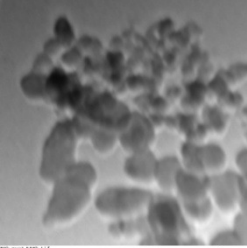
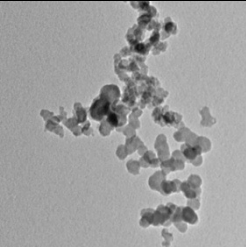
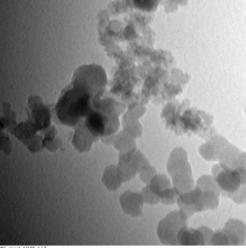
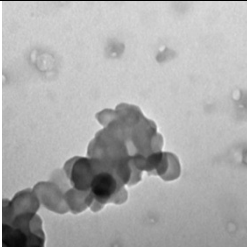
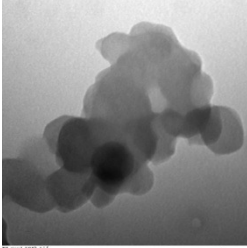
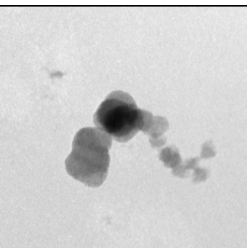
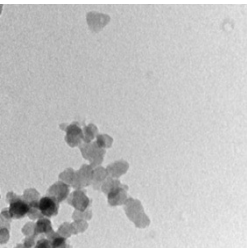
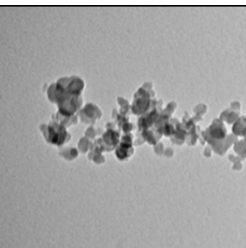
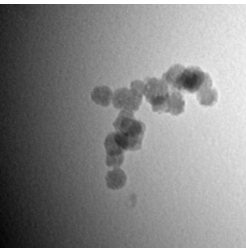
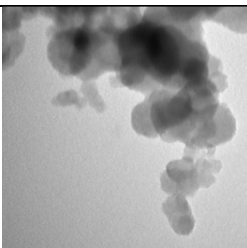
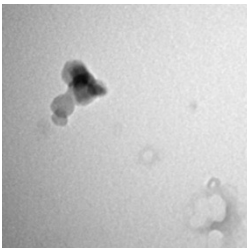
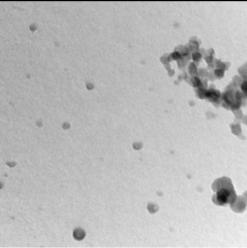
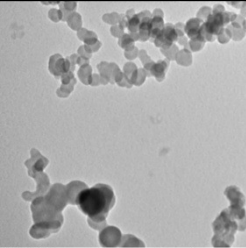
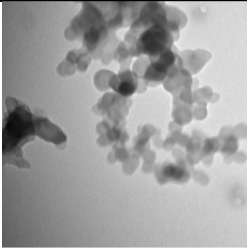
150kx magnification	Test 1 (D2)	Test 2 (E1)	Test 4 (B7)
Chulika point 1	 <p>Micrograph showing a cluster of dark, irregular particles (likely spores or debris) against a light background. The particles are concentrated in the upper right quadrant.</p>	 <p>Micrograph showing a cluster of dark, irregular particles (likely spores or debris) against a light background. The particles are concentrated in the upper right quadrant.</p>	 <p>Micrograph showing a cluster of dark, irregular particles (likely spores or debris) against a light background. The particles are concentrated in the upper right quadrant.</p>
point 2	 <p>Micrograph showing a cluster of dark, irregular particles (likely spores or debris) against a light background. The particles are concentrated in the upper left quadrant.</p>	 <p>Micrograph showing a cluster of dark, irregular particles (likely spores or debris) against a light background. The particles are concentrated in the upper right quadrant.</p>	 <p>Micrograph showing a cluster of dark, irregular particles (likely spores or debris) against a light background. The particles are concentrated in the upper right quadrant.</p>
point 3	 <p>Micrograph showing a cluster of dark, irregular particles (likely spores or debris) against a light background. The particles are concentrated in the upper right quadrant.</p>	 <p>Micrograph showing a cluster of dark, irregular particles (likely spores or debris) against a light background. The particles are concentrated in the upper right quadrant.</p>	 <p>Micrograph showing a cluster of dark, irregular particles (likely spores or debris) against a light background. The particles are concentrated in the upper right quadrant.</p>
point 4	 <p>Micrograph showing a cluster of dark, irregular particles (likely spores or debris) against a light background. The particles are concentrated in the lower right quadrant.</p>	 <p>Micrograph showing a cluster of dark, irregular particles (likely spores or debris) against a light background. The particles are concentrated in the upper right quadrant.</p>	 <p>Micrograph showing a cluster of dark, irregular particles (likely spores or debris) against a light background. The particles are concentrated in the upper right quadrant.</p>
point 5	 <p>Micrograph showing a cluster of dark, irregular particles (likely spores or debris) against a light background. The particles are concentrated in the lower left quadrant.</p>	 <p>Micrograph showing a cluster of dark, irregular particles (likely spores or debris) against a light background. The particles are concentrated in the upper right quadrant.</p>	 <p>Micrograph showing a cluster of dark, irregular particles (likely spores or debris) against a light background. The particles are concentrated in the upper right quadrant.</p>

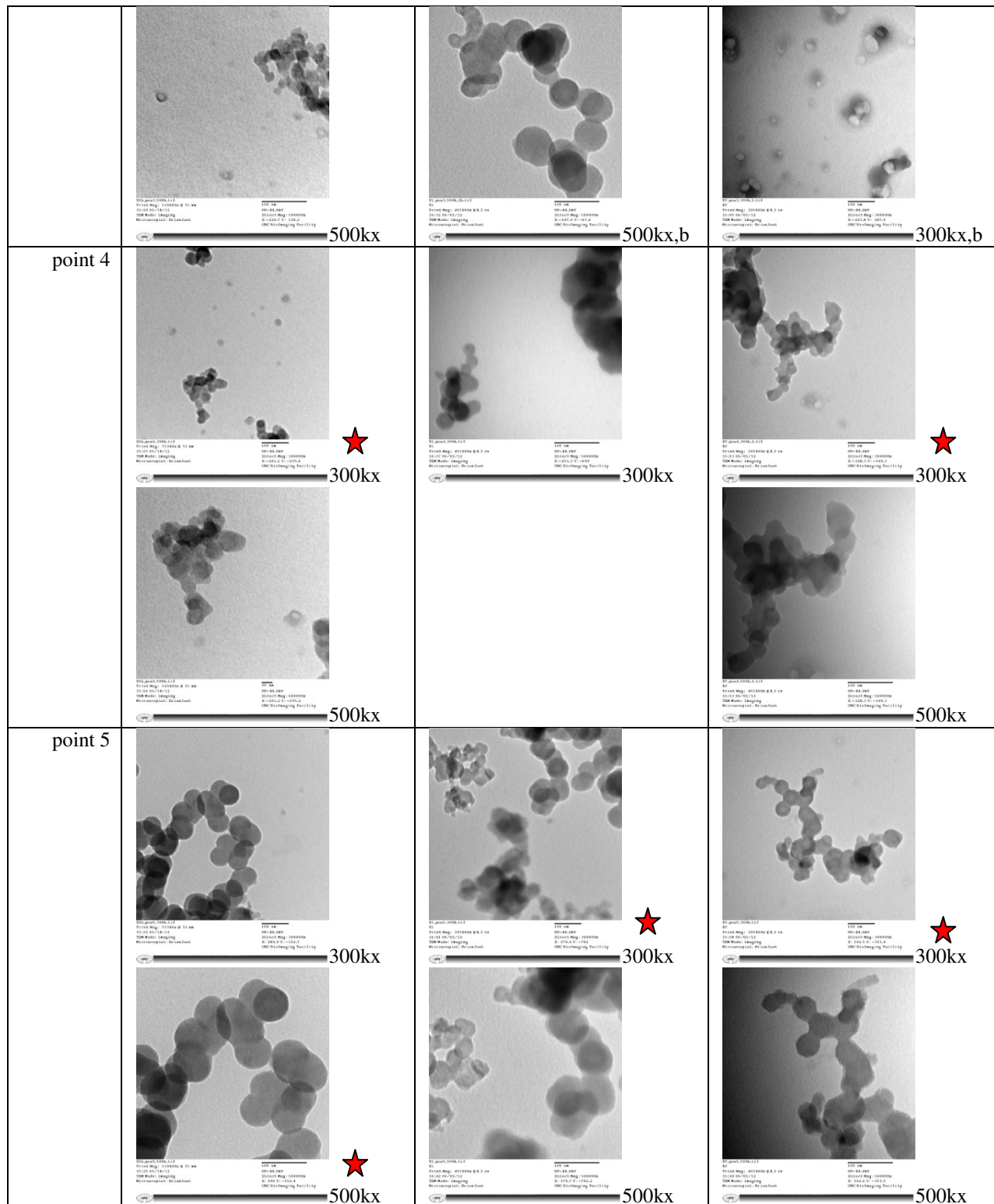
150kx magnification	Test 1 (D4)	Test 2 (E3)	Test 4 (B8)
3-Stone point 1	 <p> <small> Mx: 400x, Y: 100.0 Fx: 100.0, Y: 100.0 Z: 100.0, Y: 100.0 Microscopist: Dr. Jankovic Date: 2014-07-10 File: 2014-07-10-100000 </small> </p>	 <p> <small> Mx: 400x, Y: 100.0 Fx: 100.0, Y: 100.0 Z: 100.0, Y: 100.0 Microscopist: Dr. Jankovic Date: 2014-07-10 File: 2014-07-10-100000 </small> </p>	 <p> <small> Mx: 400x, Y: 100.0 Fx: 100.0, Y: 100.0 Z: 100.0, Y: 100.0 Microscopist: Dr. Jankovic Date: 2014-07-10 File: 2014-07-10-100000 </small> </p>
point 2	 <p> <small> Mx: 400x, Y: 100.0 Fx: 100.0, Y: 100.0 Z: 100.0, Y: 100.0 Microscopist: Dr. Jankovic Date: 2014-07-10 File: 2014-07-10-100000 </small> </p>	 <p> <small> Mx: 400x, Y: 100.0 Fx: 100.0, Y: 100.0 Z: 100.0, Y: 100.0 Microscopist: Dr. Jankovic Date: 2014-07-10 File: 2014-07-10-100000 </small> </p>	 <p> <small> Mx: 400x, Y: 100.0 Fx: 100.0, Y: 100.0 Z: 100.0, Y: 100.0 Microscopist: Dr. Jankovic Date: 2014-07-10 File: 2014-07-10-100000 </small> </p>
point 3	 <p> <small> Mx: 400x, Y: 100.0 Fx: 100.0, Y: 100.0 Z: 100.0, Y: 100.0 Microscopist: Dr. Jankovic Date: 2014-07-10 File: 2014-07-10-100000 </small> </p>	 <p> <small> Mx: 400x, Y: 100.0 Fx: 100.0, Y: 100.0 Z: 100.0, Y: 100.0 Microscopist: Dr. Jankovic Date: 2014-07-10 File: 2014-07-10-100000 </small> </p>	 <p> <small> Mx: 400x, Y: 100.0 Fx: 100.0, Y: 100.0 Z: 100.0, Y: 100.0 Microscopist: Dr. Jankovic Date: 2014-07-10 File: 2014-07-10-100000 </small> </p>
point 4	 <p> <small> Mx: 400x, Y: 100.0 Fx: 100.0, Y: 100.0 Z: 100.0, Y: 100.0 Microscopist: Dr. Jankovic Date: 2014-07-10 File: 2014-07-10-100000 </small> </p>	 <p> <small> Mx: 400x, Y: 100.0 Fx: 100.0, Y: 100.0 Z: 100.0, Y: 100.0 Microscopist: Dr. Jankovic Date: 2014-07-10 File: 2014-07-10-100000 </small> </p>	 <p> <small> Mx: 400x, Y: 100.0 Fx: 100.0, Y: 100.0 Z: 100.0, Y: 100.0 Microscopist: Dr. Jankovic Date: 2014-07-10 File: 2014-07-10-100000 </small> </p>
point 5	 <p> <small> Mx: 400x, Y: 100.0 Fx: 100.0, Y: 100.0 Z: 100.0, Y: 100.0 Microscopist: Dr. Jankovic Date: 2014-07-10 File: 2014-07-10-100000 </small> </p>	 <p> <small> Mx: 400x, Y: 100.0 Fx: 100.0, Y: 100.0 Z: 100.0, Y: 100.0 Microscopist: Dr. Jankovic Date: 2014-07-10 File: 2014-07-10-100000 </small> </p>	 <p> <small> Mx: 400x, Y: 100.0 Fx: 100.0, Y: 100.0 Z: 100.0, Y: 100.0 Microscopist: Dr. Jankovic Date: 2014-07-10 File: 2014-07-10-100000 </small> </p>

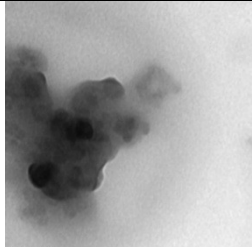

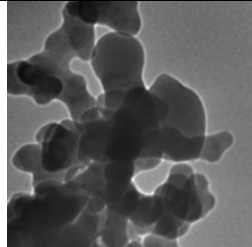
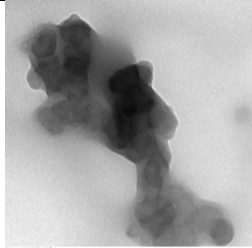
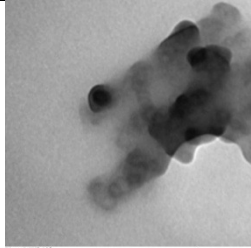
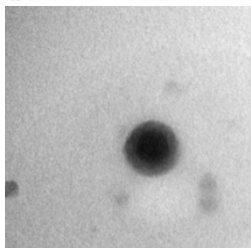
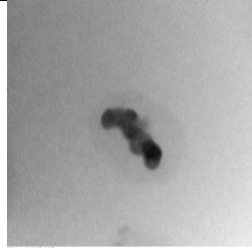
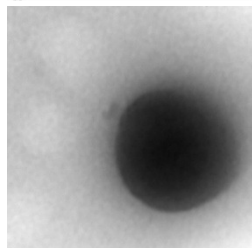
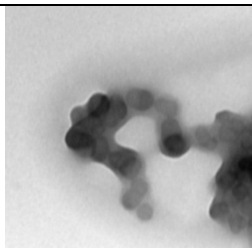
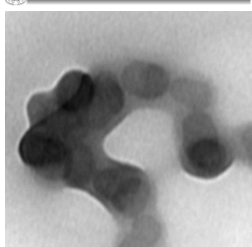
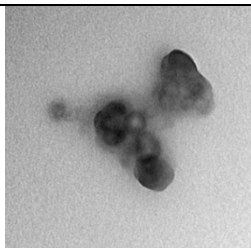
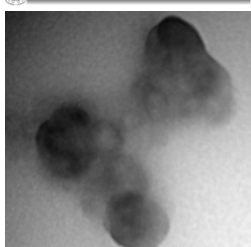
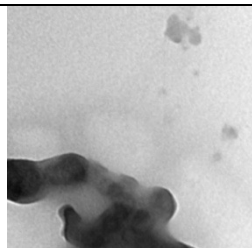
On the following pages, magnification is at 300000x and/or 500000x. In some cases, more than one region from the 150000x image was investigated; these are indicated by (a) and (b) labels. At this point, manual measurements of images can yield approximate particle size in agglomerates, although three-stone primary particles are sometimes hard to discern and there is significant variability in size. Starred images were measured / analyzed; refer to Appendix R.

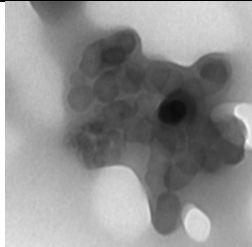
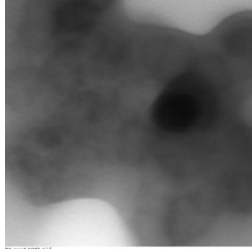
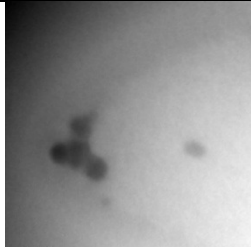

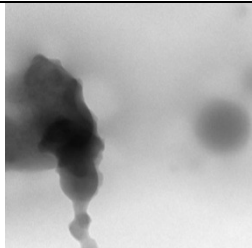
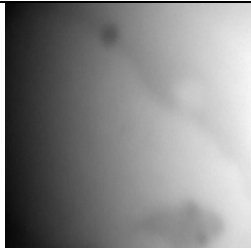
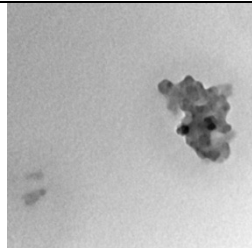
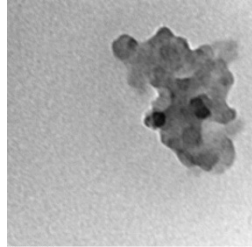
300/500kx mag.	Test 1 (D1)	Test 4 (B6)	Test 5 (B9)
Oorja point 1	 <p data-bbox="337 667 586 709">300kx</p>  <p data-bbox="337 970 586 1012">500kx</p>	 <p data-bbox="711 667 959 709">300kx</p>  <p data-bbox="711 970 959 1012">500kx</p>	 <p data-bbox="1084 667 1333 709">300kx</p>
point 2	 <p data-bbox="337 1281 586 1323">300kx</p>  <p data-bbox="337 1583 586 1625">500kx</p>	 <p data-bbox="711 1281 959 1323">300kx</p>  <p data-bbox="711 1583 959 1625">500kx</p>	 <p data-bbox="1084 1281 1333 1323">300kx</p>



300/500kx mag.	Test 1 (D2)	Test 2 (E1)	Test 4 (B7)
Chulika point 1	 <p>300kx</p>  <p>500kx</p>	 <p>300kx</p>  <p>500kx</p>	 <p>300kx</p>  <p>500kx</p>
point 2	 <p>500kx,a</p>  <p>500kx,b</p>	 <p>300kx,a</p>  <p>500kx,b</p>	 <p>500kx,a</p>  <p>500kx,b</p>
point 3	 <p>300kx</p>	 <p>300kx</p>	 <p>300kx,a</p>

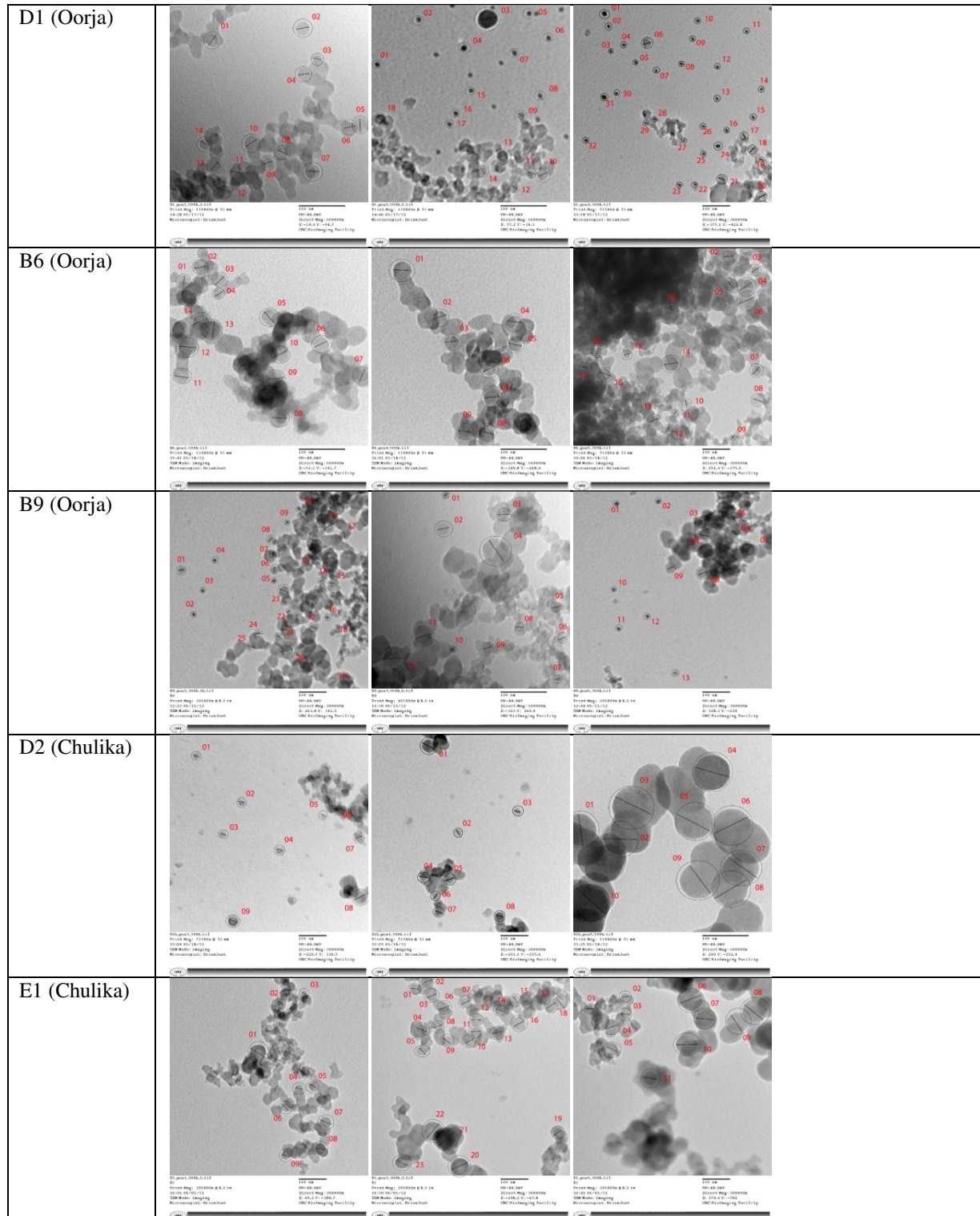


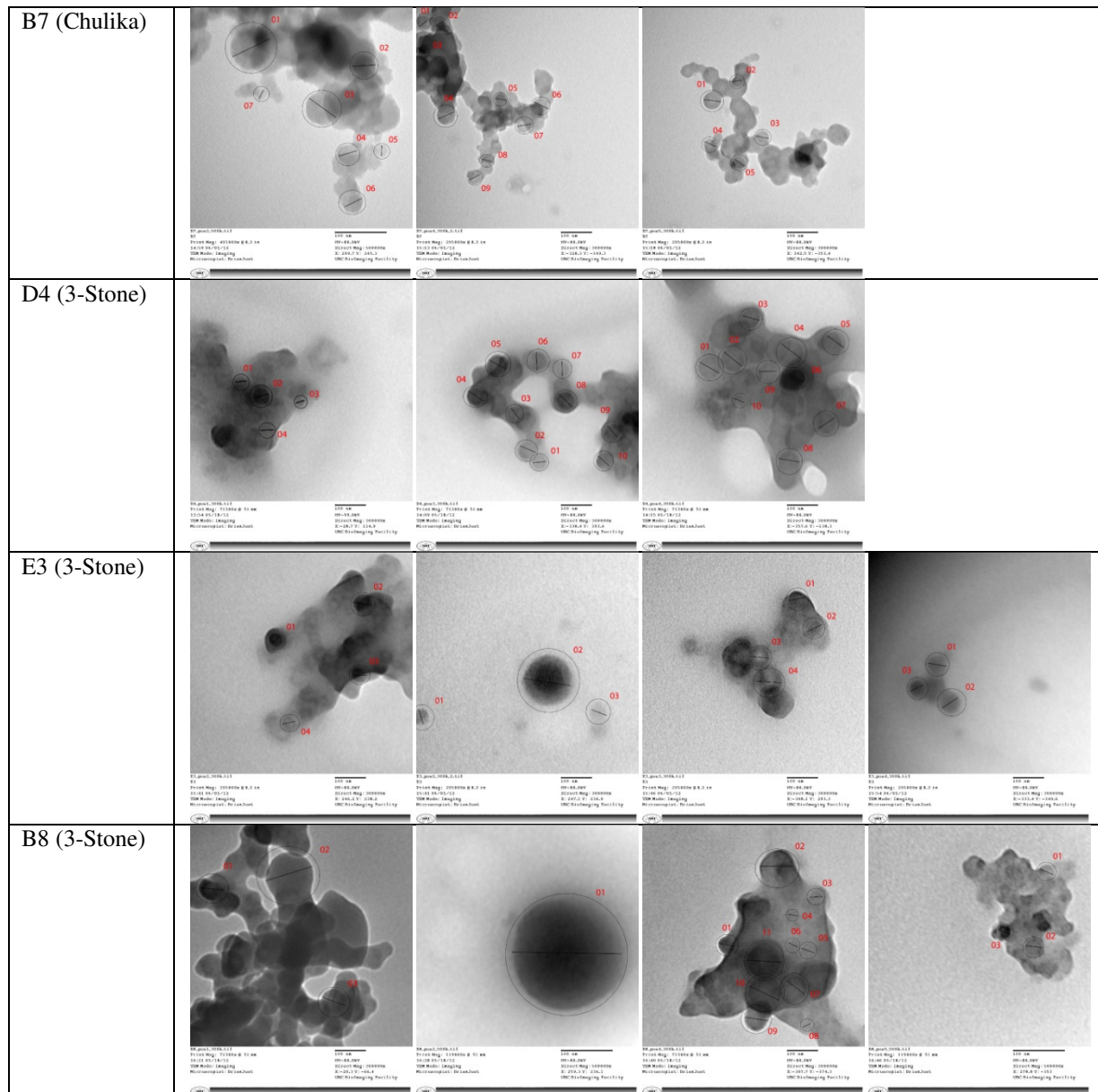
300/500kx mag.	Test 1 (D4)	Test 2 (E3)	Test 4 (B8)
3-Stone point 1	 <p>300kx</p>	 <p>300kx</p>	 <p>300kx</p>
point 2	 <p>300kx</p>	 <p>300kx,a</p>  <p>300kx,b</p>	 <p>300kx,a</p>  <p>500kx,b</p>
point 3	 <p>300kx</p>  <p>500kx</p>	 <p>300kx</p>  <p>500kx</p>	 <p>300kx</p>

<p>point 4</p>	 <p>300kx</p>  <p>500kx</p>	 <p>300kx</p>	 <p>300kx</p>
<p>point 5</p>	 <p>300kx</p>	 <p>300kx</p>	 <p>300kx</p>  <p>500kx</p>

Appendix S: Primary particle sizing

A full catalogue of images used for primary particle sizing is included here. Larger files are available electronically.





Imaging software was used to measure particle sizes. See Figure 46 - Figure 48. Scaled measurements used in the summary in the main body appear in Figure 49.

raw	Oorja								
	D1, pt1 (500)	D1, pt2 (500)	D1, pt4 (300)	B6, pt1 (500)	B6, pt4 (500)	B6, pt5 (300)	B9, pt2 (300)	B9, pt3 (500)	B9, pt5 (300)
1	0.118 a	0.037 s	0.044 s	0.126 a	0.181 a	0.079 a	0.278 s	0.196 s	0.149 s
2	0.127 s	0.046 s	0.025 s	0.141 a	0.14 a	0.104 a	0.131 s	0.511 s	0.149 s
3	0.089 a	0.188 s	0.023 s	0.124 a	0.153 a	0.085 a	0.119 s	0.508 a	0.323 a
4	0.119 a	0.045 s	0.026 s	0.091 a	0.142 a	0.157 a	0.144 s	1.098 a	0.396 a
5	0.143 a	0.042 s	0.024 s	0.164 a	0.134 a	0.101 a	0.111 s	0.327 a	0.175 a
6	0.112 a	0.039 s	0.079 s	0.147 a	0.13 a	0.162 a	0.28 a	0.344 a	0.272 a
7	0.141 a	0.047 s	0.024 s	0.151 a	0.145 a	0.101 a	0.242 a	0.263 a	0.569 a
8	0.118 a	0.041 s	0.036 s	0.153 a	0.158 a	0.097 a	0.249 a	0.301 a	0.458 a
9	0.098 a	0.07 a	0.027 s	0.155 a	0.132 a	0.044 a	0.121 s	0.348 a	0.31 a
10	0.136 a	0.106 a	0.031 s	0.155 a		0.068 a	0.121 a	0.184 a	0.124 s
11	0.101 a	0.073 a	0.025 s	0.154 a		0.056 a	0.41 a	0.738 a	0.125 s
12	0.141 a	0.078 a	0.025 s	0.177 a		0.075 a	0.272 a	0.818 a	0.15 s
13	0.111 a	0.097 a	0.026 s	0.175 a		0.1 a	0.218 a		0.22 s
14	0.121 a	0.079 a	0.023 s	0.168 a		0.15 a	0.201 a		
15		0.043 s	0.028 s			0.066 a	0.201 a		
16		0.039 s	0.026 s			0.129 a	0.134 a		
17		0.055 s	0.059 a			0.082 a	0.306 a		
18		0.088 a	0.067 a			0.069 a	0.126 a		
19			0.024 a				0.34 a		
20			0.072 a				0.55 a		
21			0.074 a				0.21 a		
22			0.03 s				0.165 a		
23			0.029 s				0.432 a		
24			0.044 s				0.2 a		
25			0.026 s				0.296 a		
26			0.026 s						
27			0.025 a						
28			0.034 a						
29			0.036 a						
30			0.023 s						
31			0.036 s						
32			0.028 s						

Figure 46. Raw sizing data, Oorja

raw	Chulika								
	D2, pt3 (300)	D2, pt4 (300)	D2, pt5 (500)	E1, pt1 (300)	E1, pt3 (300)	E1, pt5 (300)	B7, pt2 (500)	B7, pt4 (300)	B7, pt5 (300)
1	0.05 s	0.147 a	0.322 a	0.684 a	0.399 a	0.313 a	1.555 a	0.404 a	0.644 a
2	0.057 s	0.057 s	0.345 a	0.338 a	0.34 a	0.309 a	0.868 a	0.351 a	0.359 a
3	0.06 s	0.061 s	0.412 a	0.244 a	0.453 a	0.393 a	1.278 a	0.354 a	0.458 a
4	0.062 s	0.083 a	0.36 a	0.335 a	0.466 a	0.525 a	0.713 a	0.679 a	0.48 a
5	0.047 s	0.086 a	0.381 a	0.335 a	0.381 a	0.531 a	0.402 a	0.42 a	0.465 a
6	0.065 a	0.065 a	0.374 a	0.369 a	0.432 a	0.885 a	0.771 a	0.602 a	
7	0.063 a	0.079 a	0.347 a	0.453 a	0.381 a	0.722 a	0.384 a	0.558 a	
8	0.126 a	0.083 a	0.373 a	0.442 a	0.36 a	0.985 a		0.417 a	
9	0.093 s		0.366 a	0.375 a	0.391 a	0.839 a		0.473 a	
10			0.4 a		0.429 a	0.894 a			
11					0.426 a	0.58 a			
12					0.44 a				
13					0.402 a				
14					0.32 a				
15					0.415 a				
16					0.519 a				
17					0.438 a				
18					0.56 a				
19					0.407 a				
20					0.72 a				
21					0.874 a				
22					0.831 a				
23					0.547 a				

Figure 47. Raw sizing data, Chulika

raw	Three-stone			a	b	E3, pt3 (300)	E3, pt4 (300)	B8, pt1 (300)	B8, pt2 (500)	B8, pt4 (300)	B8, pt5 (500)
	D4, pt1 (300)	D4, pt3 (300)	D4, pt4 (300)								
1	0.104 a	0.114 a	0.198 a	0.464 a	0.576 s	0.638 a	0.69 a	0.21 a	0.988 s	0.146 a	0.13 a
2	0.142 a	0.163 a	0.206 a	0.695 a	1.783 s	0.618 a	0.702 a	0.43 a		0.294 a	0.152 a
3	0.08 a	0.131 a	0.155 a	0.547 a	0.556 s	0.763 a	0.562 a	0.226 a		0.11 a	0.116 a
4	0.116 a	0.156 a	0.221 a	0.496 a		0.976 a				0.08 a	
5		0.181 a	0.189 a							0.113 a	
6		0.161 a	0.161 a							0.099 a	
7		0.123 a	0.163 a							0.2 a	
8		0.161 a	0.183 a							0.071 a	
9		0.144 a	0.153 a							0.202 a	
10		0.139 a	0.093 a							0.291 a	
11										0.284 a	

Figure 48. Raw sizing data, 3-Stone

	Dorja									Chulika									Three-stone											
	D1,pt1 (500)	D1,pt2 (500)	D1,pt4 (300)	B6,pt1 (500)	B6,pt4 (500)	B6,pt5 (300)	B9,pt2 (300)	B9,pt3 (500)	B9,pt5 (300)	D2,pt3 (300)	D2,pt4 (300)	D2,pt5 (500)	E1,pt1 (300)	E1,pt3 (300)	E1,pt5 (300)	B7,pt2 (500)	B7,pt4 (300)	B7,pt5 (300)	D4,pt1 (300)	D4,pt3 (300)	D4,pt4 (300)	a E3,pt2 (300)	b E3,pt2 (300)	E3,pt3 (300)	E3,pt4 (300)	B8,pt1 (300)	B8,pt2 (500)	B8,pt4 (300)	B8,pt5 (500)	
scale, 100nm=	0.463	0.463	0.279	0.465	0.463	0.278	1.163	1.935	1.159	0.278	0.28	0.463	1.154	1.155	1.155	1.331	1.159	1.154	0.279	0.278	0.278	1.159	1.154	1.159	1.159	0.278	0.463	0.278	0.463	
agglom.	25.5	15.1	21.1	27.1	39.1	28.4	24.1	26.3	27.9	23.4	52.5	63.5	59.3	34.5	27.1	80.5	34.9	55.8	37.3	41.0	71.2	40.0			55.0	59.5	75.5		52.5	28.1
	19.2	22.9	24.0	30.3	30.2	37.4	20.8	56.7	34.2	22.7	29.6	74.5	29.3	23.4	26.8	45.0	30.3	31.1	50.9	58.6	74.1	60.0			53.3	60.6	154.7		105.8	32.8
	25.7	15.8	8.6	26.7	33.0	30.6	21.4	16.9	15.1	45.3	30.7	89.0	21.1	39.2	34.0	66.2	30.5	39.7	28.7	47.1	55.8	47.2			65.8	48.5	81.3		39.6	25.1
	30.9	16.8	25.8	19.6	30.7	56.5	10.4	17.8	23.5		23.2	77.8	29.0	40.3	45.5	36.9	58.6	41.6	41.6	56.1	79.5	42.8			84.2				28.8	
	24.2	21.0	26.5	35.3	28.9	36.3	35.3	13.6	49.1		28.2	82.3	29.0	33.0	46.0	20.8	36.2	40.3		65.1	68.0								40.6	
	30.5	17.1	9.0	31.6	28.1	58.3	23.4	15.6	39.5		29.6	80.8	32.0	37.4	76.6	39.9	51.9		57.9	57.9								35.6		
	25.5	19.0	12.2	32.5	31.3	36.3	18.7	18.0	26.7			74.9	39.3	33.0	62.5	19.9	48.1		44.2	58.6								71.9		
	21.2		12.9	32.9	34.1	34.9	17.3	9.5				80.6	38.3	31.2	85.3		36.0		57.9	65.8								25.5		
	29.4			33.3	28.5	15.8	17.3	38.1				79.0	32.5	33.9	72.6		40.8		51.8	55.0								72.7		
	21.8			33.3		24.5	11.5	42.3				86.4		37.1	77.4				50.0	33.5								104.7		
	30.5			33.1		20.1	26.3							36.9	50.2													102.2		
	24.0			38.1		27.0	10.8							38.1																
	26.1			37.6		36.0	29.2							34.8																
				36.1		54.0	47.3							27.7																
						23.7	18.1							35.9																
						46.4	14.2							44.9																
						29.5	37.1							37.9																
						24.8	17.2							48.5																
							25.5							35.2																
														62.3																
														75.7																
														71.9																
														47.4																
singles	27.4	8.0	15.8				23.9	10.1	12.9	18.0	20.4													49.9			213.4			
		9.9	9.0				11.3	26.4	12.9		20.5	21.8												154.5						
		40.6	8.2				10.2		10.7															48.2						
		9.7	9.3				12.4		10.8																					
		9.1	8.6				9.5		12.9																					
		8.4	28.3				10.4		19.0																					
		10.2	8.6																											
		8.9	12.9																											
		9.3	9.7																											
		8.4	11.1																											
		11.9	9.0																											
			9.0																											
			9.3																											
			8.2																											
			10.0																											
			9.3																											
			10.8																											
			10.4																											
			15.8																											
			9.3																											
			9.3																											
			8.2																											
			12.9																											
			10.0																											

Figure 49. Scaled sizing data, all stoves